MICROCOPY RESOLUTION TEST CHART

NATIONAL BUREAU OF STANDARDS-1963-A

ARO /8965.2-PH

TR - 85 - 015

②

UV SUSTAINED GLOW DISCHARGE OPENING SWITCH

Final Report

M. vonDadelszen, W. M. Moeny, A. E. Rodriguez, C. M. Young and A. I. Lampson

June 1985

U.S. Army Research Office

DTIC
ELECTE
S AUG 2 6 1985 D
B

TETRA CORPORATION
4905 Hawkins Street NE
Albuquerque, New Mexico 87109

AD-A158 411

DTIC FILE COPY

85   8   23   016

TABLE OF CONTENTS

AD-A158411

REPORT DOCUMENTATION PAGE	READ INSTRUCTIONS BEFORE COMPLETING FORM

1. REPORT NUMBER ARO 18965.2 PH	2. GOVT ACCESSION NO. N/A	3. RECIPIENT'S CATALOG NUMBER N/A

4. TITLE (and Subtitle)	5. TYPE OF REPORT & PERIOD COVERED
UV Sustained Glow Discharge Opening Switch	Final Report July 1, 1982 - December 31, 1984
	6. PERFORMING ORG. REPORT NUMBER TETRA TR-85-015

7. AUTHOR(s)	8. CONTRACT OR GRANT NUMBER(s)
M. vonDadelszen and W. M. Moeny	DAAG29-82-C-0018

9. PERFORMING ORGANIZATION NAME AND ADDRESS	10. PROGRAM ELEMENT, PROJECT, TASK AREA & WORK UNIT NUMBERS
Tetra Corporation 4905 Hawkins Street NE Albuquerque, New Mexico 87109	P-18965-S-P

11. CONTROLLING OFFICE NAME AND ADDRESS	12. REPORT DATE
U. S. Army Research Office Post Office Box 12211 Research Triangle Park, NC 27709	13. NUMBER OF PAGES

14. MONITORING AGENCY NAME & ADDRESS(If different from Controlling Office)	15. SECURITY CLASS. (of this report)
	Unclassified
	15a. DECLASSIFICATION/DOWNGRADING SCHEDULE

16. DISTRIBUTION STATEMENT (of this Report)

Approved for public release; distribution unlimited.

17. DISTRIBUTION STATEMENT (of the abstract entered in Block 20, if different from Report)

NA

18. SUPPLEMENTARY NOTES

The view, opinions, and/or findings contained in this report are those of the author(s) and should not be construed as an official Department of the Army position, policy, or decision, unless so designated by other documentation.

19. KEY WORDS (Continue on reverse side if necessary and identify by block number)

UV Sustained Glow Discharges, Externally Sustained Glow Discharges,
Glow Discharge, and
Opening Switches

20. ABSTRACT (Continue on reverse side if necessary and identify by block number)

This was combined theoretical and experimental research program to determine discharge performance characteristics and the influence of various gas mixture additives on discharge performance for UV-sustained glow discharges. This research has a significant technological application in opening switches.

The approach was a coordinated theoretical and experimental research effort to gain understanding of the characteristics and physics of UV-sustained glow

20. ABSTRACT

discharges. A major portion of the research program was an experimental investigation of discharge physics using a single-pulse, UV-sustained 1.5 liter discharge chamber. By measuring discharge characteristics as a function of the electrode separation, pressure, applied voltage, source characteristics, and gas mixture, we determined the relationship between the gas mixture and the discharge kinetics, and between the UV-sustainer characteristics and the glow discharge performance characteristics. The experimental facility included the capability of studying the influence of seedants on discharge performance and measuring glow discharge kinetic rates.

I. INTRODUCTION

This was a combined theoretical and experimental research program to determine discharge performance characteristics and the influence of various gas mixture additives on discharge performance and UV-sustainer physics for UV-sustained glow discharges. This research has a significant technological application in opening switches. The UV-sustained glow discharge opening switch appears to have considerable potential as a reliable, high-current opening switch for pulse power applications. The issues addressed in this research program include:

1. The relationship between UV-sustainer power and glow discharge performance.

2. The relationship between gas mixture and the discharge kinetics.

3. The role of seedants in the UV-sustained glow discharge.

Our approach was a coordinated theoretical and experimental research effort to gain understanding of the characteristics and physics of UV-sustained glow discharges. A major portion of the research program was an experimental investigation of discharge physics using a single-pulse, UV-sustained 1.5 liter discharge chamber. By measuring discharge characteristics as a function of the electrode separation, pressure, applied voltage, source characteristics, and gas mixture, we determined the relationship between the gas mixture and the discharge kinetics, and between the UV-sustainer characteristics and the glow discharge performance characteristics. The experimental facility included the capability of studying the influence of seedants on the discharge performance and measuring glow discharge kinetic rates.

The series R-L storage circuit requires fast opening and closing times with short run (switch conduction) times, whereas the resonant charging-circuit has less critical switching time requirements, but requires long run times. It is concluded from these studies that switch performance is as much a function of the external circuit as it is of the switch characteristics themselves. An optimum system requires a match between the switch characterizations and the external circuit.

Also evaluated are the effects of flashboard offset behind the screen electrode and the electrode separation in determining the optimum photo-ionization seedant density. It is concluded that the smallest flashboard offset to electrode separation ratio gives the best switch performance.

9. ELECTRIC FIELD ANALYSIS

Theoretical studies were undertaken on the field distortion effects of non-uniform photoionization source strength within the discharge. An interesting observation made from these studies was the possibility of field distortion control of glow discharges whereby part of the discharge runs in the externally-sustained mode and part runs in the self-sustained mode. There are many stability issues that must be resolved experimentally, but this may have substantial payoff in improving the switch efficiency.

10. ELECTRO-MAGNETIC NOISE ANALYSIS

Also undertaken was an analysis of the magnitude of Electro-Magnetic Noise (EMN) likely to arise from a glow discharge opening switch. The conclusion is that for glow-discharges, EMN does not pose a significant problem.

11. CONCLUSIONS

The improved understanding of the physics of UV sustained glow discharges obtained on this program indicates that the UV sustained glow discharge opening switch has significant potential. Scaling to opening voltages of about 100 KV and currents of about 100 KA with switch impedances near 0.01 Ω does not appear unreasonable. Until the flashboard UV decay time issue is resolved, opening times appear limited to about 6 μs. It is expected that raised flashboard sparks will enable opening times nearer to 1 μs. Many important physics issues were resolved in this research program, laying the foundation for further research in specific basic issues and for engineering developments of the switch technology. The development of the curvefitting technique for automated data acquisition of recombination, UV source strength, and attachment rates will have significant impact on glow discharge physics studies throughout the scientific community.

9

IV. EXPERIMENTAL FACILITY

This chapter describes the facility and diagnostics. The main issues were the flashboard and flashboard PFN design, EMN suppression, the discharge electrode design and the data reduction.

1. FACILITY DESIGN

Figure 1 shows a schematic diagram of the UV sustained glow discharge opening switch test facility. By definition, there is no spark gap or any other switch in the discharge circuit. The 1Ω series resistor is purely for arc protection. The large value of the discharge capacitor, 14.7 μF, ensures constant voltage throughout the discharge duration,approximately 5-10μs, as long as the discharge impedance is very much greater than the 1Ω series resistor. The rest of the circuit is self evident. The PFN spark gap is triggered manually with our trigger circuit. The set up proved to be very reliable, with negligible jitter between shots. The discharge is 5 cm in radius and the electrode spacing is usually 1 1/2 cm. The flashboard is set 1 1/2 inches behind the screen electrode.

a. **Flashboard Design** --The goals in designing the flashboard were to achieve high spark density, for uniform ionization, with high spark power dissipation for strong photo-ionization source strength, and with an impedance which could be matched easily with a PFN. The flashboard first built by Tetra for this purpose had 11 parallel lines of 12 sparks each. While this flashboard achieved nearly uniform ionization intensity, it had an operating impedance of only about 0.2 Ω. This low impedance made it effectively impossible to match and control with a conventional PFN. Subsequent to this initial flashboard design, Tetra undertook a study of flashboard scaling rules under another contract (See Appendix B). Rather than try to design a sophisticated PFN to match the low impedance flashboard, it was decided to use the scaling rules to design a higher impedance flashboard which could be more readily matched by a conventional PFN.

Figure 2 shows the flashboard which resulted from these considerations. There are 89 sparks in series in an area of 78.5 cm^2. This corresponds to a density of 1.13 sparks /cm^2. With the flashboard offset 1 1/2 in. behind the screen electrode, this spark density gave a uniform UV flux into the discharge. When the flashboard was first tested it had an operating impedance of about

breakdown voltages, indicating that these discharges were energy loading limited, rather than E/N limited.

Discharge efficiencies better than 30% were observed, where the discharge efficiency is defined as the ratio between the energy loaded into the discharge and the sum of the discharge and flashboard energies, with no load in series with the switch. When a load is placed in series with the switch, then the efficiency with which energy is stored, or dissipated, in the load in the switch efficiency is dependent upon the relative impedances, as discussed in Section 2.6.

Two further interesting phenomena were observed. The first was the lack of a cathode fall voltage drop with any N_2 based mix, irrespective of discharge polarity, and the second was the existence of negative differential conductivity oscillations for several gas mixes.

5. SWITCHING TIMES

The switch closing times were typically about 4 μs and were closely controlled by the flashboard current rise times. The opening times, however, were significantly greater than the flashboard current decay times. The fastest opening times, about 10 μs, corresponded with the photo-detector decay times, further suggesting the existence of flashboard substrate surface radiation. For even relatively small attacher seedant densities, it was difficult to resolve the difference between the photo-detector decay and switch opening times. By using raised sparks it is expected that closing and opening times nearer to 1 μs will be achievable.

6. ATTACHMENT, RECOMBINATION, AND SOURCE STRENGTH MEASUREMENTS

There are two points to be made as background to this section. The first is that in every discharge of interest to this program the voltage is less than the self-sustained glow voltage and Townsend ionization is negligible. The second point is that in all the gas mixes the spark spectrum is such that there is negligible photo-ionization of either the nitrogen or the helium. The only source of ionization, therefore, is photo-ionization of seedants within the discharge. The seedants may be contaminants or added gases such as TMA. If the external source were an e-beam or x-rays then this argument would not hold and there would be a significant number of ions of Nitrogen or Helium present.

The curvefitting routine was used to determine the effective attachment and recombination rates as well as the source strengths for N_2 mixes with different concentrations of TMA. These were the only mixes with sufficiently long opening times to allow the accurate use of the curvefitting routine. The calculated source strengths agree well with published values (Ref. 3). As expected, the calculated attachment and recombination rates are significantly different from the known values in pure N_2. This is expected because in these mixes, as just stated, the majority of the ions are those of TMA and its fragments, with negligible ionization of the nitrogen. The discharge physics is, therefore, dominated by the TMA and the nitrogen acts as a buffer gas, fixing the electron velocity distribution. Furthermore, the relative composition of the TMA and its fragments is a function of both the TMA density and the source strength (which is partly a function of the TMA density), and the attachment and recombination rates are observed to not necessarily be linear functions of the TMA density. When an attacher, such as CF_4 or NO, is added then this effect is masked and the TMA simply determines the photoelectron source strength.

There was no evidence of Penning ionization in any of the discharges. For longer discharge durations, however, Penning ionization may play a significant role. (Penning ionization is a mechanism whereby the energy stored in the Nitrogen vitrational manifold ionizes the TMA.)

7. ELECTRODE PHOTO-ELECTRON EMISSION

A mechanism is proposed to explain better the lack of a cathode fall voltage drop for N_2 based mixes and the discharge polarity dependance at the conductivity at low values of E/N. It is suggested that the UV photoelectron secondary emission from the electrode surfaces is stronger than the volumetric photo-ionization in the discharge. This means that no cathode sheath region is necessary to maintain current continuity at the cathode surface for either discharge polarity. This effect leads to a partial e-beam effect in the discharge yielding enhanced conductivities and improved flashboard efficiencies since the UV not absorbed by the gas is available for secondary electron emission from the solid electrode and the UV blocked by the screen electrode also produces secondary electrons. The polarity dependance of the conductivity is due to the different electrode materials.

8. SCALING RULES
Scaling rules have been developed for two types of external circuits. The first circuit type consists of a series R-L inductive storage circuit, with a constant voltage supply. The second type is a resonant charging R-L-C circuit.

photo-ionization source strength, with sufficiently high impedance to enable good impedance matching and control with a Pulse Forming Network (PFN). A series spiral flashboard was designed, using the flashboard scaling laws developed by Tetra (See Appendix B), achieving high spark area density and a 1-3 Ω impedance, depending upon the gas mix and flashboard current. This is the first time, to our knowledge, that flashboards have been matched to a PFN for controlled UV emission.

A 9 stage 2 Ω PFN with a pulse duration of 5.5 μs was built, giving good impedance matching with the flashboard. During the preliminary data acquisition phase the Electro-Magnetic Noise (EMN) from the flashboard PFN presented a problem. This was corrected by a careful shielding of the PFN and isolation of the diagnostics and data acquisition equipment.

The screen (UV transmission) electrode was a copper sheet with a screen etched into it. The solid electrode design was more involved. It was necessary to design a 7.5 cm radius electrode with only a 2.5 cm roll off, yet with a well behaved electric field distribution for variable electrode spacings. Tetra's Electric Field (ELF) Codes (Ref. 2) were used to do this, and the resulting electrode profiles were machined on a Numerically Controlled (NC) lathe. The electrode design is described in Appendix C.

The gas mixing and vacuum systems were standard and are described in Section V along with a complete facility description.

2. DATA ACQUISITION AND REDUCTION

The facility diagnostics consisted of standard high voltage probes and current monitors and a fast photo-detector. All the traces were displayed on a digital storage oscilloscope and transferred, as desired, to a micro-computer to be stored on floppy disks for future reduction and analysis.

Several data reduction programs were developed for the computer. The simplest programs enabled the computation and graphic display and printout of voltage, current, impedance, conductivity, power and energy traces as functions of time. The most sophisticated program was a curvefitting routine enabling the determination of the effective attachment rate, the recombination rate to drift velocity ratio and the photo-ionization source strength-electron drift velocity product. This routine uses the current decay curve, after the source has turned off, and the maximum current density to evaluate the parameters. With the surface spark flashboard the light output is observed by the photodetector to have a decay time significantly longer than the flashboard current decay time. The discharge current is usually small before the source is

5

completely turned off, and hence the curvefitting routine is limited to cases where the recombination and/or attachment rates are relatively small.

A new curvefitting routine has been identified, which uses both the current and photodetector traces. This will enable fitting to the entire current trace, not just the decay curve, and will give good results for any discharge, regardless of the magnitude of the attachment and recombination rates or the rate of decay of the external source. Our existing computer was inadequate to execute this routine, however, and it was not used on this research effort. The routine is outlined in Appendix A.

It is noted that both these curvefitting routines use a parametric approach which, as far as we are aware, is previously unreported. This technique has resulted in measuring new rates previously unreported and has the potential of providing kinetic use measurements for many gas mixtures. The ease of measurment compensates for the somewhat reduced accuracy of the method compared to more direct measurements.

3. FLASHBOARD PERFORMANCE

The series spiral flashboard performed as designed. Average power densities over the flashboard area were greater than 10^5 W/cm^2. This is not an upper power limit, but for surface sparks, higher average power densities lead to reduced flashboard lifetime. The spiral flashboard lifetime was about 750 shots under the normal operating conditions.

As previously stated, the photocell data showed that the light from the flashboard had decay times significantly greater than the flashboard current decay times. This decay time was effectively independent of the gas mix, and it was concluded that the most likely mechanism was light emission from the flashboard substrate surface.

Because of the lifetime and decay time observations, it is concluded that future flashboard development should be directed toward elevated sparks.

4. DISCHARGE MEASUREMENTS

Conductivity measurements were taken for several gas mixes as functions of E/N and photo-ionization source strength. Conductivities better than 3 x $10^{-3}\Omega^{-1}$cm^{-1} were observed with typical flashboard power densities of 1.5-2 x 10^5 W/cm^2. This lead to current densities in the range of 5-10 A/cm^2 near the opening voltage limit for most of the mixes studied. The opening voltage limits were much lower, for the 5.5 μs discharge times, than the corresponding

$$\frac{dn_e}{dt} = S - An_e - Rn_e^2 \qquad\qquad 4.2.1$$

$$J_{max} = e\, n_{e\ max}\, v_e \qquad\qquad 4.2.2$$

and
$$n_{e\ max} = \left[\left(\frac{A}{2R}\right)^2 + \frac{S_{max}}{R}\right]^{\frac{1}{2}} - \frac{A}{2R} \qquad\qquad 4.2.3$$

since when $n_e = n_{emax}$, $dn_e/dt = 0$. For $t > t_0$, $S = 0$ and thus;

$$J(t) = e\, n_e(t)\, v_e \qquad\qquad 4.2.4$$

$$n_e(t) = \frac{A}{\left(\frac{A}{n_{eo}R} + R\right) e^{A(t-t_0)} - R} \qquad\qquad 4.2.5$$

and
$$n_{eo} = \frac{J_0}{ev_e} \qquad\qquad 4.2.6$$

The parameters in equations 4.2.1 – 4.2.6. are defined as follows:

S = photoelectron source strength
A = attachment rate coefficient [$f(E/N)$]
R = recombination rate coefficient [$f(E/N)$]
n_e = electron number density [$f(A,p,S)$]
v_e = electron drift velocity [$f(E/N)$]
P = photoionization seedant density

The subscript, max, refers to the values when $J = J_{max}$, and the subscript, 0, refers to the values when $J = J_0$.

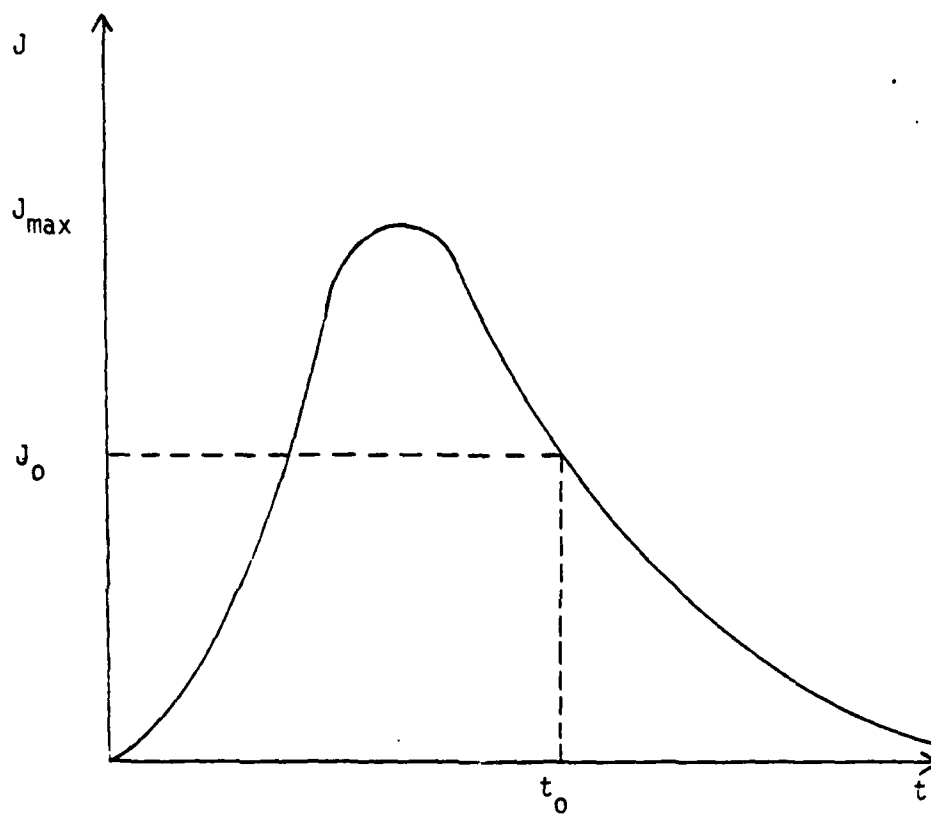It is noted that, theoretically, the information to solve equations 4.2.4 –

Figure 10   An Illustrative Current vs. Time Trace

21

power and energy traces as functions of time. They need not be detailed in this report. A curvefitting routine was developed, however, which enabled the computation of the effective attachment rate and the recombination rate to drift velocity ratio as well as the photo-ionization source strength to electron drift velocity product from the current traces. This program uses a novel parametric approach and is outlined next.

a. The Curve-Fitting Routine-- In order for the results of this investigation to have general applicability to a wide range of geometries, the raw data must be reduced to a more useful form. The goal is to obtain values for the attachment and recombination rate coefficients and the electron drift velocity as functions of E/N and the photoelectron source strength as a function of flashboard power density, gas mix and geometry. A novel parametric approach is outlined in this section which uses the discharge current decay curve to evaluate these parameters. It is shown that it is not possible to obtain absolute values for all of the parameters, but that relative magnitudes between the parameters can be obtained with this approach, yielding significant insight into the discharge physics. We are not aware of any previous work using this approach to obtain these values. The methods enables quick and inexpensive results.

An extension to this method is suggested in Appendix A which will allow fitting to the entire current trace, not just the decay curve. Our present data acquisition and reduction system is inadequate to undertake this, but the results to date give us confidence that this new approach will work.

Consider the current density trace shown in Figure 10. J_{max} is the maximum UV sustained current density, J_0 is the current density at some time, t_0, after the UV source is turned off. Because of the low currents and large storage capacitance used in the experiments, it is assumed that the discharge voltage remains constant throughout the discharge duration. The longest discharges are of the order of 10 μs, whereas it is easy to show that the pressure will take more than 100 μs to equilibrate. It is assumed, therefore, that the gas neutral particle number density, N, will also remain constant. With these two assumptions, the value of E/N and thus the electron drift velocity will remain constant during the discharge. The final assumptions made are that all the current is carried by the electrons and that, for each gas mix at each value of E/N, there is one effective attachment and one effective recombination rate coefficient. With these assumptions the following relationships hold;

20

Photodetector
(2 V/div)

Current
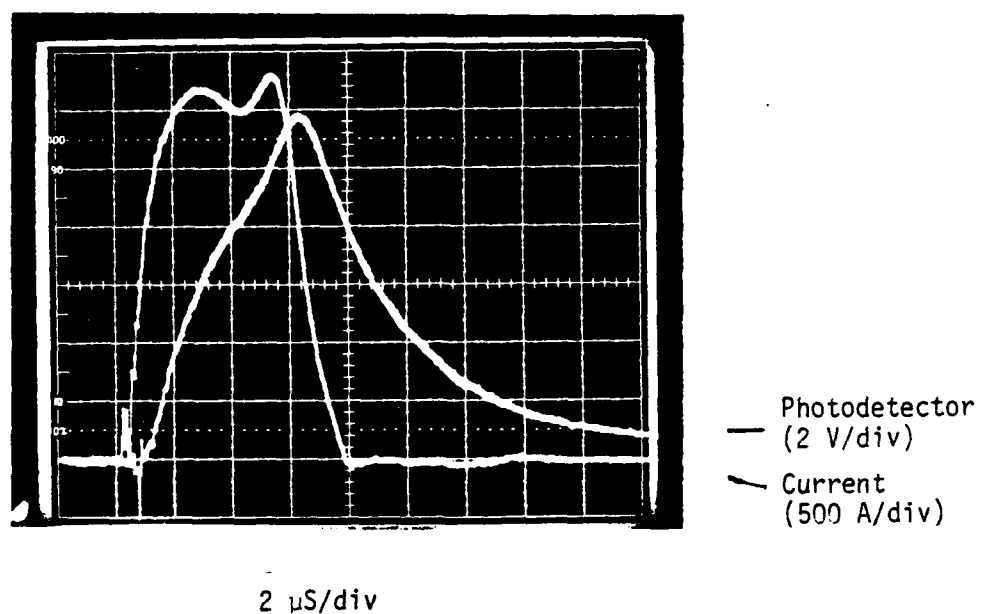(500 A/div)

2 µS/div

Figure 8 The Flashboard Current Trace and Corresponding
Photodetector Trace.
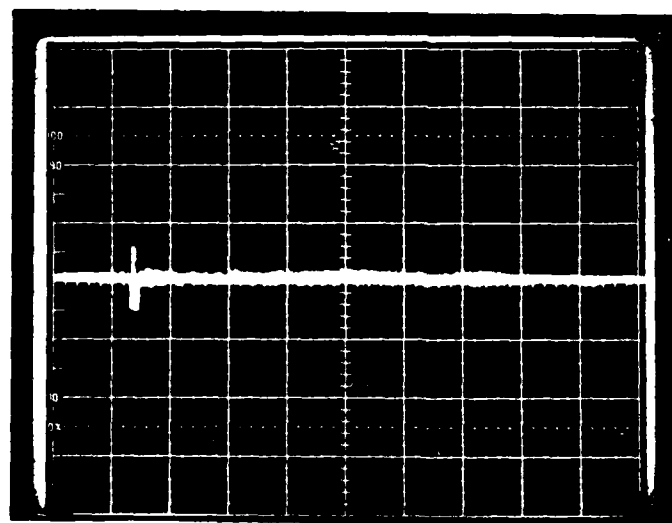

Figure 9 The Photodetector Trace for the Same Flashboard
Conditions as in Fig. 8, but with the Photocell
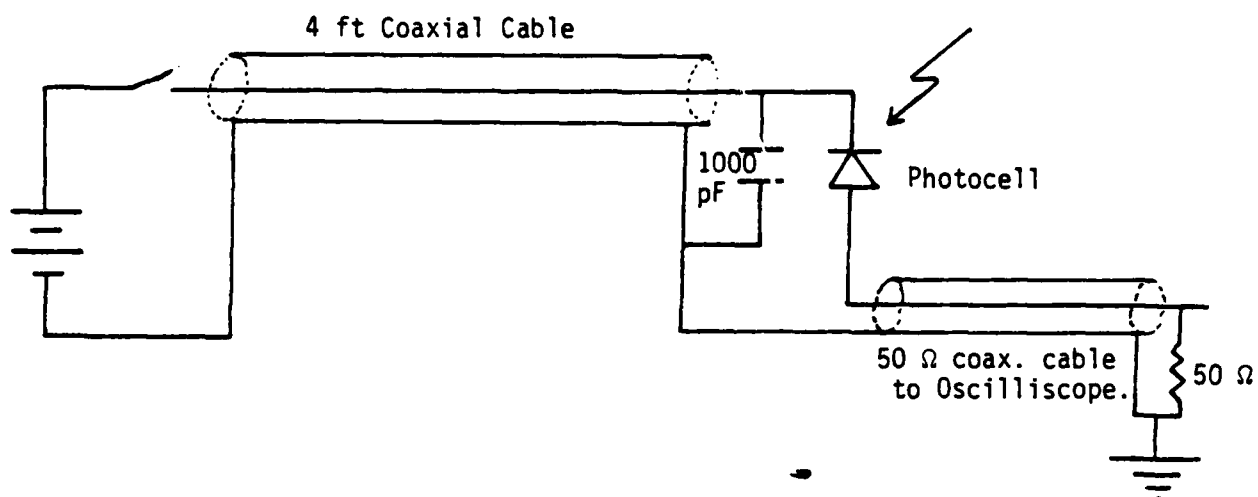Masked Off.

19

4 ft Coaxial Cable

1000 pF

Photocell

50 Ω coax. cable
to Oscilliscope.

50 Ω

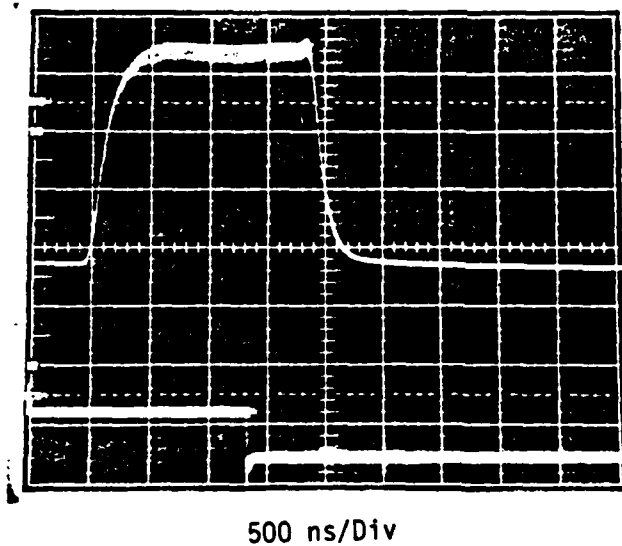Figure 6   The Photodectector Circuit.

500 ns/Div

Figure 7   The Photodetector Responce Time.

2. DATA ACQUISITION AND REDUCTION

The current and voltage diagnostics were standard low noise inductive current monitors and resistive voltage dividers. Also used was a fast photodetector. The optical element was a PIN silicon photocell. Figure 6 shows the electrical circuit used for the photodetector. The photocell has a spectral response from 200-1150 nm. The UV wavelengths of interest are typically less than 150 nm, so the photodetector does not measure the flashboard performance directly. The results of the next two subsections indicate, however, that the photoelectron source strength follows the photocell trace very closely. The photodetector response time was measured at the Air Force Weapons Laboratory using a Bragg cell switched helium-neon laser. Figure 7 shows the trace which was obtained. The Bragg cell had a switching time of at least 250 ns. The $1/e^2$ on and off times for the trace are 400 ns. It is concluded, therefore, that the photodetector response time is better than 150 ns, which is adequate for this investigation.

The circuit was designed for fast response and low EMN sensitivity. Figures 8 and 9 show photodetector traces for identical flashboard shots. In Figure 9 the photodetector has been masked off with black electrical tape, and, apart from some spark gap noise, the trace is almost perfectly flat. It is concluded, therefore, that the photodetector traces show the correct relative flashboard intensities with good time response. It is also noted that for the voltages observed in the traces the photocell is calibrated as having a linear response with light intensity. With the above considerations in mind, it is interesting to look again at Figure 8. The flashboard light has a significant intensity for more than 10 μs after the flashboard current has been completely turned off. This issue will be addressed in the next two subsections.The data was normally acquired and displayed on a Tektronix 468 digital storage oscilloscope. The oscilloscope stores 512 data points per trace and has 8 bit accuracy. The output from the oscilloscope is on a GPIB buss and a program was written to enable interaction with an Apple IIe microcomputer. The traces were stored on floppy disks by the computer to enable further analysis and reduction at a later time. This set up proved to be very convenient and reliable, even though the microcomputer tended to be somewhat slow, especially for the data reduction programs.

The majority of the data reduction programs, written for the microcomputer, were relatively simple. They enabled the computation and graphic display and print out of voltage, current, impedance, conductivity,
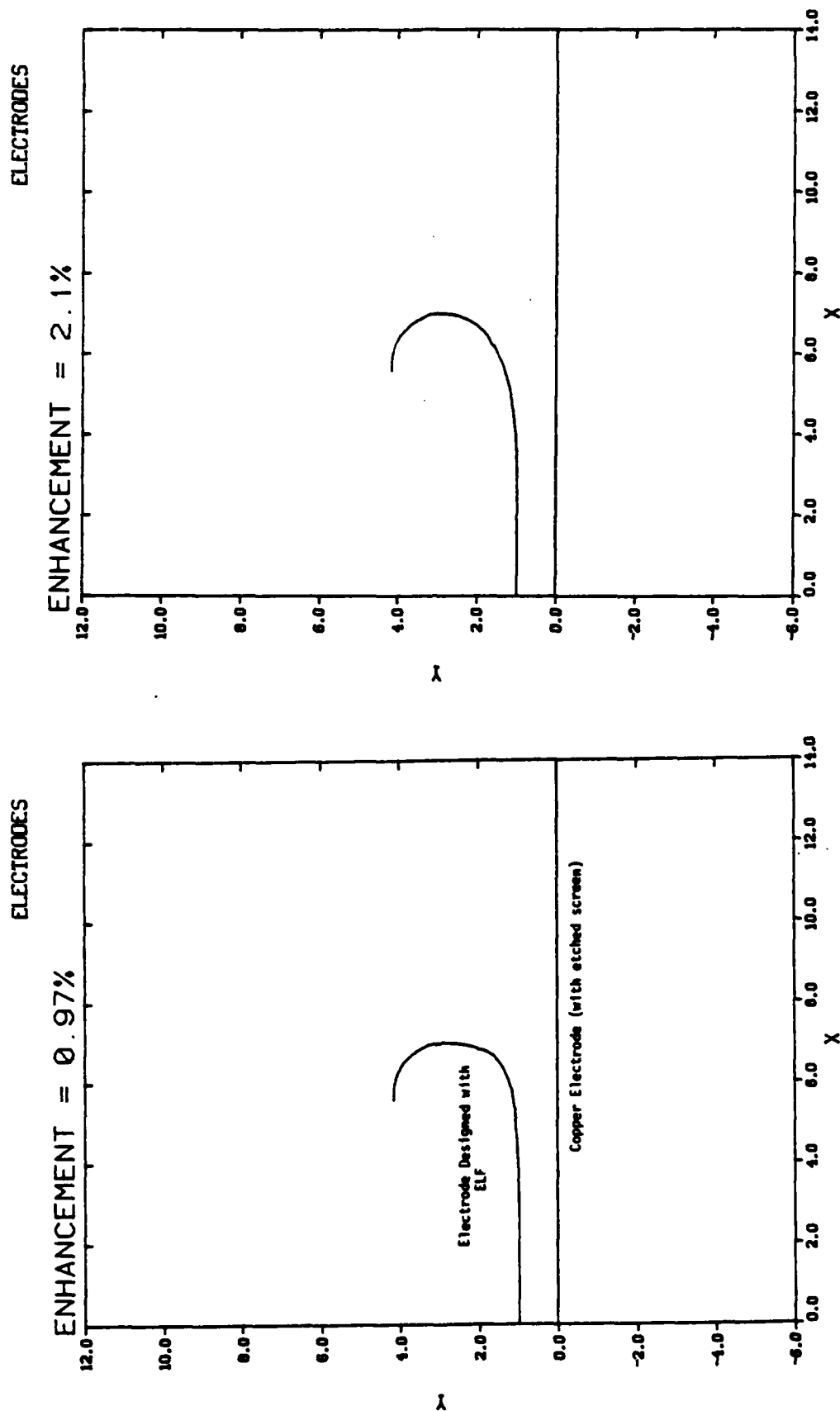
17

ELECTRODES

ENHANCEMENT = 2.1%

Y

X

0.0 2.0 4.0 6.0 8.0 10.0 12.0 14.0

-6.0 -4.0 -2.0 0.0 2.0 4.0 6.0 8.0 10.0 12.0

Figure 5 The Best Electrode Profile for Variable Electrode Spacing.

ELECTRODES

ENHANCEMENT = 0.97%

Electrode Designed with
ELF

Copper Electrodes (with etched screen)

Y

X

0.0 2.0 4.0 6.0 8.0 10.0 12.0 14.0

-6.0 -4.0 -2.0 0.0 2.0 4.0 6.0 8.0 10.0 12.0

Figure 4 The Best Electrode Profile for Uniform Electric Field Distribution with a 1 cm Electrode Spacing. Symmetric about x = 0.

16

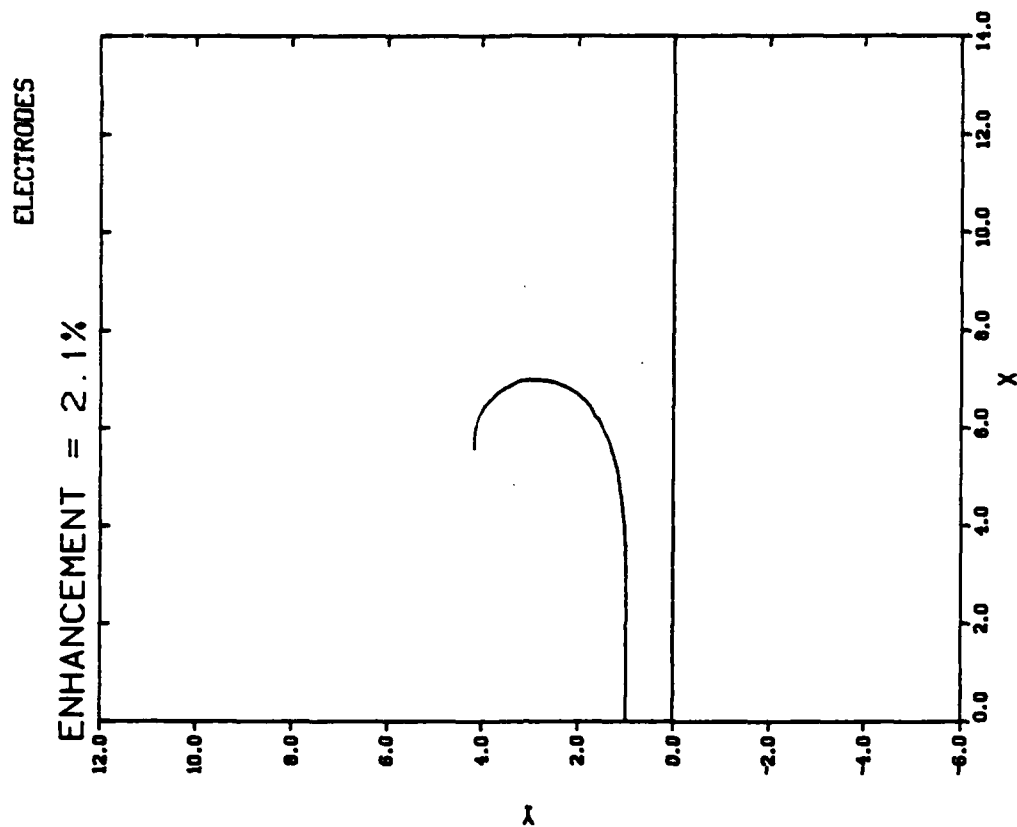d. **The Discharge Electrodes--** The design of the discharge solid electrode required use of the ELF codes. It was necessary to design an axisymetric electrode for a 5 cm radius discharge with a 2 1/2 cm roll off, due to the discharge chamber dimensions. The goal was to design the electrode with uniform electric field over the surface in the discharge region, with no electric field curvature enhancement in the roll off region, and to be used for variable electrode spacings. It was not possible to fulfill these goals with one electrode within the geometry contraints. Consequently two electrodes were designed. One was for a fixed electrode separation of 1 cm and for a very uniform electric field to be used for breakdown voltage measurements. The other was for variable electrode gaps and was designed to keep the roll off enhancements within reasonable limits. The electrode design is described in Appendix C. Figures 4 and 5 show the resulting profiles for the 1 cm gap electrode and the variable gap electrode respectively.

e. **The Flow System --**The flow system was of a standard design. Total flow rates were 2-4 l/min, and the operating pressure was usually 400 torr. At these flow rates a delay of 1 1/2 minutes between shots was sufficient to obtain highly repeatable data. The system could be pumped down to good vacuum, and leak rates were measured at better than 10^{-3} cc/s.
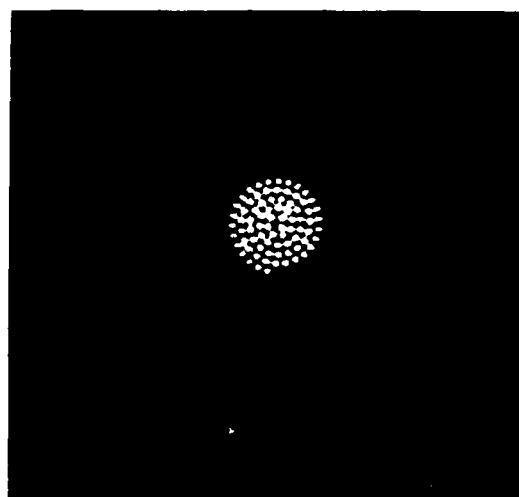
Figure 3   Open shutter photograph of the series
spiral flashboard in operation. Taken
in air.

14 Ω, or about 0.15 Ω per gap. This impedance rapidly changed and after a conditioning period of less than 50 shots settled down to an impedance of about 2Ω, or 0.02 Ω per gap. Figure 3 shows an open shutter photograph of the series spiral flashboard in operation, taken in air. It was necessary to bond a barrier between the spiral lines to avoid flashover between the lines.

b. **The Flashboard PFN**--The flashboard PFN was designed to match a 2 Ω load. There were nine stages with a capacitance of 0.155 µF and a self inductance of 0.54 µH per stage. The mutual inductance between stages was about 0.08 µH. Standard formulae (Ref. 4) were used to design the inductor. This gave a PFN impedance;

$$Z_{pfn} = \sqrt{L_{Total}/C_{Total}} = 2.0 \; \Omega \qquad\qquad 4.1.1$$

and a pulse length;

$$t_{pfn} = 2 \sqrt{L_{Total} C_{Total}} = 5.5 \; \mu s \qquad\qquad 4.1.2$$

c. **EMN Suppression**-- During the preliminary experiments done with the low impedance flashboard it became evident that Electromagnetic Noise (EMN) would present a significant problem in the acquisition of good data unless it were dealt with properly. Because the flashboard itself was fairly well shielded within the discharge chamber, it was assumed that the major sources of EMN were the spark gap and the PFN inductor. By placing the entire PFN and the spark gap circuit inside a Faraday cage, and then grounding the cage to the back end of the pfn, no current flows in the cage itself. It also sees very little ground swing and therefore acts as a very good shield, in spite of the large currents passing in and out of it.

The Faraday cage worked as designed and suppressed the EMN to workable levels. By also shielding the oscilloscope it was possible to virtually eliminate the EMN problem completely. For very low discharge voltages and currents there was still a slight problem in data acquisition, mainly due to ground swing, but it could be handled relatively easily by taking tare measurements with zero discharge voltage and subtracting them from the data.
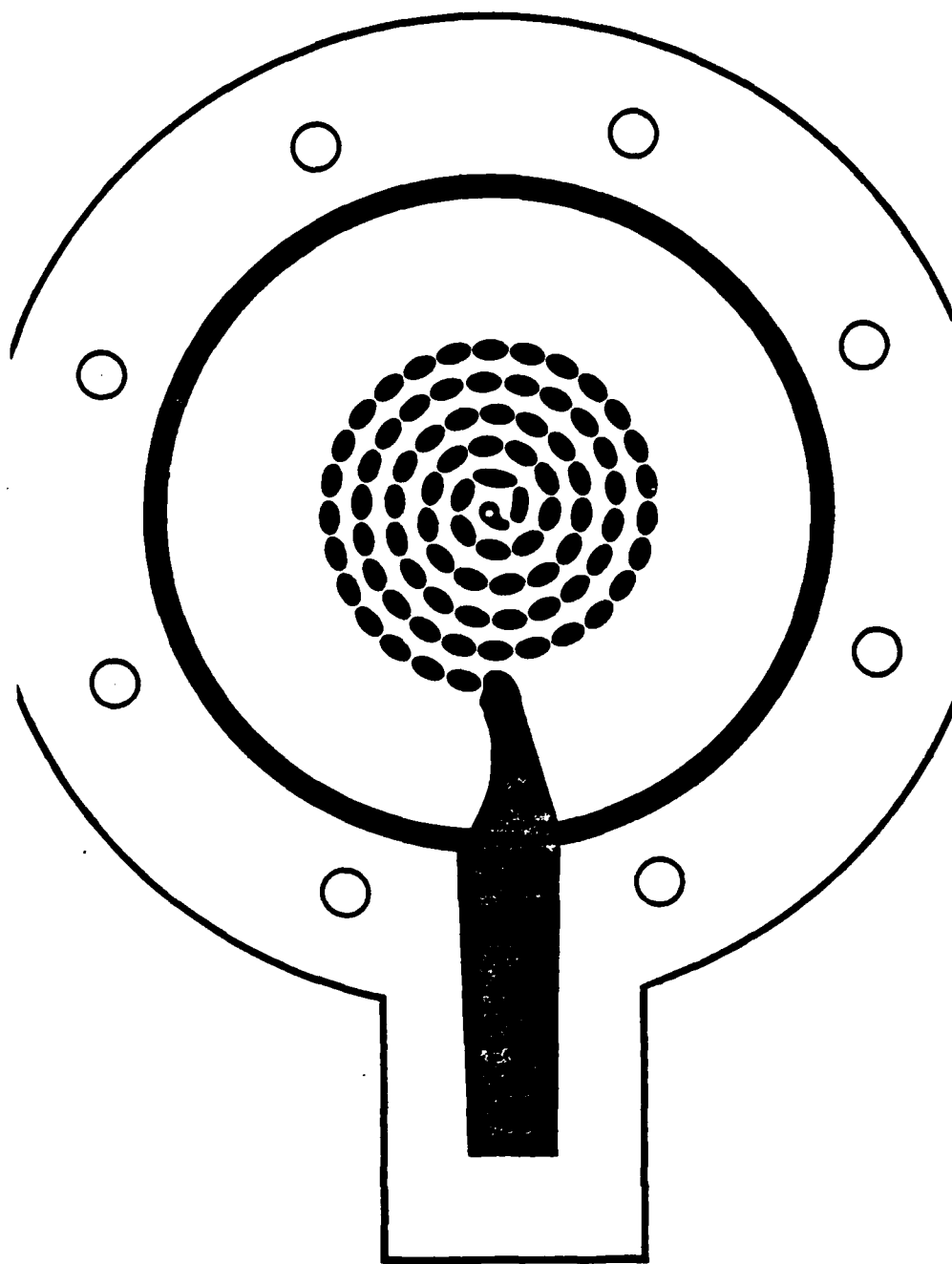
13

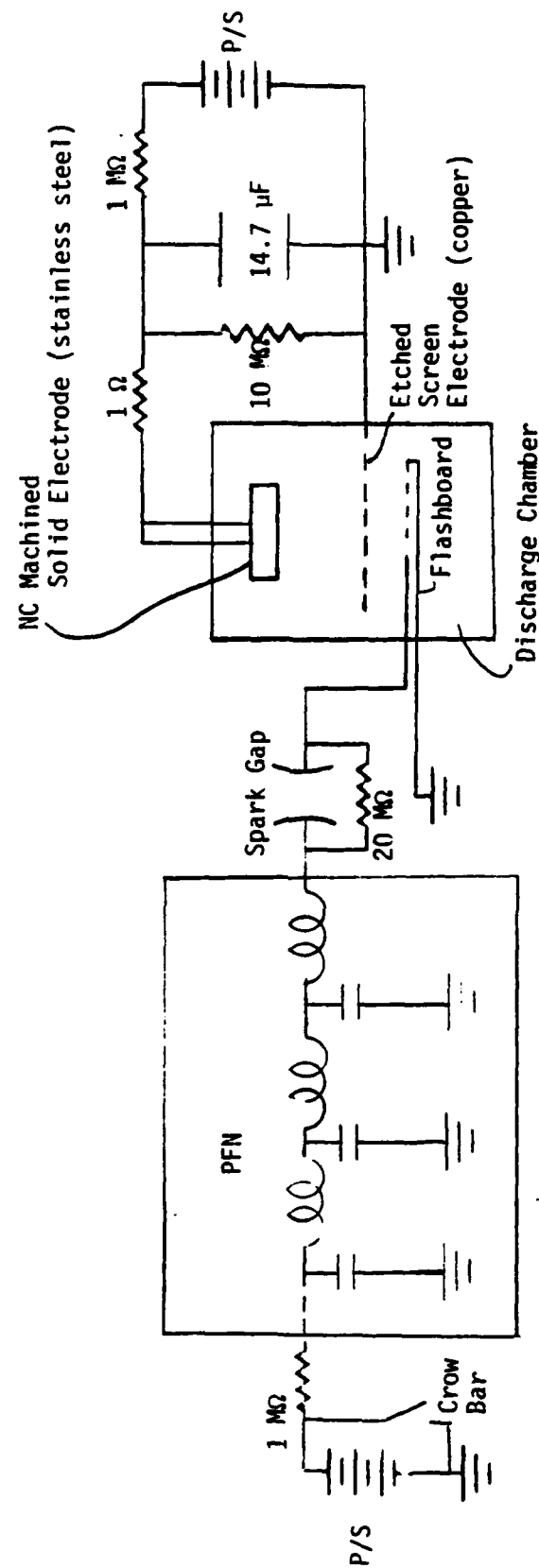Figure 2   The Series Spiral Flashboard

Figure 1   Schematic diagram of the glow discharge opening switch test facility.
Not to scale.

11

III. PROGRAM SUMMARY

The goals of the program were to undertake a theoretical and experimental investigation into the physics of UV sustained glow discharge opening switches with high switch ratio, with high conductivity in the closed mode, with high breakdown electric field, with low photo-ionization power requirements, and with fast switching times.

The majority of gas mixes were N_2 based to take advantage of the 108 nm UV emission. TMA was used as the photo-ionization seedant because of its relatively large photo-ionization cross section at 108 nm (Ref. 1). The attachers used were CF_4 and NO. Helium was used as a buffer gas, frequently as the major constituent. This combination of gases provided wide variations in the discharge physics.

The various issues will be addressed briefly in this summary, and then in greater detail in the following chapters. The results have applications ranging beyond opening switch considerations alone. The issues are largely interrelated, but are arranged in the following order:

1. Facility Design
2. Data Acquisition and Reduction
3. Flashboard Performance
4. Discharge Measurements
5. Switching Times
6. Attachment, Recombination, and Source Strength Measurements
7. Electrode Photo-Electron Emission
8. Scaling Rules
9. Electric Field Analysis
10. Electro-Magnetic Noise Analysis

The following subsections briefly summarize each of these issues and some of the conclusions drawn.

1. FACILITY DESIGN

It was necessary to design a high power flashboard, enabling strong

II. PROGRAM OBJECTIVES

In this section, the goals of the UV-Sustained Radial Glow Discharge Opening Switch Program are summarized.

1. EXPERIMENTAL OBJECTIVES

The experimental objectives can be divided into four basic issues:

a. Develop a photoionizer with high photo-intensity output and with sufficiently high impedance to be controlled by a Pulse Forming Network.

b. Determine the relationship between UV-sustained power and glow discharge performance.

c. Determine the relationship between gas mixture and the discharge kinetics.

d. Determine the role of seedants in the UV-sustainer glow discharge.

2. THEORETICAL OBJECTIVES

The theoretical objectives can similarly be divided into three issues:

a. Use the results of the experimental investigation to develop scaling rules for the UV-sustained glow discharge, particularly for, but not restricted to, opening switch considerations.

b. Understand the effects of non-uniform ionization and conductivity on the discharge physics.

c. Determine the potential problems due to EMN from these discharges.

3

4.2.6 is carried in any part of the current decay curve. If the current density data were sufficiently accurate it would be possible to choose t_0 corresponding to very small values of J_0, and still have all the information necessary to solve the equations. In practice, of course, there is some scatter to the data, and the data have a finite accuracy. Also, in the tail of the decay curve, attachment and/or recombination processes other than the best effective values for the entire current trace may arise. It is best, therefore, to use as much of the decay curve as is possible.

The following approach is used to solve for the values of A, R, and v_e or S. Equations 4.2.4 - 4.2.6 can readily be combined to yield:

$$\frac{J(t)}{J_0} = 1 \bigg/ \left[\left(1 + \frac{RJ_0}{ev_e A} \right) e^{A(t-t_0)} - \frac{RJ_0}{ev_e A} \right]$$

4.2.7

for $t > / t_0$. Define

$$G = \frac{RJ_0}{ev_e A} = \frac{n_{eo} R}{A}$$

4.2.8

Equation 4.2.7 then becomes;

$$\frac{J(t)}{J_0} = \frac{1}{\left[(1+G) e^{A(t-t_0)} - G \right]}$$

4.2.9

The entire current decay curve is written in terms of two parameters, A and G which can easily be solved for by using a curve fitting routine. A two parameter gradient-expansion least squares curve fitting routine, which is described in the next subsection, is used to solve equation 4.2.9 for the best values of the attachment rate coefficient, A, and the parameter G. The remaining parameters can now be solved for as follows. From equation 4.2.8:

$$\frac{R}{v_e} = \frac{eA}{J_0} G = H$$

4.2.10

The values of A, J_0 and B, and Thus H, are all known, Combining equation 4.2.2

23

and 4.2.3 yields:

$$\frac{J_{max}}{e} = v_e \left[\left[\left(\frac{A}{2R}\right)^2 + \frac{S_{max}}{R} \right]^{\frac{1}{2}} - \frac{A}{2R} \right]$$

$$4.2.11$$

But $R = v_e H$, and substituting into equation 4.2.11 and solving for v_e yields:

$$v_e S_{max} = \frac{\left(\frac{J_{max} H}{e} + \frac{A}{2}\right)^2 - \left(\frac{A}{2}\right)^2}{H}$$

$$4.2.12$$

The values that can be derived directly from the current decay curve are the attachment rate coefficient, A, the ratio between the recombination rate coefficient and the drift velocity, R/v_e, and the product of the drift velocity and the maximum source strength, $v_e S_{max}$. If any one of the values of R, V_e or S is known, or can be given a good estimate, then the other two parameters can immediately be derived.

There will be many discharges where either attachment or recombination will be negligible. In either case, to look for a solution for both recombination and attachment rate coefficients may cause numerical overflow or underflow. Consequently these two situations must be dealt with separately. First consider the case where the discharge is attachment dominated, i.e. consider $G \ll 1$. Equation 4.2.1 then becomes;

$$\frac{dn_e}{dt} = S - An_e$$

$$4.2.13$$

which has the solution; for $t > t_0$:

$$n_e(t) = n_{eo} e^{-A(t-t_0)}$$

$$4.2.14$$

thus

$$\frac{J(t)}{J_0} = e^{-A(t-t_0)}$$

$$4.2.15$$

The least squares curve fit for equation 4.2.15 requires no iterations, and is

24

given by;

$$A = Ave \left[\frac{\log\left(\frac{J_0}{J(t)}\right)}{(t-t_0)} \right]$$ 4.2.16

The maximum electron number density is;

$$n_{e\ max} = \frac{S_{max}}{A}$$ 4.2.17

yielding the relationship;

$$v_e\ S_{max} = \frac{J_{max}\ A}{e}$$ 4.2.18

When the discharge is recombination dominated then $G >> 1$. In this case the following expressions are derived;

$$\frac{dn_e}{dt} = S - Rn_e^2 \qquad\qquad 4.2.19$$

$$n_e(t) = \frac{n_{eo}}{[1+n_{eo}R(t-t_o)]} \qquad\qquad 4.2.20$$

$$\frac{J(t)}{J_o} = \frac{1}{[1+n_{eo}R(t-t_o)]} \qquad\qquad 4.2.21$$

$$n_{eo}\,R = \frac{J_o R}{ev_e} = Ave\left[\frac{\left(\frac{J_o}{J(t)}-1\right)}{(t-t_o)}\right] \qquad\qquad 4.2.22$$

$$R/v_e = \frac{e}{J_o}\,Ave\left[\frac{\left(\frac{J_o}{J(t)}-1\right)}{(t-t_o)}\right] = H \qquad\qquad 4.2.23$$

$$n_{e\ max} = \sqrt{\frac{S_{max}}{R}} \qquad\qquad 4.2.24$$

$$v_e S_{max} = \left(\frac{J_{max}}{e}\right)^2 H \qquad\qquad 4.2.25$$

26

b. Further Reduction and Use of the Results-- The results of the curvefitting routine give the parameters A, R/v_e and $v_e S$. If the following functional assumptions are made;

$$A = A \, (E/N)$$

$$R/v_e = R/v_e \, (E/N)$$

and

$$v_e S = v_e S \, (E/N, P_{fb}, \rho, x)$$

where

$$v_e = v_e \, (E/N)$$

and

$$S = S \, (P_{fb}, \rho, x)$$

and where P_{fb} is the flashboard power per unit area, Rho is the photionization seedant density and X is the distance from the flashboard, then with sufficient data a parametric investigation should be sufficient to determine the absolute values of v_e and S. and thus of R. Using the Westinghouse results (Ref. 3) a source term of the form;

$$S = \text{Const} \; P_{fb} \; \rho \; e^{-(\alpha + \beta \rho x)} \qquad\qquad 4.2.26$$

should be fitted to.

Even without this further data reduction, it is noted that equations 4.2.2 and 4.2.3 can be combined to yield;

$$J_{max} = e \left[\left[\left(\frac{A}{2} \frac{v_e}{R} \right)^2 + \frac{v_e}{R} v_e S \right]^{\frac{1}{2}} - \frac{A}{2} \frac{v_e}{R} \right] \qquad 4.2.27$$

27

Thus even by evaluating the three terms A, R/v_e and v_e S significant insight can be gained into predicting discharge performance. Use of the three parameter curvefitting routine identified in Appendix A will enable the acquisition of data over a wide variety of parameters.

c. Gradient-Expansion Least Squares Curve Fitting-- There are several methods of obtaining a least squares curve fit to a set of data. One method is by use of gradient-expansion iterations. This approach has the advantage of converging even for first guesses which are many orders of magnitude off while giving rapid convergence as the final solution is approached. It is well described elsewhere (Ref. 5) and will not be desribed in any detail here. All that will be presented is the particular algorithm for the curvefitting routine. For each data point define:

$$JR^1 = \frac{J^1}{J_0} = \frac{1}{\left[(1+G)e^{A(t^1-t_0)}-G\right]}$$ 4.2.28

then

$$\frac{\partial JR^1}{\partial A} = JA^1 = \frac{-t(1+G)}{\left[(1+G)e^{A(t^1-t_0)}-G\right]^2}$$ 4.2.29

and

$$\frac{\partial JR^1}{\partial G} = JG^1 = \frac{-\left(e^{A(t^1-t_0)}-1\right)}{\left[(1+G)e^{A(t^1-t_0)}-G\right]^2}$$ 4.2.30

let

$$\underline{\underline{\alpha}} = \begin{bmatrix} (1+\lambda) \sum_1 (JA^1)^2 & \sum_1 JA^1 JG^1 \\ \sum_1 JA^1 JG^1 & (1+\lambda) \sum_1 (JG^1)^2 \end{bmatrix}$$ 4.2.31

$$\underline{\beta} = \begin{bmatrix} \sum_1 (JR^1 - JR(t^1))JA^1 \\ \sum_1 (JR^1 - JR(t^1))JG^1 \end{bmatrix}$$ 4.2.32

28

and
$$\underline{\underline{\Sigma}} = \underline{\underline{a}}^{-1}$$
4.2.33

Finally define;

$$\Delta A = \beta_1 c_{11} + \beta_2 c_{12}$$
4.2.34

$$\Delta G = \beta_1 c_{21} + \beta_2 c_{22}$$
4.2.35

$$x^2 = \sum_i \left(JR^i - JR(t_i) \right)^2$$
4.2.36

The scheme goes as follows. Guess values for A and the parameters that make up G. Choose a value for Lambda (normally 10^{-3}).

With the initial guesses for A and G solve for the JR_i. Evaluate the error, X^2, for these values.

Solve for the values of ΔA and ΔG. Solve for the JR_i with $A = A + \Delta A$ and $G = G + \Delta G$. Evaluate X^2 for the new Jr_i.

If X^2 decreases accept ΔA, ΔG. Let Lambda become Lambda /2.

If X^2 increases keep old A, G. Let Lambda become 2 Lambda.

Iterate until $\Delta A/A < 10^{-3}$ and $\Delta G/G < 10^{-3}$.

Or, if # iterations > 5 and $\Delta A/A < 10^{-2}$ and $G < 10^3$, go to routine for $G \gg 1$.

This method allows the largest possible steps in A and G (the smallest possible value of x while ensuring a decreasing error (guaranteering convergence). Initial guesses for A and G more than 5 orders of magnitude in error will converge. A large number of iterations will be required for very bad initial guesses, but convergence is guaranteed.

29

d. Suggested Improvements --It is concluded that for all ranges of relative magnitude between the attachment and recombination rates it is possible to derive the absolute value for the attachment rate coefficient, if significant, the ratio between the recombination coefficient and electron drift velocity, if significant, and the product of the maximum source strength and the electron drift velocity. If the absolute values for any one of the source strength, the drift velocity or the recombination rate coefficient values is known or can be reasonably estimated, then the remaining two values can be derived.

This approach has the advantages that only a two parameter curve fit is required and that the source need not turn off instantly in order to obtain values for the parameters of interest. As long as there is a measurable current after the source has eventually turned off then a reasonable estimate of the various parameters is possible. For strong attachment and/or recombination rates or for long source delay times, however, the two parameter curvefitting routine is not adequate.

The results of the following sections indicate that the source strength follows the photocell trace very closely. Because of the long source decay times observed, and thus the necessity of starting the curvefitting at small current values, a method of fitting to the entire current trace, rather than just the decay curve, is desirable. Appendix A outlines a method of doing this. A similar parametric approach as has just been presented is used, along with the normalized photocell trace. A three parameter least squares curve fit is required and our present microcomputer is inadequate to undertake this. The results from the fitting to the decay curve, however, give us confidence that this new proposed routine would be very robust and give accurate results.

V. EXPERIMENTAL RESULTS

1. FLASHBOARD PERFORMANCE

The series spiral flashboard worked effectively as designed. Figures 11, 12 and 13 show a series of current and voltage traces for a 400 torr mix of N_2 with 100 ppm TMA at different PFN charge voltages. In Figure 13 the current trace is inverted with respect to Figures 11 and 12. Figures 14, 15 and 16 show the corresponding impedance, power and energy traces. It is seen that the impedance is not constant, but is dependent upon the flashboard current. The current, or PFN charge voltage, dependence of the flashboard impedance is expected because the analysis described in Appendix B indicates that the flashboard gaps have similar characteristics to a zener diode in series with a resistor. The PFN matches reasonably well for each of these shots, but the optimum matching is for the 12 KV PFN charge voltage. For the 12 KV and 14 KV charge voltage cases the current on and off times are about 2 μs. The choice of a 2 Ω PFN gives adequate impedance matching over a range of flashboard powers. Note that for the 14 KV case the maximum flashboard power density is 0.28 MW/cm^2. The FWHM current pulse width in the 12 KV and 14 KV cases is 5.5 - 6 μS, as designed.

Gases with higher electrical conductivity could not be matched as well at high power. Figures 17-20 and Figures 21-24 show the results for a 50%/50% N_2 H_e mix and a 10%/90% N_2/H_e mix respectively. The greater the percentage of helium, the lower the PFN charge voltage at which impedance matching can be achieved. Even for the 90% helium mixture, however, reasonable matching occurs with power densities of 0.16 MW/cm^2. Pure helium, however, could not be well matched at any PFN charge voltage for this flashboard.

It is concluded that when designing a PFN-flashboard combination the gas conductivity must be taken into account. When using a wide range of gas mixtures it is advisable to have several PFN's available if good impedance matching is desired.

If seedants such as NO or CF_4 are added to the gas similar phenomena are observed. The lower the gas conductivity, the higher the PFN charge voltage at which impedance matching is achieved.

Another observation of interest, related to the flashboard performance, is the decay time of the flashboard light output. As previously stated, the
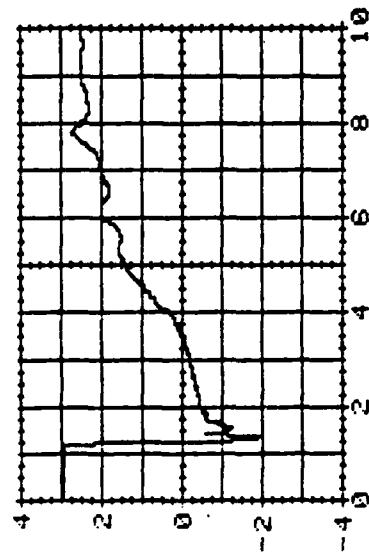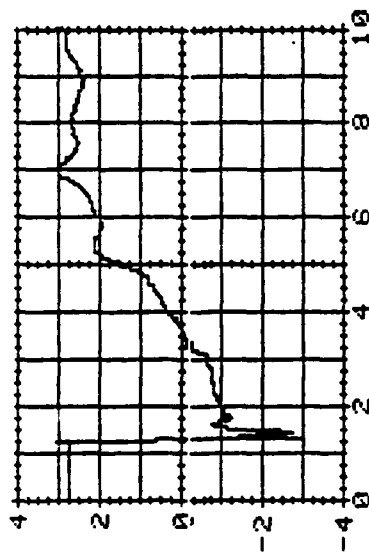
31

TRACE = VOLTS
SCALE = 2000 PER DIVISION
TIME = 2E-06 SEC. PER DIVISION

TRACE = CURRENT (AMPS)
SCALE = 500 PER DIVISION
TIME = 2E-06 SEC. PER DIVISION

Figure 12 As in Figure 11, with a 12 KV PFN Charge.

TRACE = VOLTS
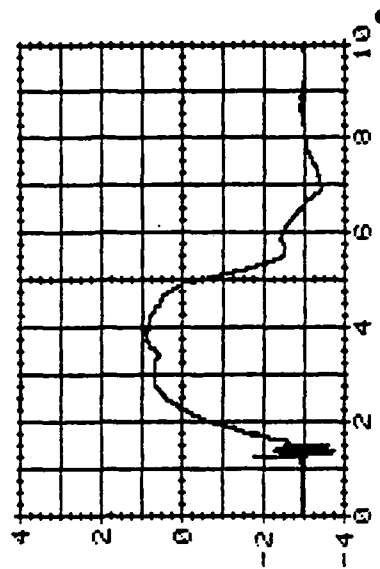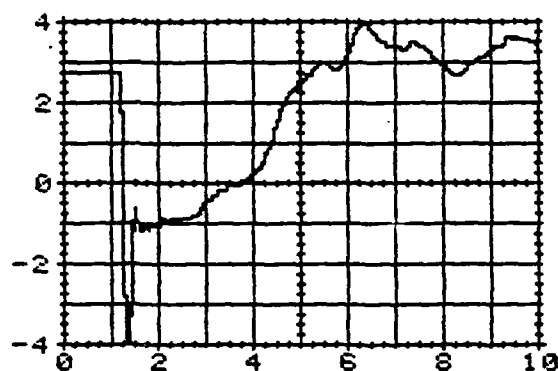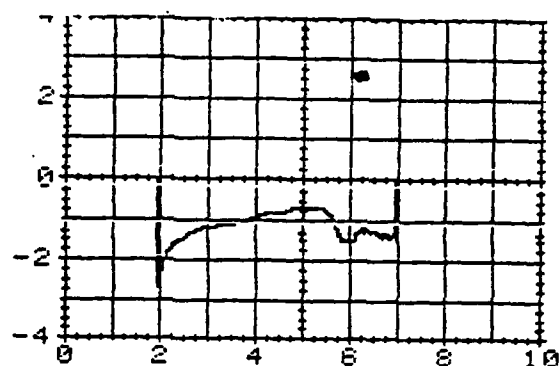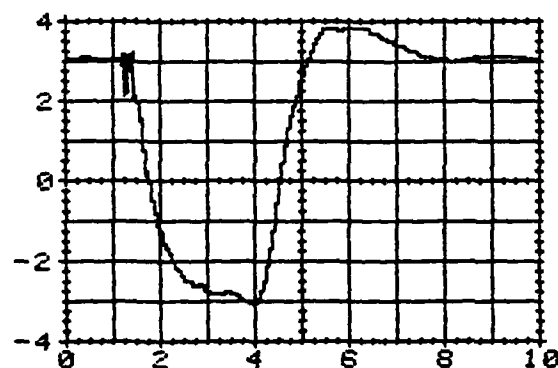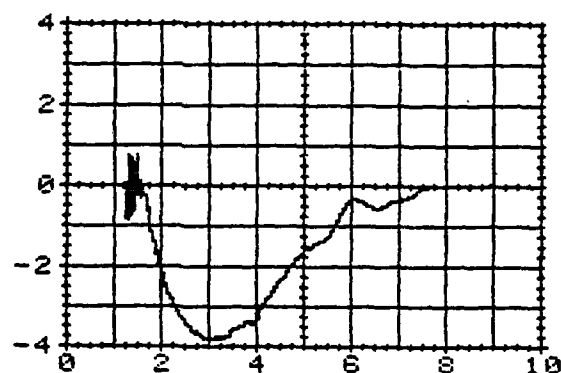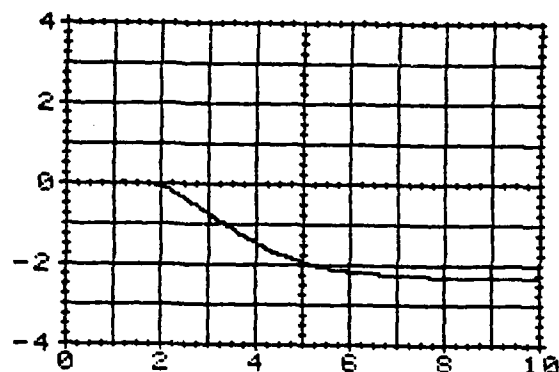SCALE = 2000 PER DIVISION
TIME = 2E-06 SEC. PER DIVISION
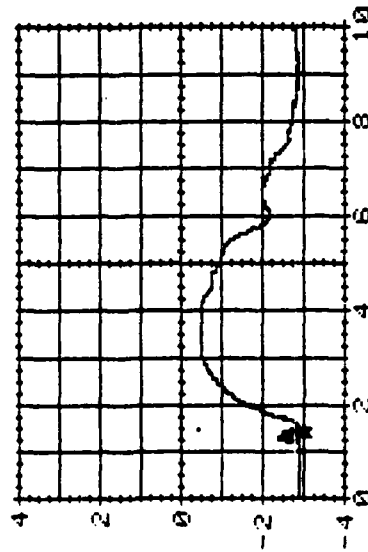
TRACE = CURRENT (AMPS)
SCALE = 500 PER DIVISION
TIME = 2E-06 SEC. PER DIVISION

Figure 11 Flashboard Current and Voltage Traces for a 400 torr Mix of N_2 with 100 ppm TMA and with a 10 KV PFN Charge.

32

TRACE = VOLTS
SCALE = 2000 PER DIVISION
TIME = 2E-06 SEC. PER DIVISION

TRACE = IMPEDENCE (OHMS)
SCALE =5 PER DIVISION
TIME = 2E-06 SEC. PER DIVISION

TRACE = CURRENT (AMPS)
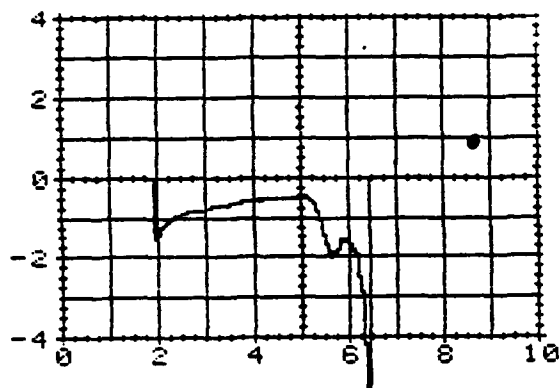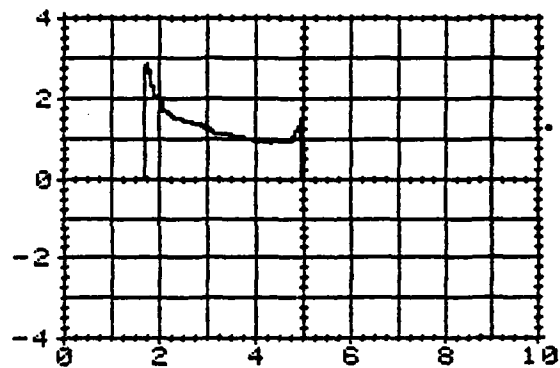SCALE = 500 PER DIVISION
TIME = 2E-06 SEC. PER DIVISION

Figure 13   As in Figure 11, with a 14 KV
            PFN Charge.

TRACE = POWER (WATTS)
SCALE =2000000 PER DIVISION
TIME = 2E-06 SEC. PER DIVISION

TRACE = ENERGY (JOULES)
SCALE =20 PER DIVISION
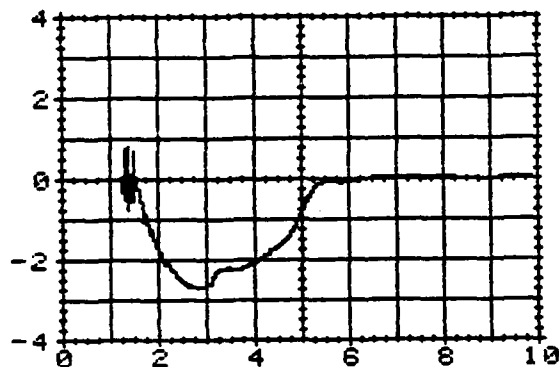TIME = 2E-06 SEC. PER DIVISION

Figure 14   The Flashboard Impedance,
            Power and Energy as Functions of
            Time Corresponding to the Current
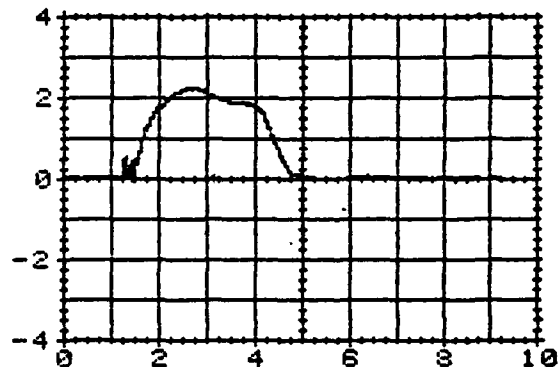   and Voltage Traces in Fig. 11.

33

TRACE = IMPEDENCE (OHMS)
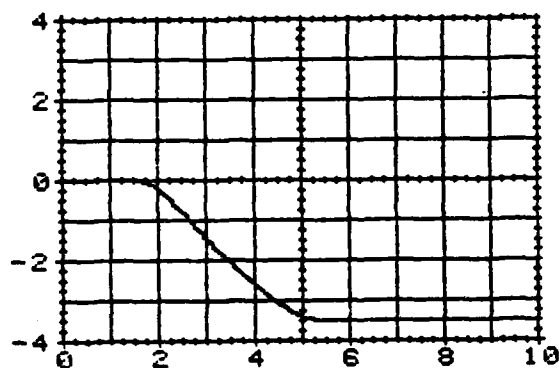SCALE =5 PER DIVISION
TIME = 2E-06 SEC. PER DIVISION

TRACE = IMPEDENCE (OHMS)
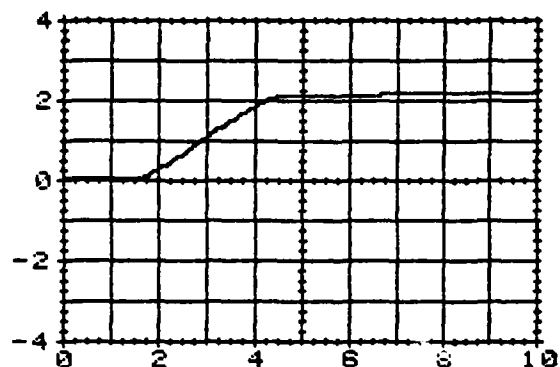SCALE =2 PER DIVISION
TIME = 2E-06 SEC. PER DIVISION

TRACE = POWER (WATTS)
SCALE =5000000 PER DIVISION
TIME = 2E-06 SEC. PER DIVISION

TRACE = POWER (WATTS)
SCALE =10000000 PER DIVISION
TIME = 2E-06 SEC. PER DIVISION

TRACE = ENERGY (JOULES)
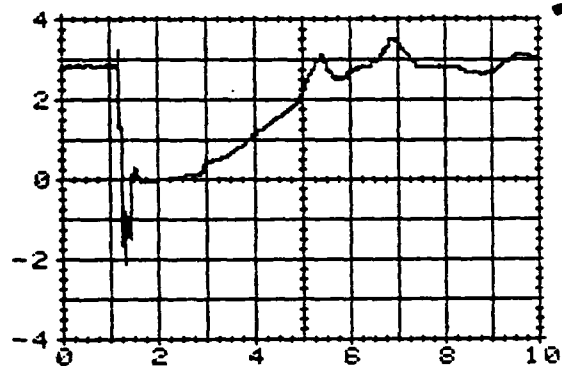SCALE =20 PER DIVISION
TIME = 2E-06 SEC. PER DIVISION

TRACE = ENERGY (JOULES)
SCALE =50 PER DIVISION
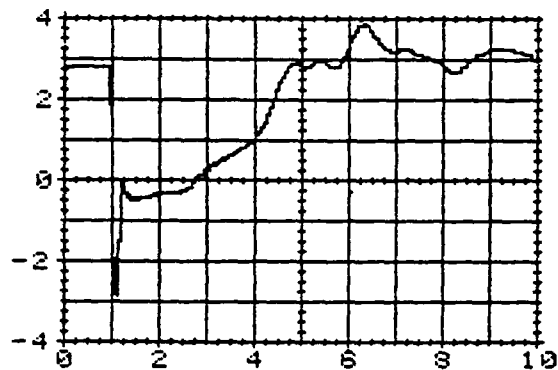TIME = 2E-06 SEC. PER DIVISION

Figure 15 AS in Figure 14, but Corresponding to Figure 12.

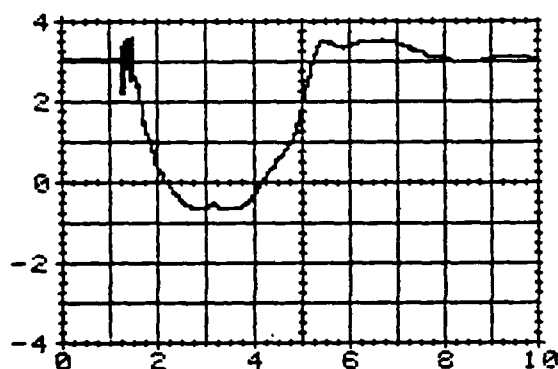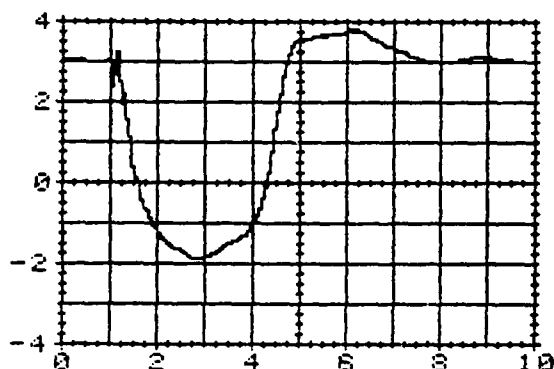Figure 16 As in Figure 14, but Corresponding to Fig. 13.

TRACE = VOLTS
SCALE = 2000 PER DIVISION
TIME = 2E-06 SEC. PER DIVISION

TRACE = VOLTS
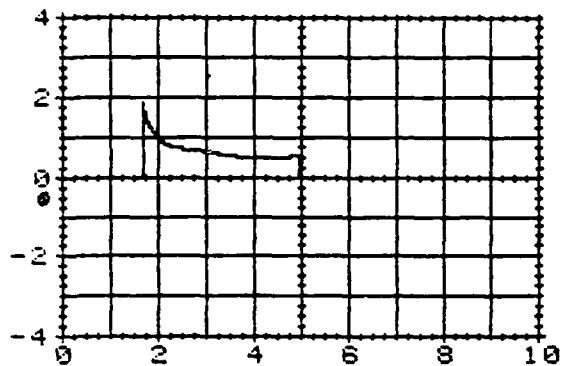SCALE = 2000 PER DIVISION
TIME = 2E-06 SEC. PER DIVISION

TRACE = CURRENT (AMPS)
SCALE = 500 PER DIVISION
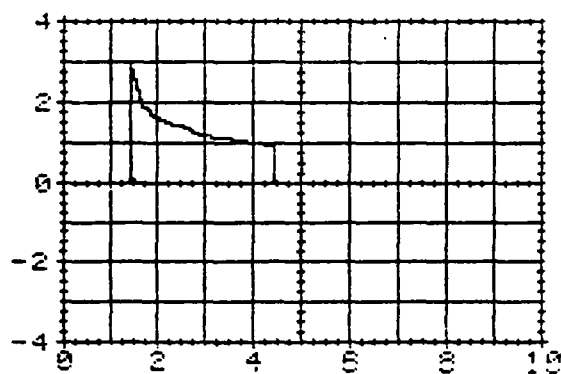TIME = 2E-06 SEC. PER DIVISION

TRACE = CURRENT (AMPS)
SCALE = 500 PER DIVISION
TIME = 2E-06 SEC. PER DIVISION

Figure 17 Flashboard Current and Voltage
Traces for a 400 torr Mix of
50/50 N_2/He with 100 ppm TMA and
with a 10 KV PFN Charge.

Figure 18 As in Figure 17, with
a 12 KV PFN Charge.

35

TRACE = IMPEDENCE (OHMS)
SCALE =5 PER DIVISION
TIME = 2E-06 SEC. PER DIVISION

TRACE = IMPEDENCE (OHMS)
SCALE =2 PER DIVISION
TIME = 2E-06 SEC. PER DIVISION
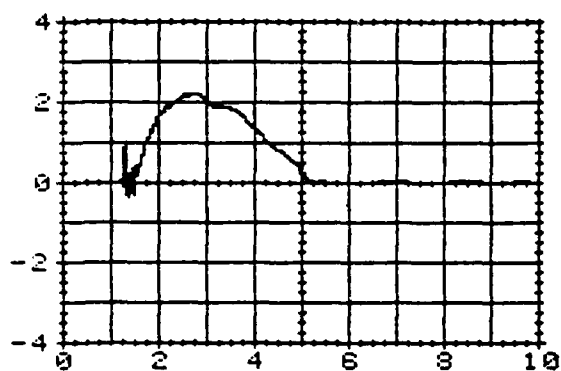
TRACE = POWER (WATTS)
SCALE =5000000 PER DIVISION
TIME = 2E-06 SEC. PER DIVISION
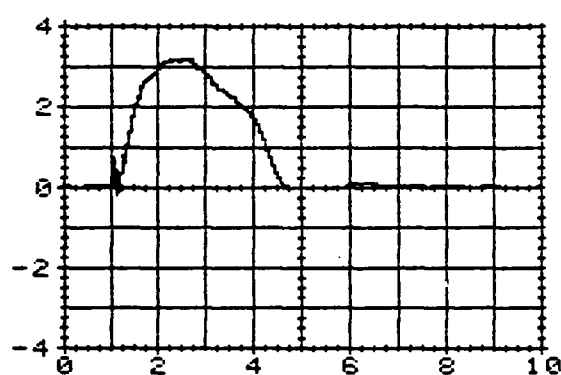
TRACE = POWER (WATTS)
SCALE =5000000 PER DIVISION
TIME = 2E-06 SEC. PER DIVISION
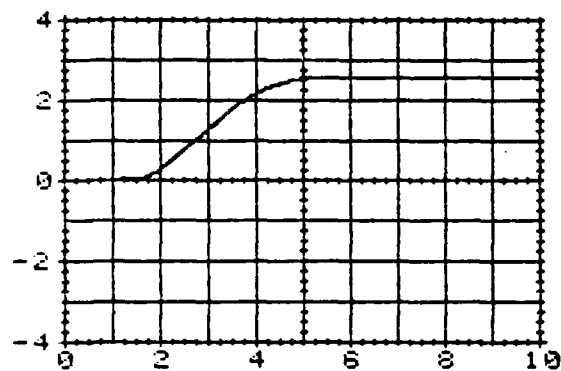
TRACE = ENERGY (JOULES)
SCALE =20 PER DIVISION
TIME = 2E-06 SEC. PER DIVISION
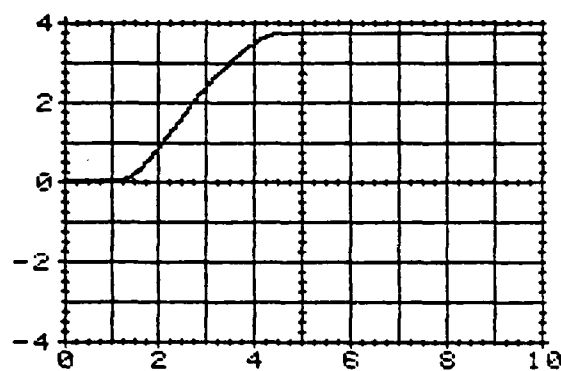
TRACE = ENERGY (JOULES)
SCALE =20 PER DIVISION
TIME = 2E-06 SEC. PER DIVISION

Figure 19 The Flashboard Impedance,
Power and Energy as Functions
of Time Corresponding to the
Current and Voltage Traces in
Figure 17.

Figure 20 As in Figure 19, but
Corresponding to Figure
18.

36

$\dfrac{\sigma N/P_{fb}}{(10^{10}\Omega^{-1}W^{-1}cm^{-2})}$

Negative Differential Conductivity
Oscillations (NDCO)

E/N $(10^{-16}\ Vcm^2)$
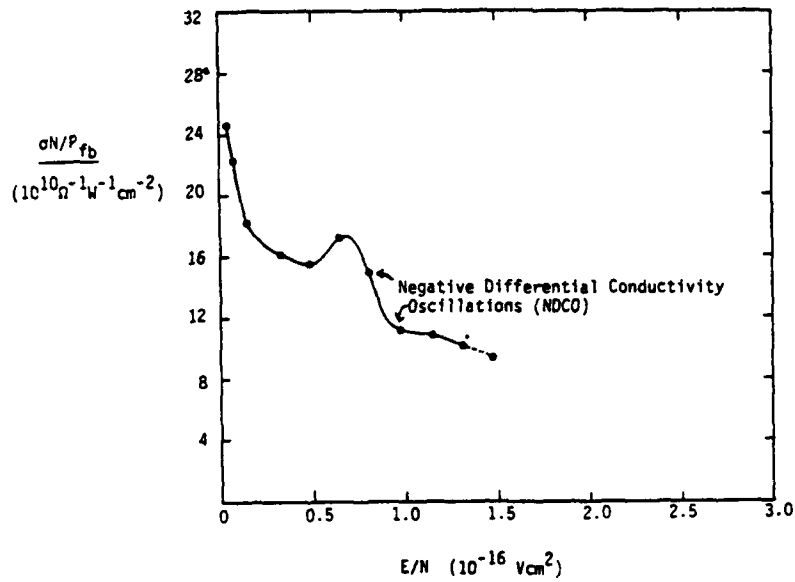
Figure 33. As in Fig. 29, 8:1 He:N$_2$ (10% CF$_4$)/TMA Data

$\dfrac{\sigma N/P_{fb}}{(10^{10}\Omega^{-1}W^{-1}cm^{-2})}$

NDCO

E/N $(10^{-16}\ Vcm^2)$

Figure 34. As in Fig. 29, He (10% CF$_4$)/TMA Data

50

Figure 31. As in Fig.29, 1:1 N_2:He (10% CF_4)/TMA Data

Figure 32. As in Fig.29. N_2 (10% CF_4)/TMA Data

Figure 29. The Scaled Conductivity as a Function of E/N for Several Gas Mixes. Note: $n_{TMA} = 4.3 \times 10^{15} cm^{-3}$ for all mixes

Figure 30. As in Fig. 29, N_2/TMA Data

48

In closed operation at $E/N = 8 \times 10^{-18}$ Vcm^2 and with $P_{fb} = 0.5$ MW/cm^2 this gives
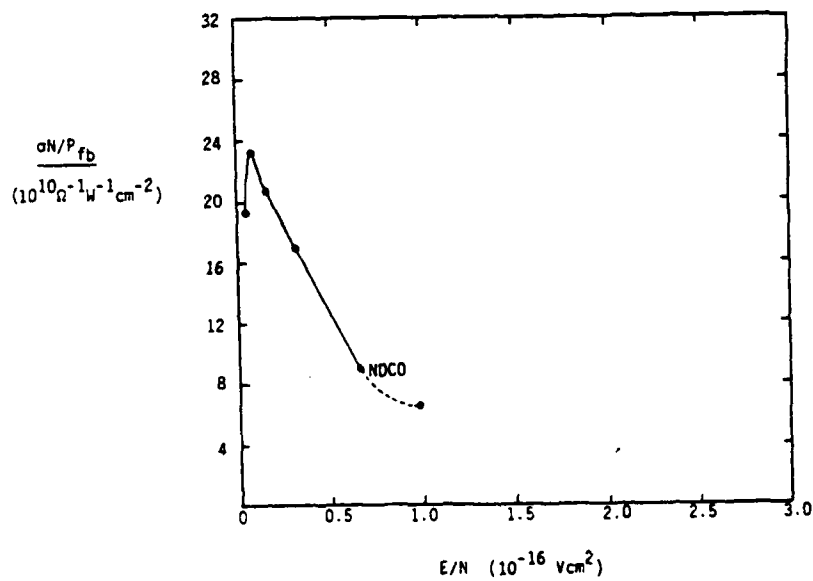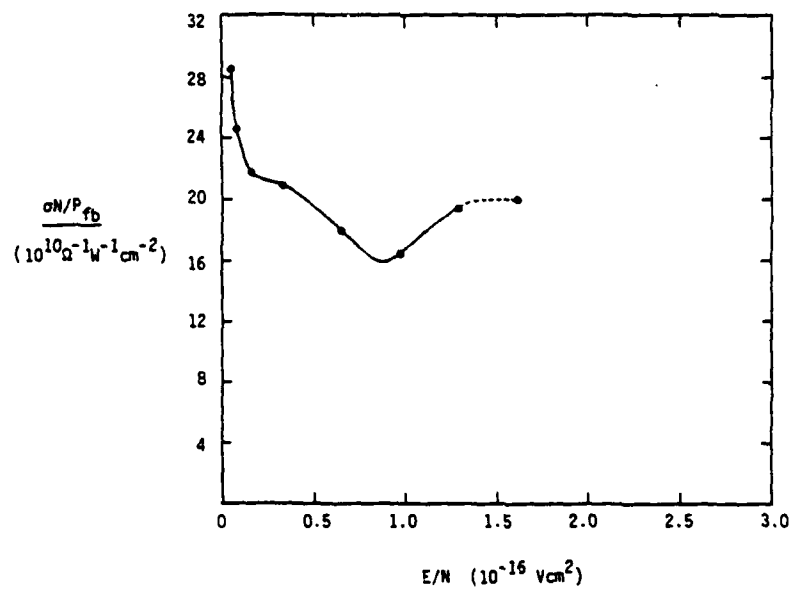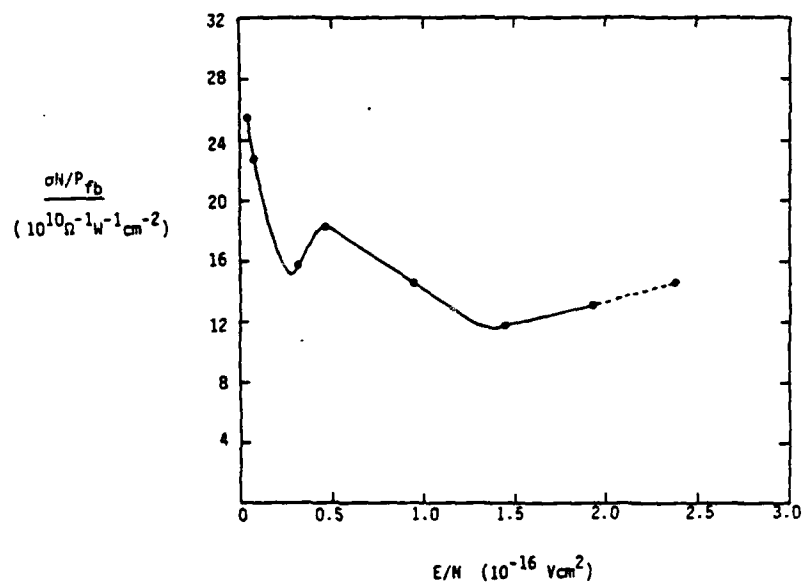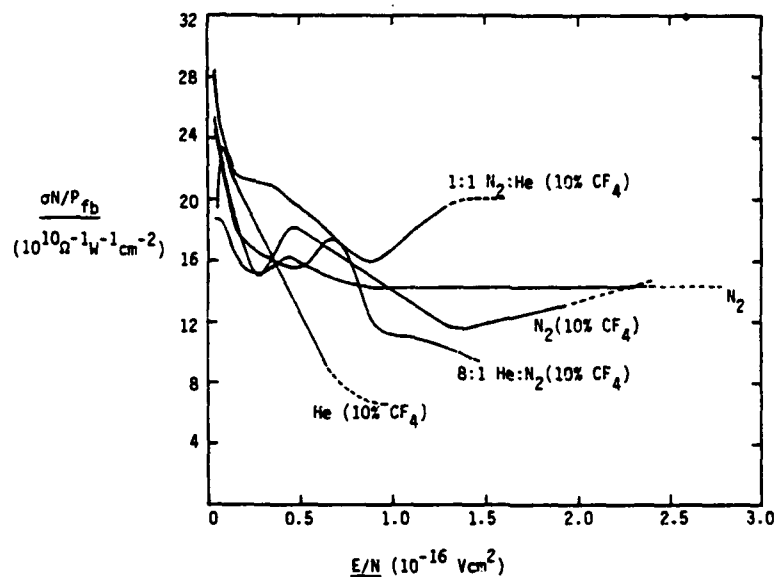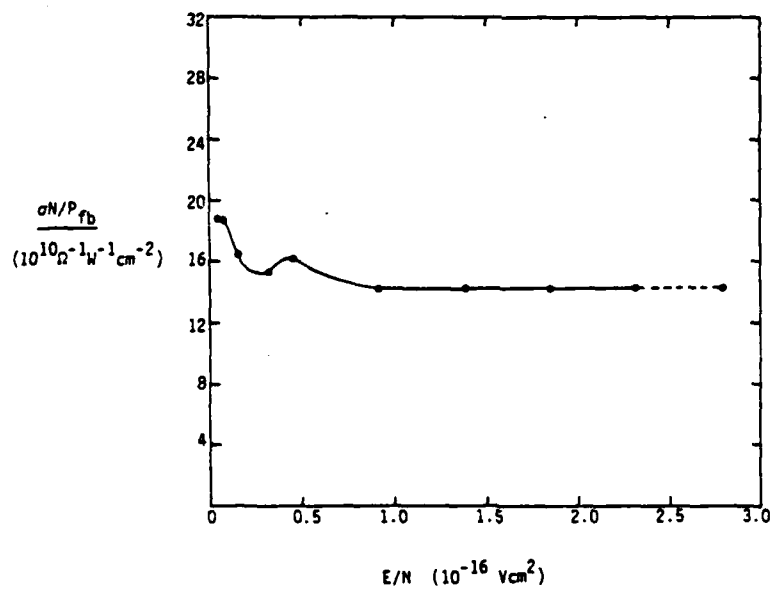
$$\sigma = 1.9 \times 10^{-3} \ \Omega^{-1} \ cm^{-1}$$

and $\qquad E = 490$ V/cm

yielding a current density;

$$J = \sigma E = 0.9 \ A/cm^2$$

Even though the switching ratio is 10 and the conductivity upon opening is reduced by a factor of 3 from the conductivity during closed operation, the current density during closed operation is quite low. If the discharge area is 1 m^2, then the total current is about 9 KA and the impedance is about 50 mΩ. This requires an external load impedance of about 0.5 Ω in order to achieve the desired switching ratio of 10.

It must be stressed again that the opening voltage limit given in Figures 29-34 is an energy loading limit for a 5.5μs discharge with effectively no external impedance. A high switch ratio means that most of the pulse energy will be dissipated or stored in the external load. In this case the E/N opening limits will probably be significantly higher than those given in these Figures. The values derived here are illustrative rather than quantitative. Even with high switch ratios, however, the opening voltage limit will be somewhat pulse length dependent. The effects of load impedance are illustrated in the following section.

It is evident that to switch high currents, or efficiently load low external circuit impedances with high switch ratios would require large discharge areas for the He/CF$_4$ mixture. Consider now the nitrogen without CF$_4$ conductivity curve (Fig. 30). The opening limit is at $E/N \approx 2.6 \times 10^{-16}$ V cm^2. For a switch ratio of 10, the closed operation value of E/N is about 2.6×10^{-17} Vcm^2. For the same switch conditions as just described the switch pressure is now 600 torr, or 0.8 atm, and the current density is 2A/cm^2. This gives a total current for a 1 m^2 electrode of 20 KA, with a corresponding impedance of 25 mΩ. Even though the peak scaled conductivity is lower than for the helium/CF$_4$ mix, the higher E/N opening limit gives a factor of two improvement in switch current for the same switch ratio and opening voltage.

47

where P_{fbmax} is the maximum flashboard power per unit area. It was decided, therefore, that the best comparison of the various gas mixes was to plot the parameter Sigma N/P_{fbmax} as a function of E/N. This is done in Figure 29 for various combinations of N_2, He, CF_4, and TMA with constant absolute TMA density. The dashed parts of the curves indicate the range in which the arc limit occurs. In all cases this range is much lower than the breakdown voltage and the opening voltage is limited by the discharge energy loading. In figures 30-34, each of these curves is presented separately.

There are several observations which can be made directly from these figures. As might be expected, the limiting opening voltage increases with the amount of nitrogen in the mix. For the mixes with nitrogen the conductivity does not vary smoothly with electric field, whereas the helium/CF_4 mix does. Comparing the nitrogen without CF_4 curve with the nitrogen with CF_4 curve indicates that the perturbations in the conductivity trace are enhanced by the CF_4. The mechanisms behind these variations in the conductivity are the dependancies of the attachment and recombination rates and the electron drift velocities upon E/N and are driven by the strong attachment cross section of CF_4 for high energy electrons (Ref. 6).

At first glance it appears that the helium/CF_4 mix might be the best mix for efficient opening switch operation, because it satisfies the criteria of high conductivity at low E/N and low conductivity at high E/N to improve both the switching time and the switch ratio. The maximum conductivity occurs at E/N $\approx 8 \times 10^{-18}$ Vcm^2 and the opening voltage limit occurs at E/N $= 8 \times 10^{-17}$ Vcm^2 leading to a switch ratio of about 10, which is quite reasonable.

There is a problem with this mix, however. The maximum conductivity occurs at a very low value of E/N. The scaling rules will be summarized later, but it is enlightening to consider a few scaling-parameters here. Consider, for example, a switch with an electrode separation of 10 cm, a flashboard power of 0.5 MW/cm^2, and a desired opening voltage of 50 KV. For the He/CF_4 mixture the following parameters are derived.

To open 50 KV at E/N $= 8 \times 10^{-17}$ Vcm^2 with d $= 10$ cm need;

P $= 2.5$ atm.
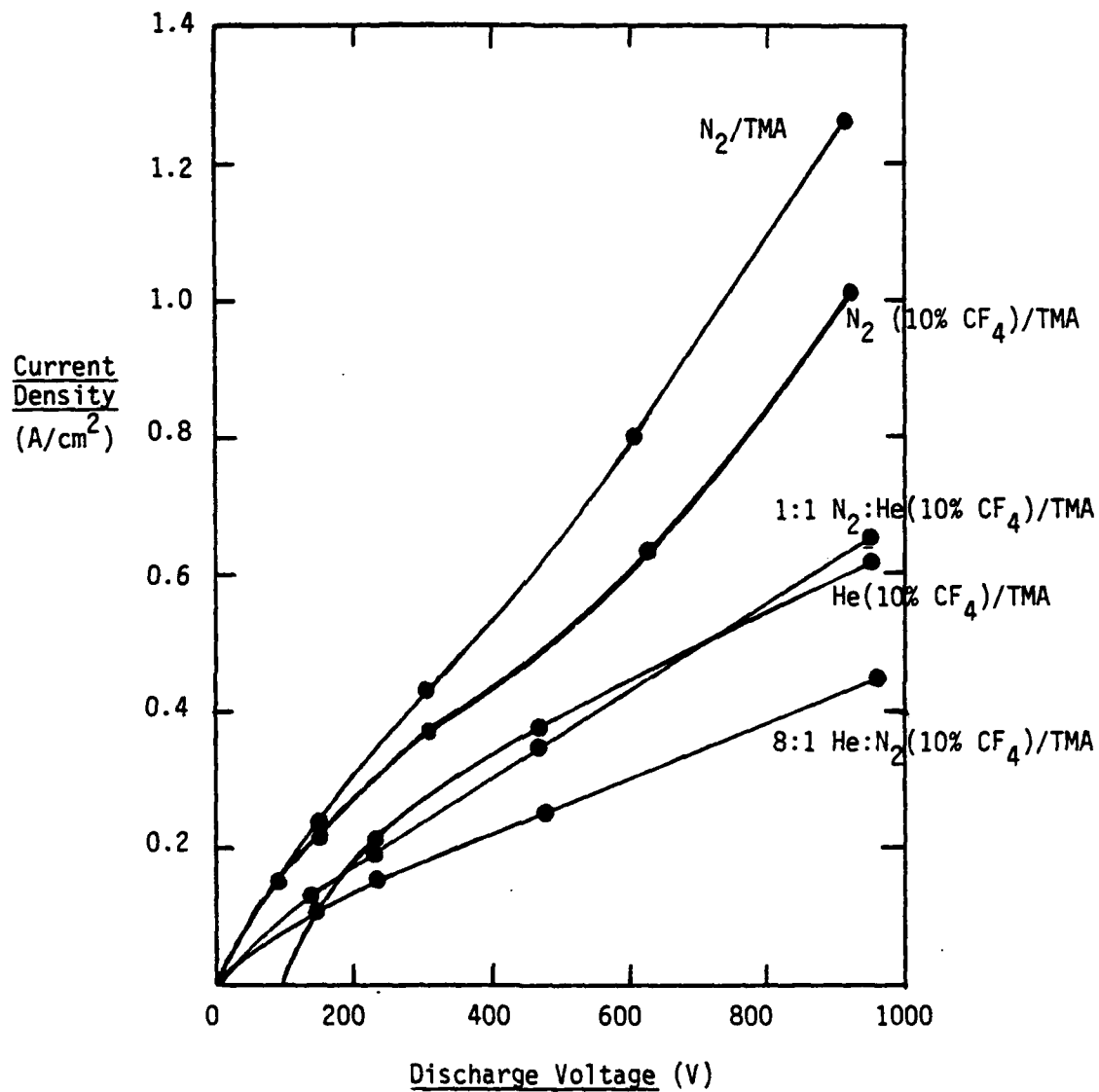
Figure 28. The Current Density as a Function of
Discharge Voltage for Several Gas Mixes
Note: $N_{TMA} = 4.3 \times 10^{15}$ cm^{-3} for all mixes

**a. Conductivity Measurements and Some Scaling
Considerations** -- The majority of the discharge experiments were untaken
with the screen electrode as the cathode. Figure 28 shows the maximum
discharge current density vs. voltage curves for several gas mixes at low
discharge voltage. The electrode spacing is fixed at 1.5 cm for each of the
mixes. The flashboard power and the gas pressure vary between mixes, even
though they are held constant for each mix. Figure 28 cannot be used to
directly compare the relative merits of the mixes, and the data must be
presented in another manner. Before doing this, however, an important
observation is made. For all the mixes which include N_2 there is no cathode fall
voltage drop. The He/CF_4 mix, however, does have a small cathode fall voltage
of about 80 V. This issue will be addressed later in this section, and in section
5.5.

Of greater interest than the current-voltage curves are the conductivities
as functions of E/N, however, and this must be taken into account. The
conductivity is given by:

$$\sigma = \frac{J}{E} = \frac{e \, n_e \, v_e}{E}$$
5.2.4

assuming that the electrons are the majority current carriers. The electron
drift velocity, v_e, is a function of E/N_x and the maximum electron number
density, n_{emax}, is given by equation 4.2.3. Unless the attachment and
recombination rate coefficients are known, as functions of E/N, the scaling of
the maximum conductivities with respect ot the maximum source strength are
unknown. Because of this, the following approach is used. As determined by
Westinghouse (Ref. 3) the time integrated source strength is proportioned to
spark energy. It is assumed, therefore, that the time varying source strength is
proportional to the flashboard power. Thus;

$$J_{max} = \sigma_{max} \, E = \sigma_{max} \, N \times \frac{E}{N}$$
5.2.5

$$\sigma_{max} = \sigma_{max} \left(\frac{E}{N}, \, P_{fb \, max} \right)$$
5.2.6

44

Using the curvefitting routine to analyze this and the 1, 2, 4, and 5 KV data it was established that there is good agreement with the photo-electron source strength relationships given in the Westinghouse report (Ref. 3), as summarized in Section 5.4. The relationship for TMA in N_2 is of the form;

$$S \propto \rho\, e^{-\beta \frac{p}{800}\rho x}$$

<div align="right">5.2.1</div>

where S is the photoelectron source strength, Beta is a constant measured by Westinghouse at 800 torr, Rho is the TMA seedant density in ppm, p is the pressure in torr and x is the distance from the flashboard surface. The corresponding Westinghouse equation has been changed to incorporate variable pressure and a one-dimensional photo-ionization flux as opposed to their single spark, spherical flux. Equation 5.2.1 can be used to determine the seedant density for the maximum source strength as follows. Look for a maximum such that;

$$\frac{\partial S}{\partial \rho} = \left(\frac{1}{\rho} - \frac{\beta \rho x}{800}\right) S = 0$$

<div align="right">5.2.2</div>

This yields;

$$\rho_{opt} = \frac{800}{\beta \rho x}$$

<div align="right">5.2.3</div>

By choosing a distance from the flashboard surface corresponding to the center of the discharge gap equation 5.2.3 yields a value of 325 ppm TMA at a pressure of 400 torr. If the seedant density is given in absolute terms rather than in parts per million, then for a given distance the optimum seedant density is constant, independent of pressure. This value is 4.3×10^{15} cm^{-3}. For the remainder of the experiments this was the value chosen for the TMA density.

The Westinghouse TMA data was given for an N_2, TMA mixture. The data is applicable for any mixture which does not absorb in the TMA photoionization wavelengths, however. Neither N_2 nor He have appreciable absorption in these wavelengths. Furthermore CF_4 was chosen as the attacher for these experiments because it has a small absorption cross section at these wavelengths as well. Mixtures with large concentrations of CF_4 could not be analyzed with the curvefitting routine, as explained in section 4.2 and the source strength could not be measured directly. With these considerations in mind it was assumed that as long as the CF_4 concentration was less than about 10% the source strength was effectively unaltered, and that the same relationship could be used to estimate its value for all the $N_2/H_e/$, CM_4/TMA mixes.

The effects of Penning ionization were relatively minor for most of the discharges and will be discussed in section 5.4.

<div align="center">43</div>

Photodetector
(1 V/div)

Current
(500 A/div)

2 μs/div
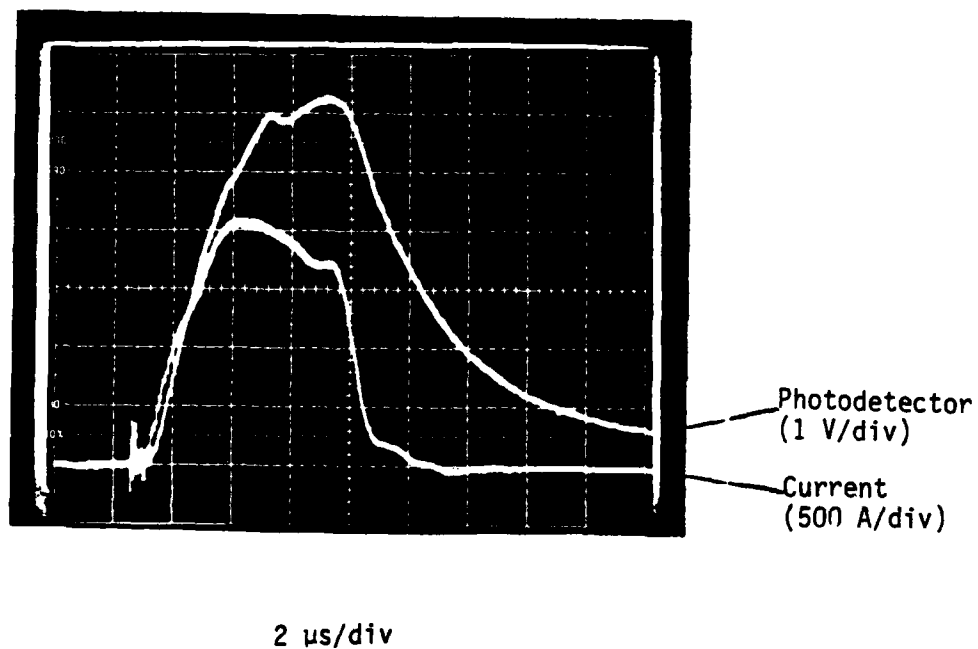
<u>Figure 27</u> The Flashboard Current and Photodetector Traces for the
same Conditions as in Figure 26.
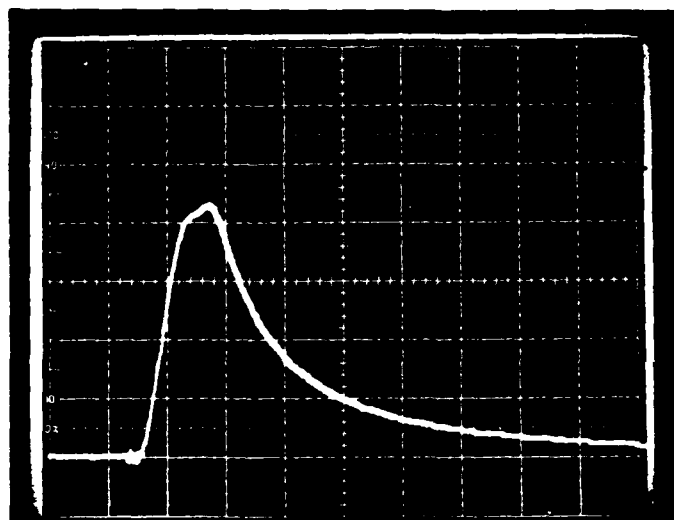
3 KV Discharge

50 A/div

5 μs/div
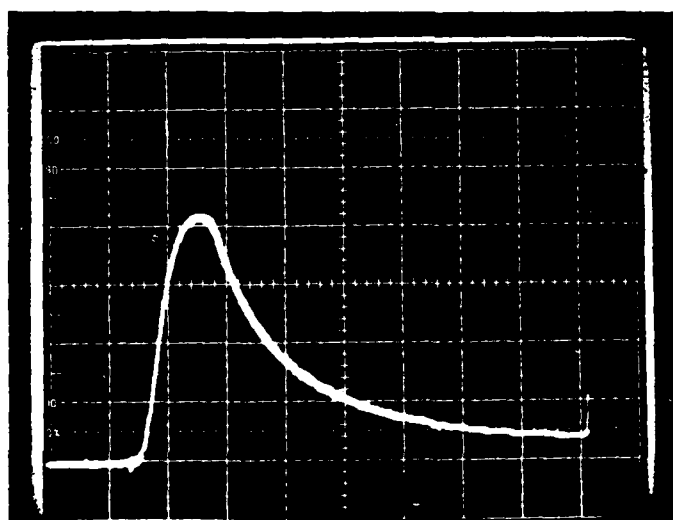
6 KV Discharge

100 A/div

5 μs/div

<u>Figure 26</u> The Discharge Currents with 3 KV and 6 KV across a 1.5 cm
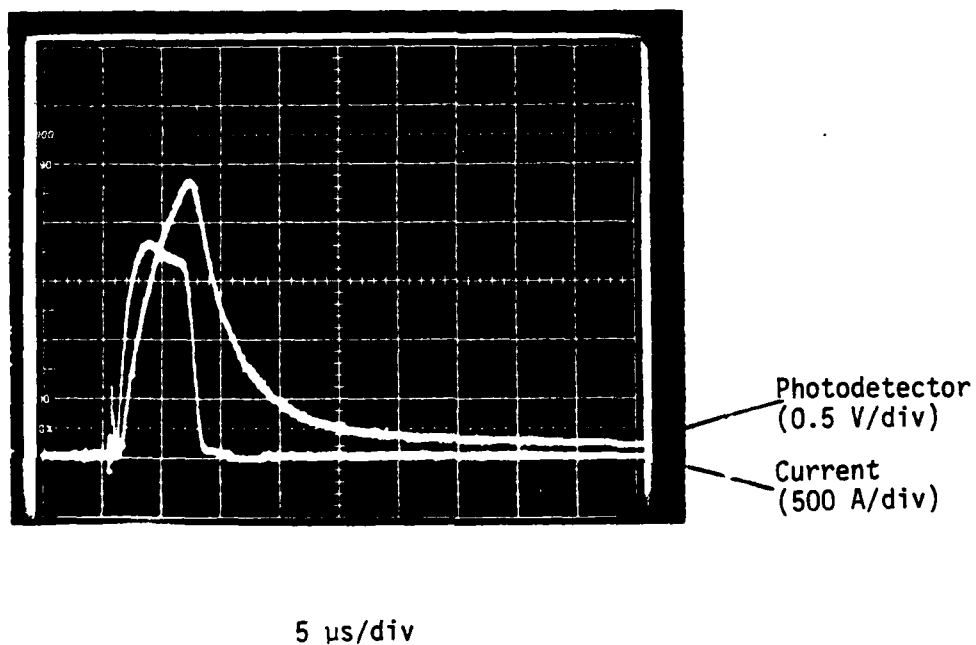Gap in N_2 with 100 ppm TMA and with a 12 KV PFN Charge.

41

5 μs/div

Figure 25   The Flashboard Current and Photodetector Traces for a
90/10 He/CF$_4$ Mix with a 10 KV PFN Charge.

photodetector does not measure the hard UV directly. The results of section 5.3 indicate however, that the photoionization UV flux follows the photocell trace closely. With this in mind, Figure 25 shows the flashboard current and photocell traces for a 90/10 He/CF$_4$ mix. Comparing Figures 8 and 25 it is seen that the e^{-2} decay time for each photocell trace is 8-10 μs. The same decay times are observed for all the gas mixes. This mixture independence implies that the long photocell decay time is likely due to light emission from the flashboard substrate surface. As described in section 4.3, this long UV decay time severly restricts switch opening times.

For the flashboard power densities required to provide acceptable switch conductivities the flashboard appears to have a lifetime of only 500-1,000 shots. For some purposes this might be adequate but longer lifetimes are generally desirable.

Because of the long switch opening times and relatively short lifetimes observed with the surface spark flashboard it appears that the development of a raised spark flashboard is desirable. Furthermore, raised sparks would give somewhat higher impedances, making impedance matching with high conductivity gases easier. Finally, the flashboard conditioning described earlier would probably not be necessary with raised sparks.

The series-spiral, surface-spark flashboard used for these experiments was adequate to obtain significant and meaningful data.

2. DISCHARGE MEASUREMENTS

Many switching experiments were undertaken for a variety of nitrogen and helium based gas mixes. Figure 26 shows the current traces for a mixture of N$_2$ with 100 ppm TMA at 400 torr, with 3 KV and 6 KV across the gap, which is set to 1.5 cm. The flashboard PFN is charged to 12 KV, with characteristics given by Figures 12 and 15. Figure 27 shows the corresponding photocell trace. As expected, with no attacher present the opening time is longer than the photocell decay time. The switching times are summarized in Section 5.3. Even though the switch is almost completely opened at 6 KV, the discharge eventually arcs. The breakdown voltage for this mix was measured to be 35 V/cm torr, corresponding to 21 KV at 400 torr with a 1.5 cm gap. The 6 KV opening limit is probably an energy loading limit rather than a pure voltage limit. The peak current at 6 KV corresponds to a current density of 5.3 A/cm^2. The traces are highly repeatable.
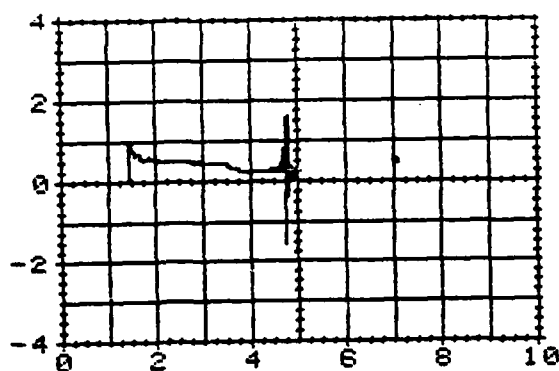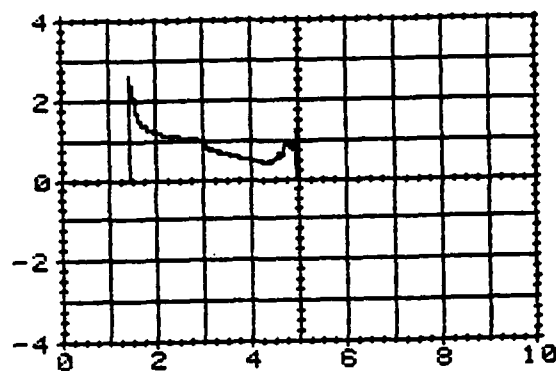
39

TRACE = IMPEDENCE (OHMS)
SCALE =5 PER DIVISION
TIME = 2E-06 SEC. PER DIVISION

TRACE = IMPEDENCE (OHMS)
SCALE =2 PER DIVISION
TIME = 2E-06 SEC. PER DIVISION
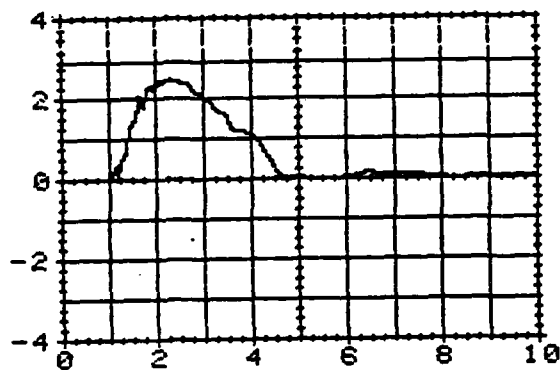
TRACE = POWER (WATTS)
SCALE =5000000 PER DIVISION
TIME = 2E-06 SEC. PER DIVISION

TRACE = POWER (WATTS)
SCALE =5000000 PER DIVISION
TIME = 2E-06 SEC. PER DIVISION

TRACE = ENERGY (JOULES)
SCALE =20 PER DIVISION
TIME = 2E-06 SEC. PER DIVISION

TRACE = ENERGY (JOULES)
SCALE =50 PER DIVISION
TIME = 2E-06 SEC. PER DIVISION

Figure 23 The Flashboard Impedance, Power and Energy as Functions of Time Corresponding to the Current and Voltage Traces in Figure 21.

Figure 24 As in Figure 23, but Corresponding to Figure 22.

38

TRACE = VOLTS
SCALE = 2000 PER DIVISION
TIME = 2E-06 SEC. PER DIVISION

TRACE = VOLTS
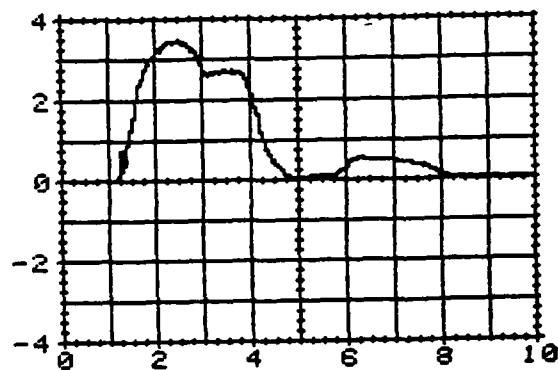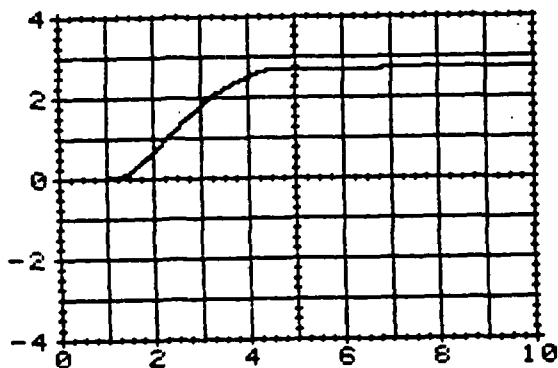SCALE = 2000 PER DIVISION
TIME = 2E-06 SEC. PER DIVISION

TRACE = CURRENT (AMPS)
SCALE = 500 PER DIVISION
TIME = 2E-06 SEC. PER DIVISION

TRACE = CURRENT (AMPS)
SCALE = 500 PER DIVISION
TIME = 2E-06 SEC. PER DIVISION

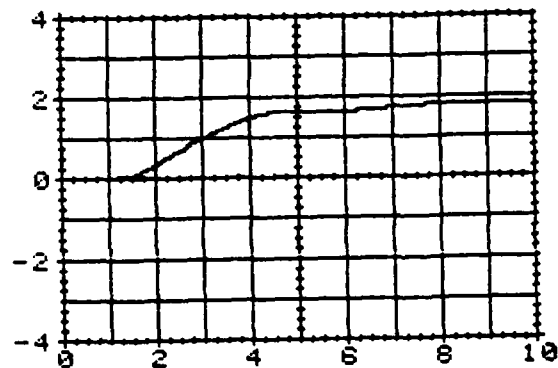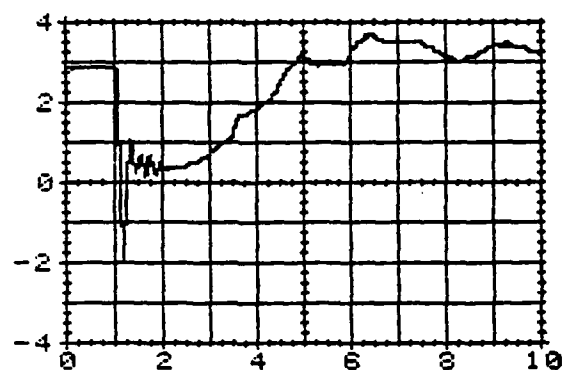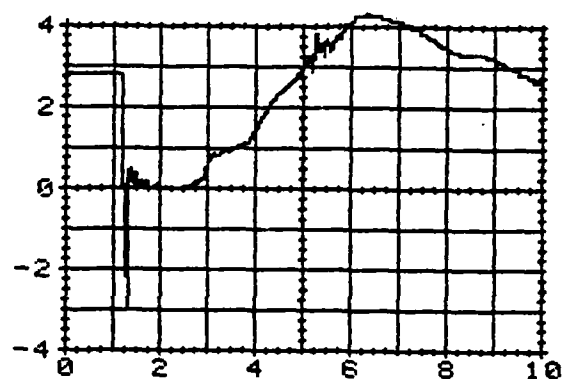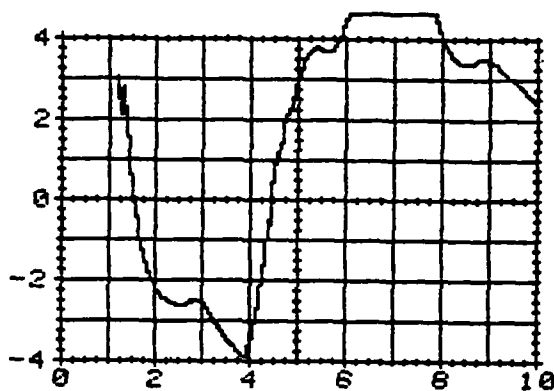Figure 21 Flashboard Current and Voltage
Traces for a 400 torr Mix of
90/10 He/N_2 with 100 ppm TMA
and with a 10 KV PFN Charge.

Figure 22 As in Figure 21, with a
12 KV PFN Charge.

37

Two further parameters of interest are the discharge efficiency, η_d, and the switch efficiency, η_s. They are defined as follows,

$$\eta_d = \varepsilon_d \; / \; (\varepsilon_d + \varepsilon_{fb})$$

and

$$\eta_s = \varepsilon_l \; / \; (\varepsilon_l + \varepsilon_d + \varepsilon_{fb})$$

where ε_l is the energy stored in the load, ε_d is the energy dissipated in the dishcarge and ε_{fb} is the total energy dissipated by the flashboard.

The discharge efficiency is only applicable with no load, and indicates the photo-ionization efficiency. The switch efficiency indicates the overall switch performance into a given load.

In the two examples just given the switch efficiency would be 7.7% for the He/CF$_4$ mixture and 15% for the N$_2$ mixture.

It is obvious from these simple scaling examples, which do not take into account the absorption length of the UV flux and other such considerations, that the switch ratio, opening voltage, efficiency, pressure, dimensions, current and impedance are all closely interrelated and that to specify one parameter independently of the others is meaningless. Furthermore, the external circuit is just as important. A switch cannot be designed from conductivity arguments alone, but must be designed for a specific-application over a certain range of parameters.

The results do indicate, however, that the potential parameter values are quite attractive for switch applications, even for non-optimized mixes. The main conclusion which can be drawn is that the optimum gas mix for a desired switch ratio will have a large E/N opening limit with a large conductivity maximum at a value of E/N equal to the inverse of the desired switch ratio times the E/N opening limit. This correlates to a combination of the best properties of the helium/CF$_4$ and the nitrogen mixes. None of the mixes tried completely fulfilled these criteria.

There are three further observations to be made from Figures 29-34 The electron drift velocity in helium is much greater than in nitrogen (ref. 7), yet the measured conductivities do not vary very much, especially at lower values of E/N. This is explained as follows. The greater the percentage of helium, the

51

greater the drift velocity, but the lower the strength of nitrogen 108 nm wavelength emission from the flashboard. With helium and nitrogen based mixes with TMA as a photoionization seedant higher drift velocity is offset by lower ionization efficiency. The 1:1 $N_2:H_e$ mix with 10% CF_4 seems to give the best compromise between these competing effects.

The next observation is the presence of negative differential conductivity oscillations (NDCO) in the two mixes with greater than 50% helium. The current at these points was actually decreasing with voltage. Figure 35 shows an example of the NDCO. This phenomenon is explained as follows. The mixes with high helium concentration will have high drift velocities with correspondingly large high energy tails to the velocity distribution functions. The CF_4 was chosen as an attacher because it has a larger attachment coefficient at high electron energies, as stated in the introduction to this report. Consequently the high energy tail is quenched by the CF_4. As the discharge voltage increases more electrons are lost by attachment and if this effect is strong enough the current can actually decrease as observed in these experiments. This leads to a negative differential conductivity, with its corresponding oscillations (Ref.8).

The final observation is made in relation to the cathode fall voltages, or lack thereof, measured from Figure 28. As the value of E/N approaches zero, the conductivities of all the nitrogen containing mixes are increasing. Only the helium/CF_4 mix has rolled over and is decreasing. This phenomenon is explained by electrode secondary photoelectron emission discussed in section 5.6. It might be expected that the current density at low discharge voltages might have a discharge polarity dependence. Figure 36 shows the current density vs. voltage curves for a N_2/TMA mix with the screen electrode acting as both the cathode and as the anode. At low voltage the screen anode gives higher current densities, whereas at higher voltage the screen cathode gives the higher current densities. This phenomenon is also explained in section 5.6.

The various observations lead to the conclusion that mixes with about equal fractions of nitrogen and helium may be optimum for opening switch operation. The optimum amount of TMA depends upon the electrode separation, and the optimum amount of CF_4 cannot be derived until more rapid source decay times are obtained. It is likely, however, that a values up to about 10% CF_4 will provide the best compromise between opening time and conductivity.
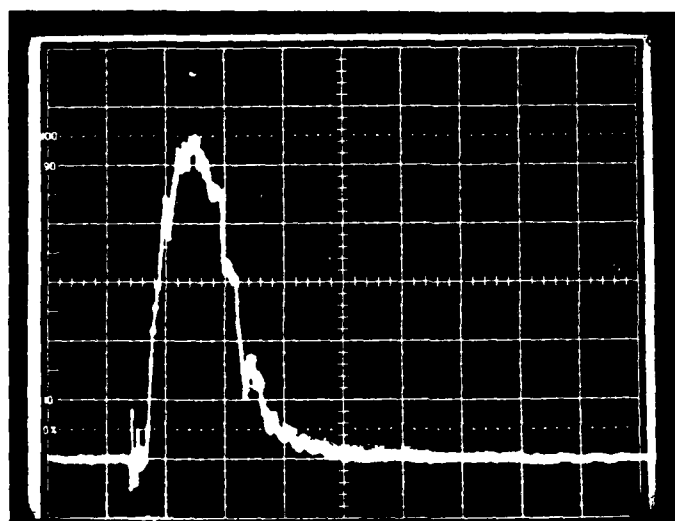
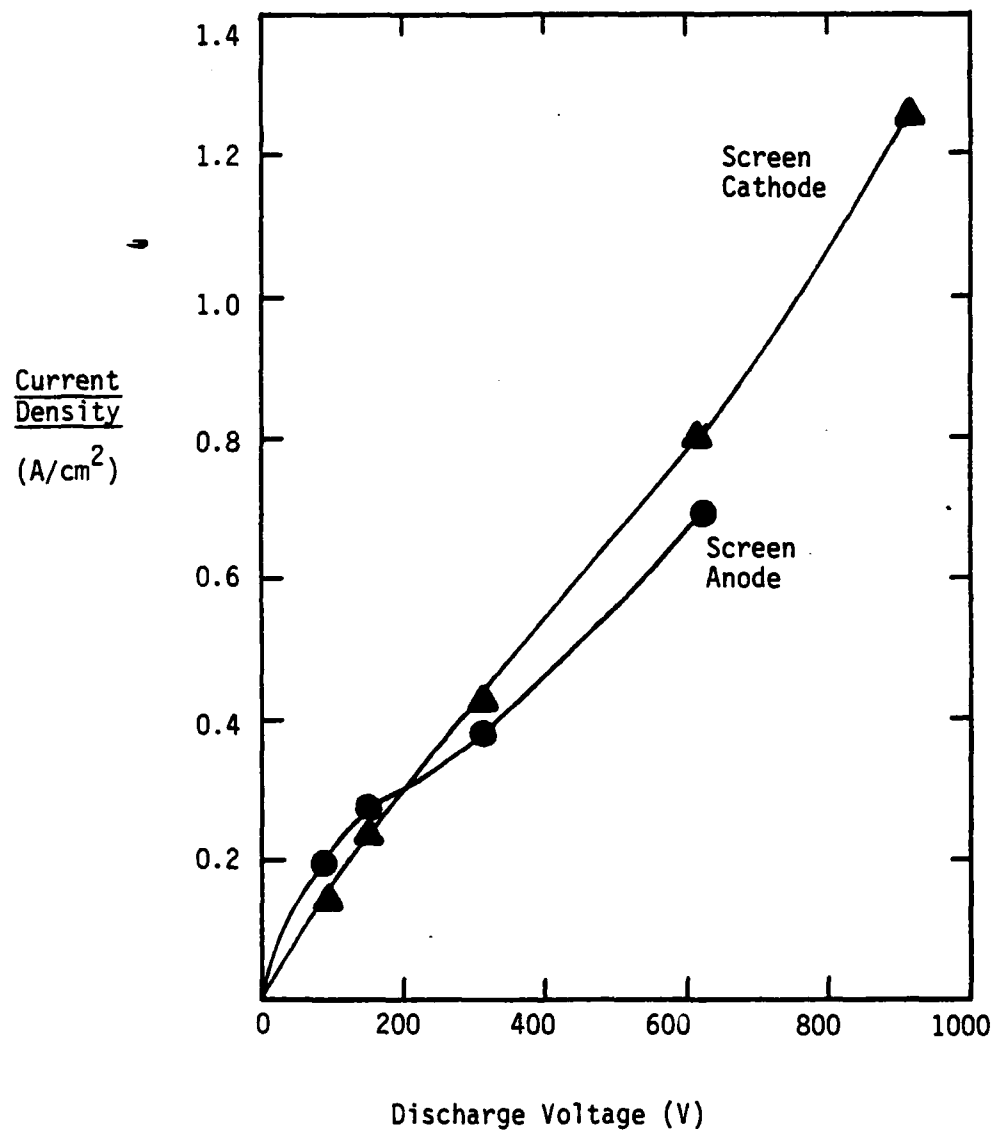2 KV Discharge

Current
(10 A/div)

5 µs/div

Figure 35 A Discharge Current Trace Showing NDCO. Gas Mix is
He with 10% CF_4 and 230 ppm TMA at 600 torr with a
10 KV PFN Charge.

53

Figure 36 The Current Density as a Function of
Discharge Voltage for a N_2/TMA Mix
for Different Discharge Polarity.

54

b. External Load Effects-- A series of experiments was run to indicate the effects of the external circuit impedance upon switch operation. NO was used as an attacher for these experiments. Using the Westinghouse data (Ref. 3) it was determined that 0.43% of NO in nitrogen at 400 torr would provide the optimum photoelectron source strength. Figure 37 shows the current traces for a 4 KV and a 7 KV discharge with 1 Ω in series with the switch. In each case the minimum discharge impedance is about 14 Ω (excluding the arc at 7 KV). Figure 38 shows the current traces for a 7 KV and a 10 KV discharge with 42 Ω in series. With the voltage drop across the 42 Ω resistor taken into account the discharge impedance is now about 4 Ω and the switch ratio at the arc limit is 13.

Apart from the obvious effect that the arc limit, or opening voltage limit, increased with placing the load in series there are several other comparisons which can be made. With 1 Ω in series 96% of the main circuit energy was loaded into the discharge, which had an energy loading limit of about 24 J. With 42 Ω in series 59% of the main circuit energy was now loaded into the resistor, and the energy loaded into the discharge at the arc limit was only 11 J. This illustrates that with a small load the discharge is energy, or $J \bullet E$, limited, whereas with a larger load the discharge is now voltage, or E/N, limited.

Finally, the total flashboard energy for these experiments was 55.4 J/shot. Using the definition for the switch efficiency given in the previous section (as opposed to the discharge efficiency defined in section 2.D) gives an efficiency of 1% into the 1 Ω resistor and an efficiency of 19% into the 42 Ω resistor. This further illustrates how sensitive the switch performance is to the external circuit characteristics.

55
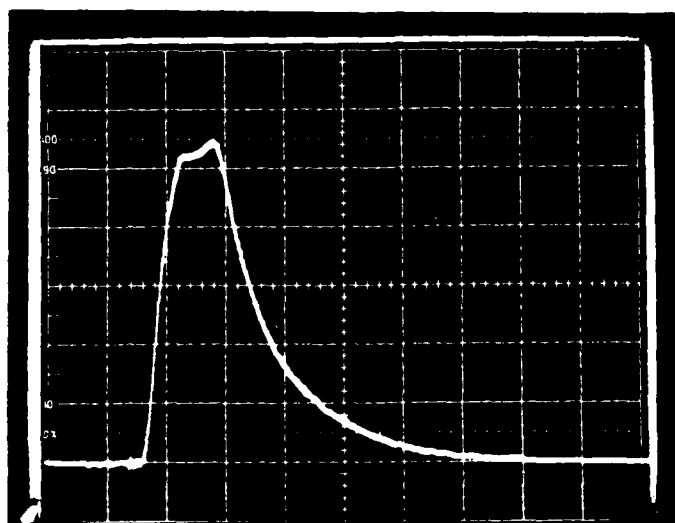
4 KV Discharge

Current
(50 A/div)

5 µs/div
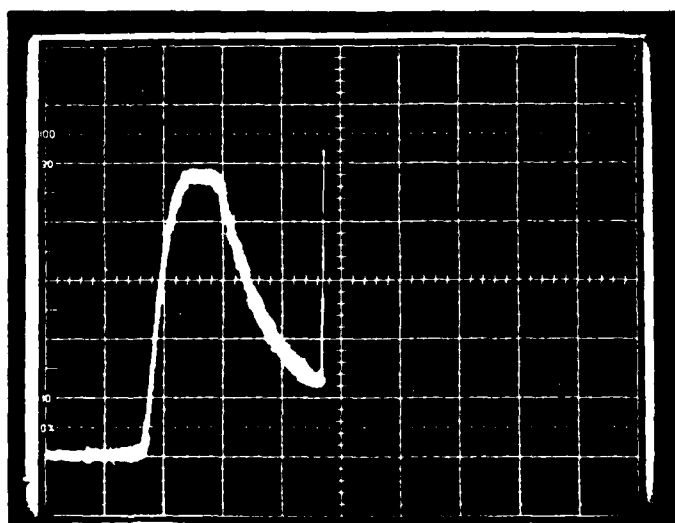
7 KV Discharge

Current
(100 A/div)

5 µs/div

Figure 37   Discharge Currents in a N$_2$ 0.43% NO Mix with a 1.5 cm Gap and
with 0.9 Ω Series Resistance. PFN Charge is 12 KV.

56
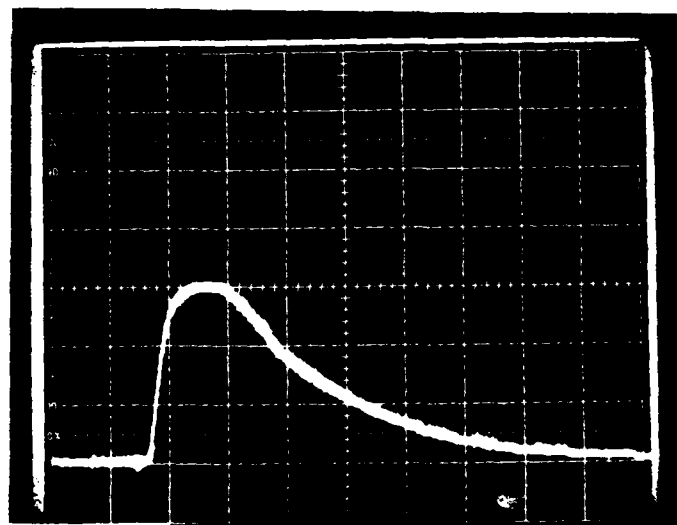
7 KV Discharge

Current
(50 A/div)

5 µs/div
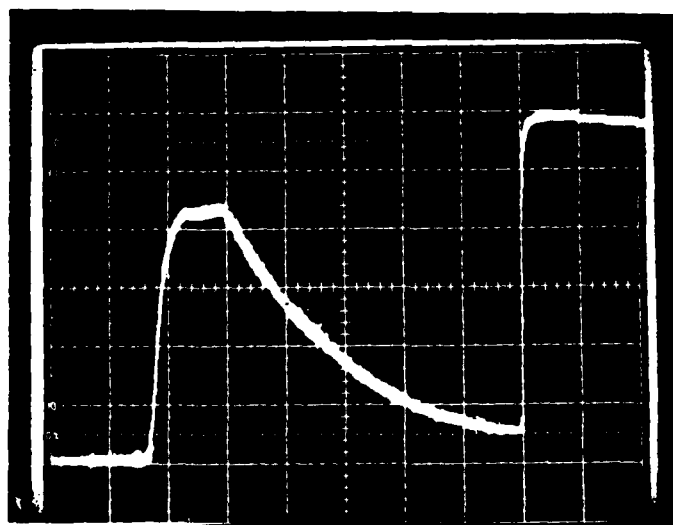
10 KV Discharge

Current
(50 A/div)

5 µs/div

<u>Figure 38</u> As in Figure 37 but with Different Discharge Voltages and
with 42 Ω Series Resistance.

c. Conclusions-- There are three important conclusions to be drawn from the conductivity measurements.

(1) The switch current, switch ratio, efficiency, opening voltage limit, and external circuit impedance are all interrelated. It is meaningless to specify one parameter independently of the others.

(2) The results from a small scale experiment cannot be directly scaled to larger switches. Rather, the conductivity values (and attachment and recombination rate coefficients, etc.) which are measured can be used to model the performance of a larger switch. Of particular importance is the fact that the optimum photoionization seedant density is a strong function of the switch geometry which will have an impact in scaling to large electrode separations.

(3) The external circuit characteristics for any particular switch application must be incorporated in the design of the opening switch.

3. SWITCHING TIMES

As previously stated the switch opening times were apparently limited by the surface photoemission decay times, rather than by either the gas mix or the PFN flashboard control. Aside from this issue, there are several conclusions which can be drawn.

Figure 39 shows the current and UV rise and decay times as measured by the photodetector for 400 torr N_2 with 100 ppm TMA and 12 KV on the PFN. The current rise time is 3 μs, whereas the UV rise time is 4 μs. At first this discrepancy was thought to be related to pumping of the nitrogen vibrational manifold, but exactly the same phenomenon was observed with helium/CF_4/TMA mixes. This independence of gas mix again points to substrate surface effects. The 90% decay of the photodetector trace is approximately 11μs.

Figures 40 (a) and 40 (b) show the corresponding discharge current traces for a 1 KV and a 4 KV discharge, respectively. In both cases the 90% closing time is 4 μs, corresponding with the photodetector 90% rise time. For the 5 KV discharge, however, the 90% opening time is 23 μs.

The same phenomena were observed with every gas mix. The switch closing time in every case corresponded with the UV as measured by the photodetector rise time. The best opening times corresponded with the photodetector decay times, but were frequently much longer, depending upon the gas mix attachment and recombination coefficients. For the discharges in Figure 40 it is seen that the rate coefficients are decreasing with E/N, as summarized in the next section.

It is concluded that for surface sparks with power densities of the order used for these experiments the best closing time possible is about 1 μs, for a perfectly square flashboard current pulse, and the best obtainable 90% opening times are about 6 μs. Both these times are apparently limited by surface substrate radiation, and changing to a raised spark configuration should significantly improve the switch performance.

59
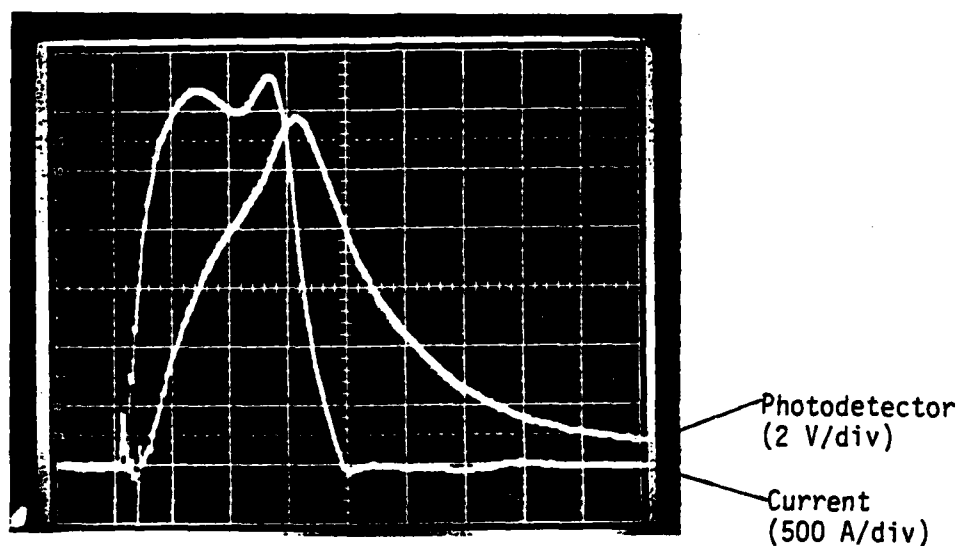
2 μS/div

Figure 39 Flashboard Current and Photodetector Traces for a Mix
of N_2 with 100 ppm TMA at 400 torr and with a 12 KV PFN Charge.
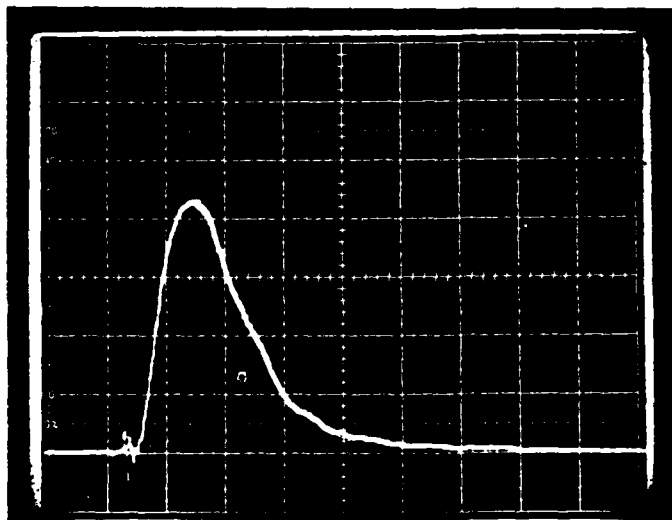
40(a)

1 KV Discharge

Current
(20 A/div)

5 μs/div
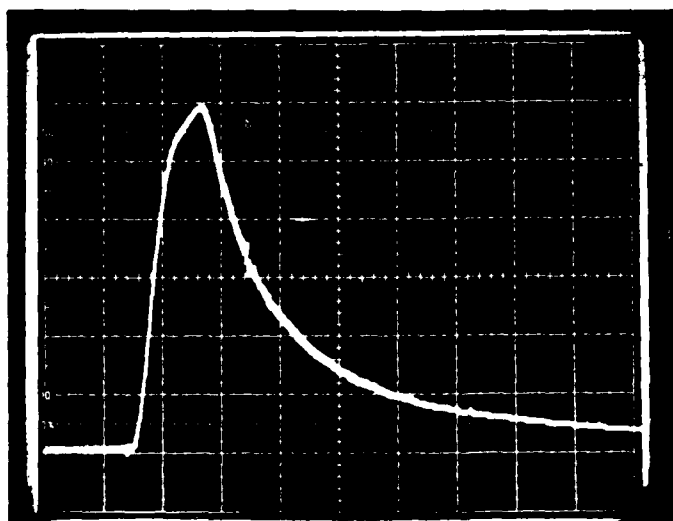
40(b)

4 KV Discharge

Current
(50 A/div)

5 μs/div

Figure 40   The Discharge Current Traces Corresponding with Figure 39
for Two Discharge Voltages.

4. ATTACHMENT, RECOMBINATION AND SOURCE STRENGTH MEASUREMENTS

There are two points to be made in relation to this section. The first is that in every discharge the voltage is less than the self-sustained glow voltage to the extent that Townsend ionization is negligible. The second point is that in all the gas mixes the spark spectrum is such that there is negligible photo-ionization of either the nitrogen or the helium. The only source of ionization, therefore, is photo-ionization of seedants within the discharge. The seedants may be contaminants or added gases such as TMA. If the external source were an e-beam or x-rays then this argument would not hold and there would be a significant number of ions of nitrogen or helium present.

The least squares curve fitting-routine described in section 4.2A was used to acquire data for several gas mixes. Because of the long source decay times observed with the surface sparks the gas mixes which could be analyzed with this routine were limited to those with relatively small attachment and recombination coefficients.

Figure 41 shows the attachment rate coefficients obtained for two N_2 mixes, one with 100 ppm TMA and one with 325 ppm TMA. Figure 42 shows the corresponding recombination rate coefficients. These values were obtained by using the known values of the electron drift velocity in N_2 (ref 7). The attachment and recombination rates given in figures 41 and 42 are significantly different from the known values in pure N_2 (Ref. 9). This is expected because in these mixes, as just stated, the majority of the ions are those of TMA and its fragments, with negligible ionization of the nitrogen. The discharge physics is, therefore, dominated by the TMA and the nitrogen acts as a buffer gas, fixing the electron velocity distribution. Furthermore, the relative composition of the TMA and its fragments is a function of both the TMA density and the source strength (which is partly a function of the TMA density), and the attachment and recombination rates are observed in figures 41 and 42 to be nonlinear functions of the TMA density. When an attacher, such as CF_4 or NO, is added then this effect will be masked and the TMA will simply determine the photoelectron source strength.

The source strengths which were determined by the curve fitting-routine were;

$$S \ (100 \ ppm) = 2.2 \times 10^{18} \ cm^{-3} \ s^{-1}$$

$$and \ \ S \ (325 \ ppm) = 3.1 \times 10^{18} \ cm^{-3} \ s^{-1}$$

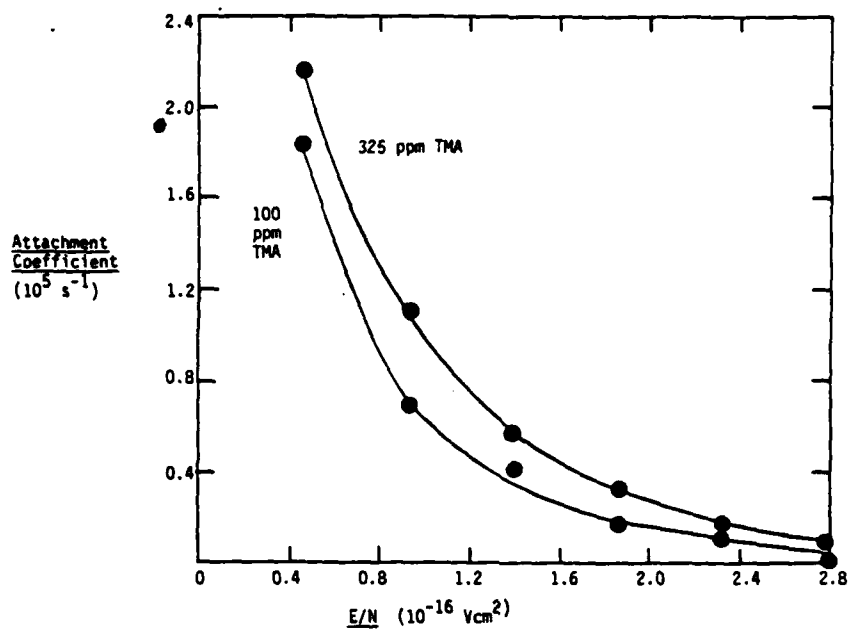Figure 41 The Attachment Rate Coefficient in Mixture
of N_2 with 100 ppm and 325 ppm TMA at 400
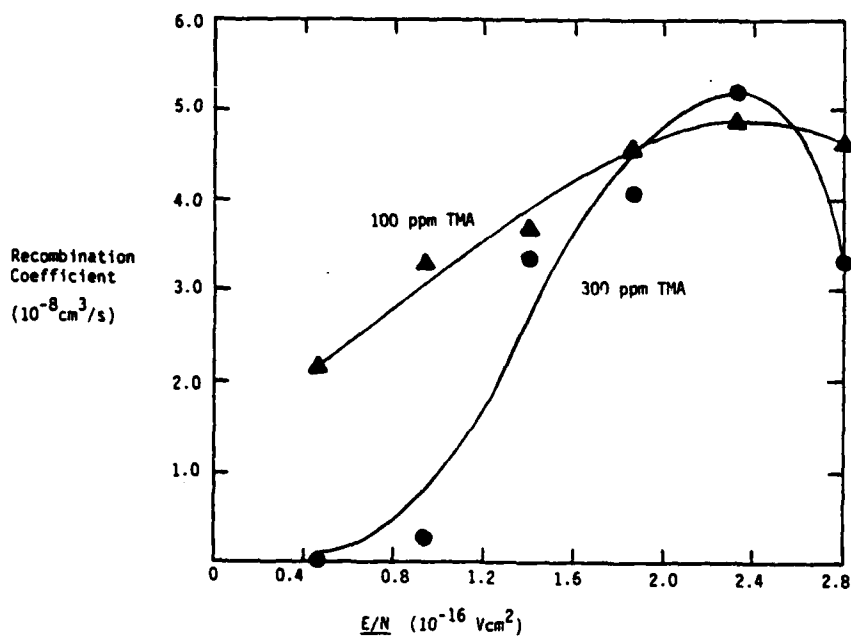torr, as Evaluated by the Curve Fitting Routine.

Figure 42 The Recombination Rate Coefficient as Evaluated by
the Curve Fitting Routine for the same Conditions
as in Figure 41.

The first point noted is that there was no conclusive evidence in these discharges of Penning Ionization of the TMA by the N_2 vibrational manifold. This is probably because the energy loading was too small, and much longer run times than the discharges in these experiments will be needed for Penning-ionization to become significant.

Adapting the source strength relationships obtained by Westinghouse (ref. 3) to a one-dimensional geometry, and for a flashboard power rather than a flashboard energy yields the relationship:

$$S = tr \times (0.5-1) \times A_\rho P_{fb} \; e^{-\beta \rho x}/Area$$

where A and ß are gas mix dependent constants, ρ is the seedant density. P_{fb} is the total flashboard power and tr is the screen electrode transmissivity. If there were no surface radiation then only half the flux would reach the discharge. If all the UV flux striking the substrate is re-radiated, then the total available flux will reach the discharge. Using the Westinghouse values for the values of A and ß, and scaling the value of ρ relative to one atmosphere pressure yields the results;

$$S(100 \, ppm) = 1.1 - 2.1 \times 10^{18} \, cm^{-3}s^{-1}$$

$$S(325 \, ppm) = 1.7 - 3.5 \times 10^{18} \, cm^{-3}s^{-1}$$

Comparing these values with the experimental values derived with the curve fitting routine, it is apparent that UV re-radiation from the substrate is very important. This gives very good flashboard efficiency, but leads to the opening time limitations already described. Using raised sparks should help in reducing the opening time, but may reduce the flashboard efficiency by nearly a factor of two. It is noted that the photoelectron source strength does not vary linearly with the TMA density.

It is concluded that the least squares curve fitting routine is a valuable tool in understanding the discharge kinetics. For long source decay times, however, the two parameter curve fit is not sufficient, and the three parameter curve fitting routine described in Appendix A should be used. Unfortunately the micro computer used reduce the data obtained in these experiments not only had limited memory, constraining us to the two parameter curve fit, but was also very slow. It would frequently take several hours to converge to a solution, depending upon the accuracy of the initial guess and the number of

64

where

$$W = R_s \sqrt{C/L} \qquad \text{6.2.7}$$

evaluated at the ring up time

$$t_f = \pi \sqrt{LC} \qquad \text{6.2.8}$$

The energy stored in the inductor is

$$E_L = \frac{1}{2} LI^2 \qquad \text{6.2.9}$$

or

$$E_L = \frac{1}{2} LA^2 e^{-\frac{R}{L}t} \sin^2\left(\frac{t}{\sqrt{LC}}\right) \qquad \text{6.2.10}$$

For the remainder of this analysis it is assumed that ring up has occurred, i.e.

$$E_L = \frac{1}{2} LA^2 e^{-W\pi} \qquad \text{6.2.11}$$

Therefore, the ratio of energy dissipated to energy stored is

$$\frac{E_{diss}}{E_L} = \frac{2}{W^2 + 4} \ [2(e^{W\pi}-1) - W^2] = r$$

Note: $\lim_{W \to 0} r = 0$ \qquad 6.2.12

$\lim_{W \to \infty} r = \infty$

For the purpose at hand, it is desired that r be as small as possible. For small w, r is given by

$$r \approx W\pi \qquad \text{6.2.13}$$

Important parameters are:

$$r = W\pi = \pi R_s \sqrt{\frac{C}{L}}$$

$$t_f = \pi \ LC$$

78
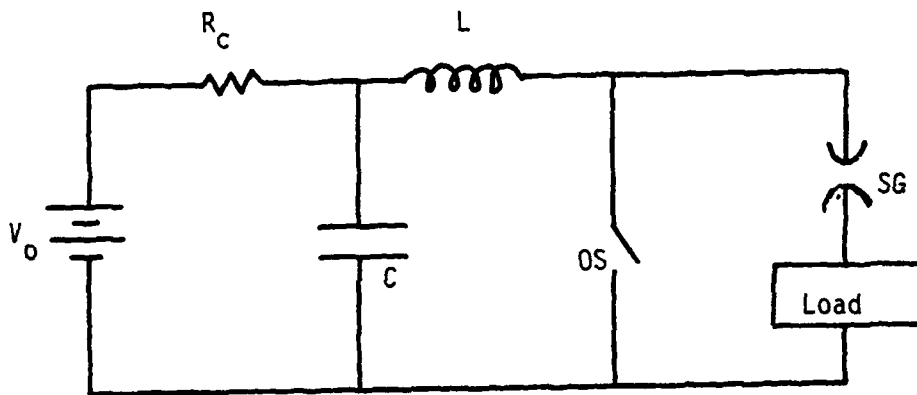
V_o is the main energy source

R_c is the charging resistor

C is the main storage capacitor

L is the inductor

OS is the opening switch

SG is a spark gap

Figure 49 A Typical Opening Switch Configuration.
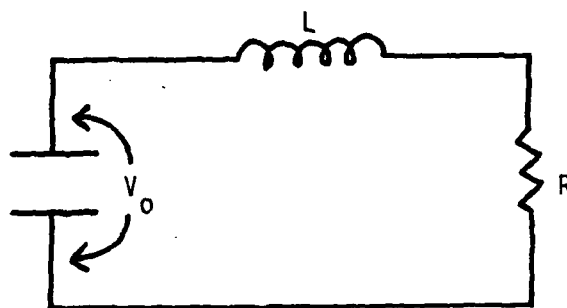
Figure 50 The RLC Circuit

2. SCALING GUIDELINES FOR A RESONANT CHARGE RLC CIRCUIT

A typical resonant charging opening switch configuration will look something like figure 49.

The opening switch (OS) is known to have some switch impedance (R), assumed constant. This being the case, it is desirable to know the amount of energy absorbed by the switch compared to the amount of energy stored in the inductor.

First assume the capacitor (c) is fully charged. Consider then the circuit in figure 50, where R_S is the switch operating impedance.

The differential equation governing this circuit is:

$$\frac{1}{c} \int I \, dt + L \frac{dI}{dt} + I \, R_s = 0$$

6.2.1

Differentiating this equation results in:

$$\left(\frac{1}{c}\right) I + L \frac{d^2 I}{dt^2} + R_s \frac{dI}{dt} = 0.$$

6.2.2

which has a solution

$$I = A \, e^{-\frac{Rs}{2L}t} \sin\left(\frac{t}{\sqrt{LC}}\right) \text{ if } R_s \ll 2\sqrt{\frac{L}{C}}$$

6.2.3

Where A is given by

$$A = I_{max} e^{\pi \left(R_s/2\right)\sqrt{C/L}}$$

6.2.4

The power dissipated in the switch is

$$P_{diss} = I^2 R_s$$

6.2.5

Time-integrating Eq. 6.2.5 gives the energy dissipated:

$$E_{diss} = \frac{A^2 L}{W^2 + 4} \left[2 - e^{W\pi}(W^2 + 2)\right]$$

6.2.6

76

times, the energy stored in the total inductance is very small, but the effi-ciency is excellent. This is where the trade-off must be made. As would be intuitively expected, the lower the total pure impedance and the higher the total inductance, the better the performance.

There are several circuits of interest. Firstly, if the charge source has effectively zero output inductance and impedance, $L = L_L$ and $R = R_s$, all the inductive energy will be available for use. If the output impedance and induc-tance are significant, and if the energy stored in the power supply output inductance is not accessible, then only the fraction;

$$E_{L \text{ effective}}(t) = L_L/(L_c + L_L) \times E_L(t) \qquad (6.1.11)$$

will be available for use.

Finally, if the energy stored in the power charge inductance is ac-cessible, then this inductance may be considered part of the load inductance (or may be the total load inductance, e.g., with a homopolar generator) and, once again, the energy stored in the total inductance is available for use.

An example is given in the following section to compare the RL circuit with the RLC resonant charge circuit.

$E_T/(V_c^2 L/R^2)$

V_R/V_c & $I/(V_c/R)$

Parameter
Value

$E_L/(V_c^2 L/R^2)$

E_L/E_T

V_L/V_c

Rt/L
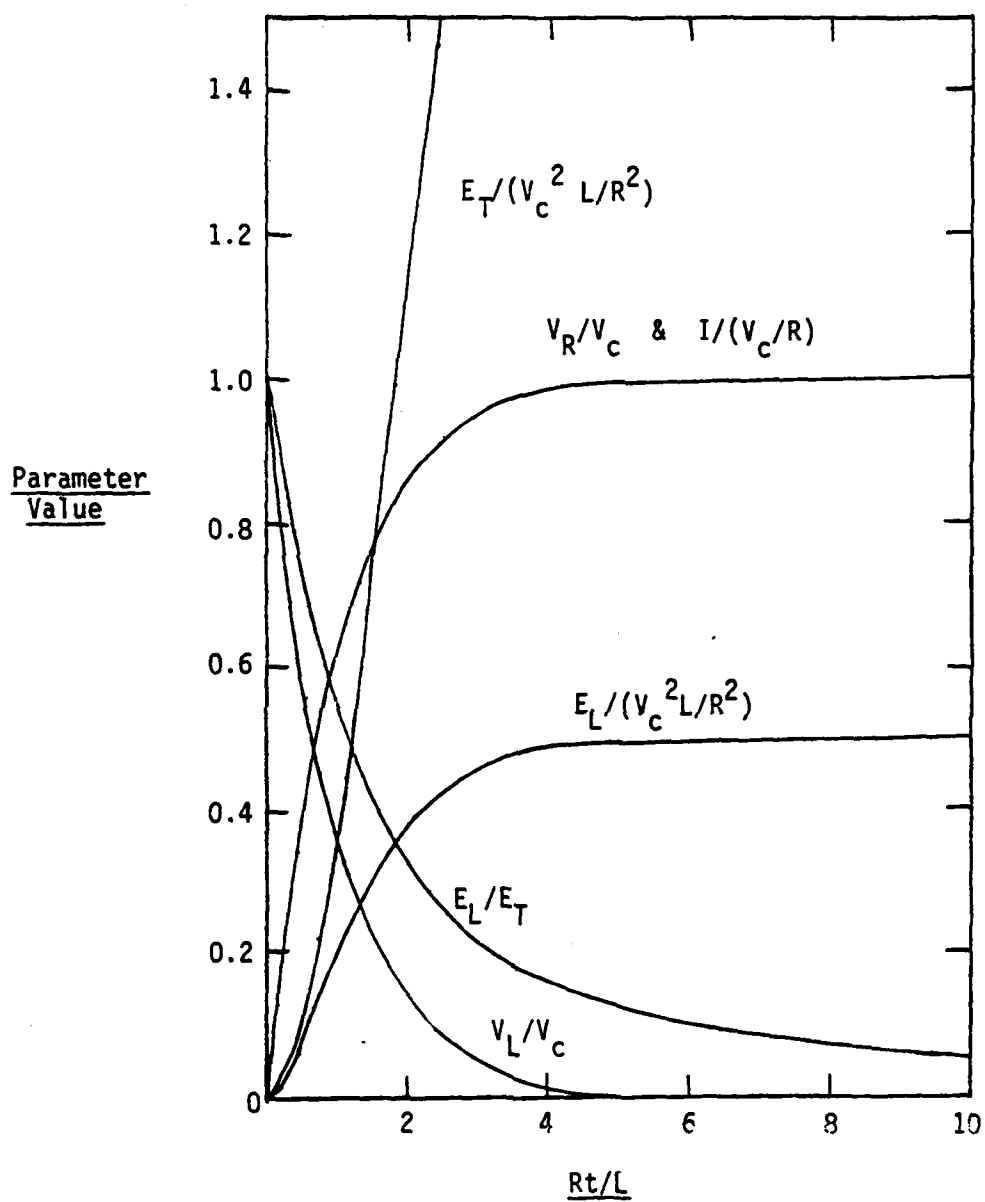
Figure 48   The RL Circuit Non-Dimensional Parameters of Interest.

74

and the voltage drop across the total impedance is;

$$V_R(t) = RI = V_c(1 - e^{-Rt/L}) \qquad 6.1.5$$

Note that the voltage does not ring up in any part of the circuit, due to the absence of capacitance in the circuit.

The total power dissipated into the circuit is;

$$P_T(t) = V_c I = (V_c^2/R)(1 - e^{-Rt/L}) \qquad (6.1.6)$$

and thus, the total energy dissipated into the circuit is;

$$E_T(t) = \int_0^t P_T(t')\, dt'$$

$$= \frac{V_c^2 L}{R^2}\left(\frac{Rt}{L} - 1 + e^{-Rt/L}\right) \qquad (6.1.7)$$

The energy accumulated into the total inductance is:

$$E_T(t) = \int_0^t P_T(t')\, dt' = \int_0^t IL\,\frac{dI}{dt'}\, dt'$$

$$= \frac{V_c^2 L}{R^2}\left[-1 + e^{-Rt/L}\left(2 - e^{-Rt/L}\right)\right] \qquad (6.1.8)$$

The fraction of the total energy which is accumulated into the total inductance is thus;

$$\frac{E_L(t)}{E_T(t)} = \frac{1}{2}\left[\frac{-1 + e^{-Rt/L}\left(2 - e^{-Rt/L}\right)}{Rt/L - 1 + e^{-Rt/L}}\right] \qquad (6.1.9)$$

Note that;

$$\frac{E_L(t)}{E_T(t)} \Rightarrow 1 \quad : \quad Rt/L \ll 1$$

$$\Rightarrow 0 \quad : \quad Rt/L \ll 1 \qquad (6.1.10)$$

Figure 48 plots the various parameters of interest.

The maximum energy which can be stored in the total inductance is $1/2 \times V_c^2 L/R$, but at this energy the efficiency is unacceptable. For very short

73
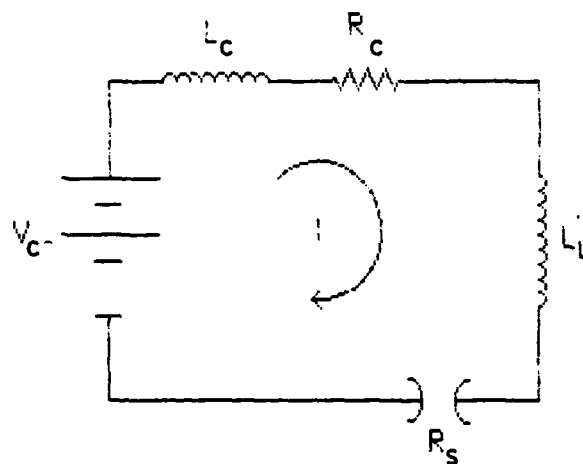
V_c is the charge voltage (assumed = const.),

L_c is the charge inductance,

R_c is the charge impedance,

L_L is the load inductance, and

R_s is the opening switch impedance in closed operation (assumed = const.).

Figure 47   Illustration of the Inductive Store Series RL Circuit.

VI. THEORETICAL ANALYSIS RESULTS

In order to illustrate the importance of the external circuit on switch performance, scaling rules have been developed for two circuit types. The first is a series RL inductive circuit with a constant voltage supply. The second is a resonant charging – RLC circuit. These are addressed in sections 6.1, 6.2, and 6.3. Some photoionization seedant density considerations are covered in section 6.4. Section 6.5 and 6.6 then investigate field distortion effects and EMN considerations in these discharges.

1. SCALING GUIDELINES FOR AN INDUCTIVE STORAGE RL CIRCUIT

Figure 47 illustrates the RL circuit of interest. At some time the switch is closed and energy is stored in the load inductance. At a later time the switch is opened and the energy stored in the inductor is then transferred to another circuit via a closing switch. It is the amount of energy stored in the load, the efficiency with which it is stored and the time required to store it which are of interest.

Referring to Figure 47, let $R = R_c + R_s$ and $L = L_c + L_L$. If the switch closes instantly at time $t = 0$, then the following 1st order O.D.E. and initial conditions hold;

$$V_c = RI + L\, dI/dt \qquad\qquad (6.1.1)$$

and

$$I\,(t = 0) = 0 \qquad\qquad (6.1.2.)$$

The solution for I is;

$$I(t) = V_c/R\,(1 - e^{-Rt/L}) \qquad\qquad (6.1.3)$$

The voltage drop across the total inductance is;

$$V_L(t) = L\, dI/dt = V_c\, e^{-Rt/L} \qquad\qquad (6.1.4)$$

71

of the space charge will be pulled through into the discharge region, and the e-field will be increased.

4) Screen Anode; High Voltage--There is no more space charge than with low voltage and there is no conceptual change.

Conclusion: Assuming that there are more electrons emitted from the copper screen than from the solid stainless steel electrode, as more of the space charge is pulled from behind the screen, the screen cathode will lead to higher current densities at higher voltages than the screen anode.

a. Conclusions-- These space charge effects give the discharge a partial e-beam appearance, yielding enhanced conductivities and improved flashboard efficiencies since the UV not absorbed by the gas is available for secondary electron emission from the solid electrode and the UV blocked by the screen electrode also produces secondary electrons. This leads to some interesting design considerations. If the screen electrode is run as the anode with as high a transmissivity as is reasonable, and the solid electrode is made of a material with a very high secondary electron coefficient, then the optimum design may not be one where the majority of the UV flux is used for photoionization of the gas. If, on the other hand, the screen electrode is operated as the cathode it will be possible to design a high transmissivity screen with sufficient surface area to remove the cathode fall voltage and yet allow very efficient photoionization of the gas.
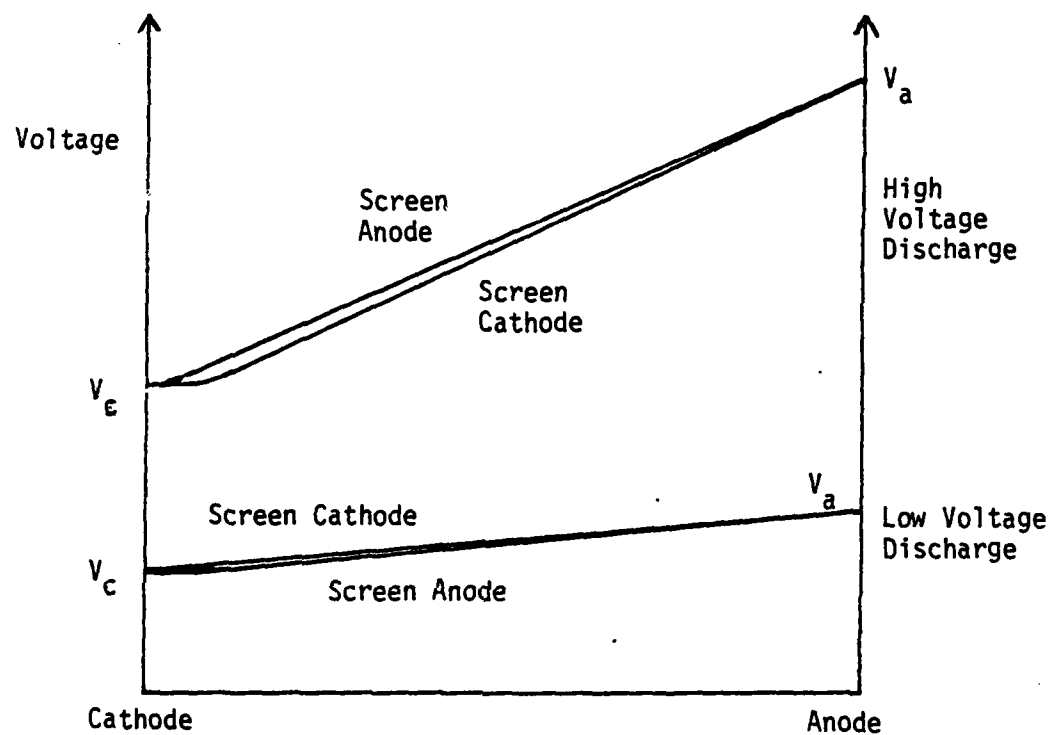
Figure 46 A Schematic Illustration of the Four Discharge Types
Under Consideration.

subscript ss refers to the solid stainless steel electrode, A is the area of electrode per unit area, F is the flux of photocathodic UV and   is the emissivity of the material. With;

$$A_{Cu} = 0.\overset{\circ}{3}5, \quad A_{ss} = 1.0$$

and

$$\frac{F_{Cu}}{F_{ss}} = \frac{1}{(0.79 \times 0.65)}$$

$$= 1.9$$

derive that;

$$\left.\frac{dn_e}{dt}\right|_{Cu} / \left.\frac{dn_e}{dt}\right|_{ss} = 0.68 \frac{\epsilon_{Cu}}{\epsilon_{ss}}$$

If, as expected;

$$\epsilon_{Cu} > 1.5 \; \epsilon_{ss}$$

then the photocathodic yield from the upper screen electrode will be greater than from the solid stainless steel electrode.

It is next assumed that whichever electrode is operated as the discharge anode, the electrons emitted from it will be rapidly conducted back to its surface, and that space charge effects over the anode will be very small, and thus neglected. There are four discharge types which will be examined now, screen cathode with low and high discharge voltage, and screen anode with low and high voltage. They are illustrated in Figure 46.

1) Screen Cathode Low Voltage--With low discharge voltage little of the space charge emitted from the back of the screen will be pulled through into the discharge region, and the e-field will be relatively uniform, as illustrated in the next figure.

2) Screen Anode; Low Voltage--The solid electorde is now the cathode, and none of the space charge is now masked from the discharge. This leads to an increased electric field in the rest of the discharge, as illustrated in the figure.

Conclusion: For low discharge voltage, and for the same volumetric ionization rates, the e-field, and thus the current density with the screen anode will be greater than with the screen cathode.

3) Screen Cathode; High Voltage--As the discharge voltage increases more
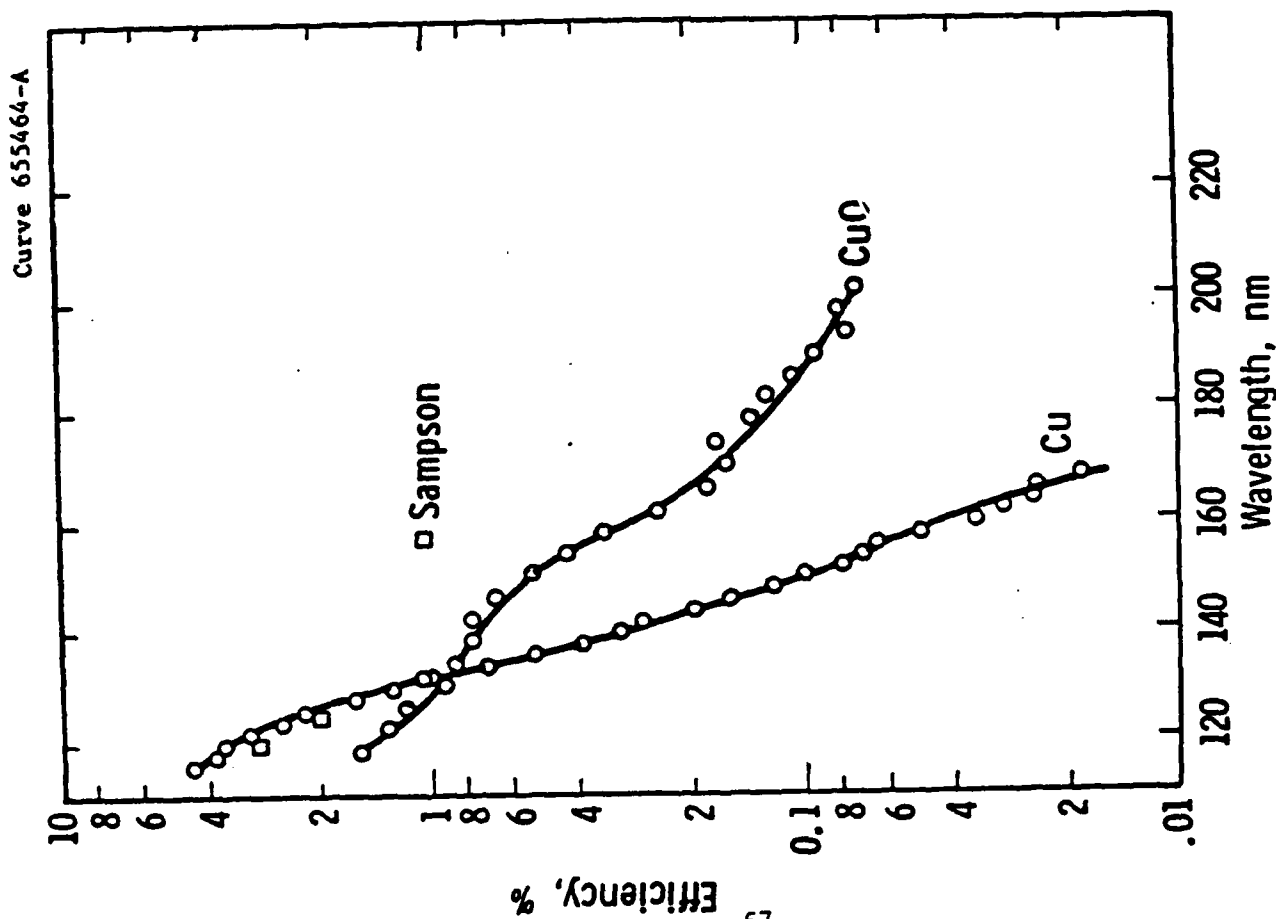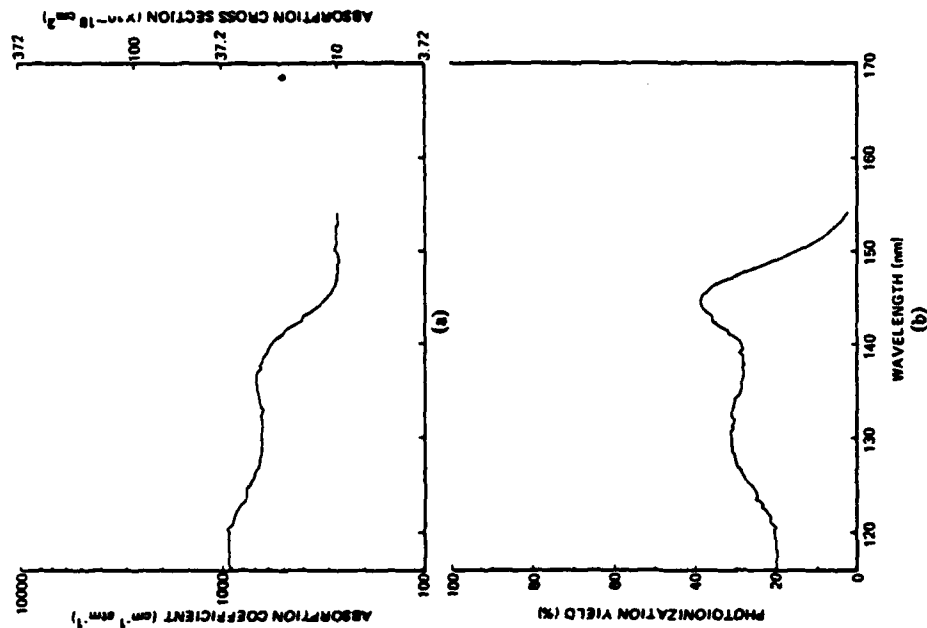
68

Figure 45 Trimethylamine.

(a) Photoabsorption cross sections.
(b) Photoionization yields

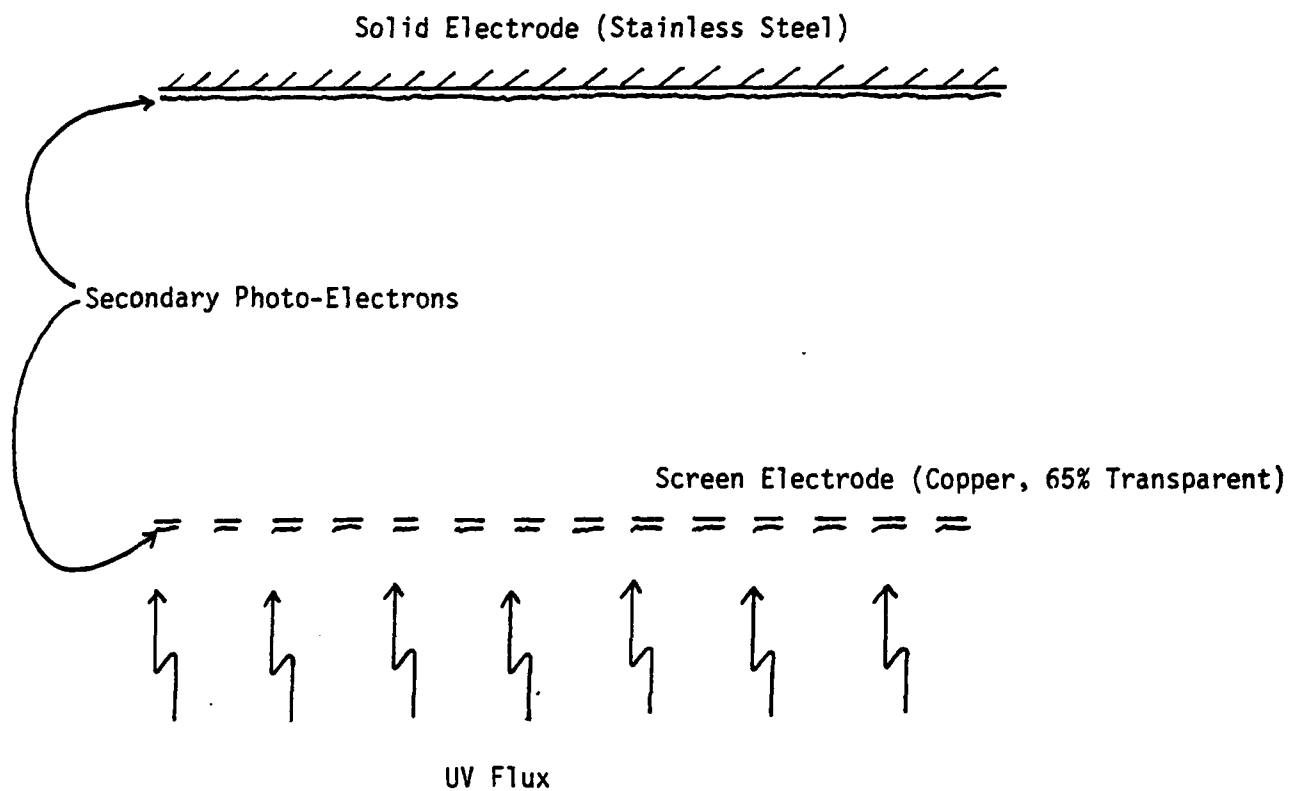

Figure 44 Photocathodic yield of Cu and CuO

67

Figure 43 A Schematic Illustration of the Situation Under Consideration.

decay data points being fit. A faster machine with greater memory and a compiled language should easily give an order of magnitude improvement in performance, and make the use of the three parameter curve fit realistic. Results for every gas mix will then be obtainable.

5. ELECTRODE PHOTOELECTRON EMISSION

In this section an explanation of the observations made in section 5.2 in relation to the lack of a cathode fall voltage drop with any of the N_2 based mixes and the polarity dependence of the current density at low discharge voltage is suggested.

The lack of a cathode fall voltage drop is easily explained. The secondary electron photoemission flux from the electrode surfaces is relatively stronger than the volumetric photoionization rates in the discharge itself. This phenomenon is not that unusual in itself. What is more interesting is the polarity dependence of the current density which is analyzed next.

Figure 43 shows a schematic illustration of the situation under consideration. The photo electrons are emitted on the back side of the screen electrode. The photo electrons emitted from the solid electrode "see" the full discharge electric field, while those emitted from the screen electrode are in a low field region, masked from the discharge by the screen

Figures 44 and 45 show that the photocathodic yield of both Cu and CuO are largest at wavelengths less than about 120 nm, and that the absorption coefficient of TMA at these wavelengths is about 900/cm atm. With 325 ppm TMA and 400 torr total pressure, about 79% of the 120 nm flux passing through the screen electrode reaches the solid electrode. Assuming that the photocathodic yield for stainless steel is also stronger at the lower wavelengths, then the electron photoemission fluxes from the two electrodes are given by;

$$\frac{dn_e}{dt}\bigg|_{Cu} = A_{Cu} \times F_{Cu} \times \epsilon_{Cu}$$

$$\frac{dn_e}{dt}\bigg|_{ss} = A_{ss} \times F_{ss} \times \epsilon_{ss}$$

where the subscript cu refers to the copper screen electrode, the

65

$$. \quad E_L = \frac{1}{2} LI_{max}^2$$

$$E_C = \frac{1}{2} LI_{max}^2 \, (1+r) = \frac{1}{2} CV_o^2$$

3. CIRCUIT EXAMPLES

First we consider the resonant charging circuit.

We want 10 times more energy stored in the inductor than dissipated in the switch. Switch impedance is 0.05 Ω. We want 20 kJ in the inductor. What are C, V_o, t_f, and L if I_{max} = 20 KA?

Solution:

Given:

$r = 0.1$

$R_s = 0.05 \; \Omega$

$I_{max} = 20 \; KA$

$E_L = 20,000 \; J$

Derive:

$E_L = \frac{1}{2} LI_{max}^2$	whence	$L = 100 \; \mu H$
$E_C = \frac{1}{2} LI_{max}^2 (1+r)$	whence	$CV_o^2 = 4.4 \times 10^3 \; J$
$r = \pi R_s \sqrt{C/L} = 0.1$	whence	$C = 40.5 \; \mu F$
	and	$V_o^2 = 1.09 \times 10^9 \; V^2$

To yield;

$C = 40.5 \; \mu F$

$V_o = 32.9 \; KV$

$t_f = 200 \; \mu s$

$L = 100 \; \mu H$

Now consider the RL circuit of section 6.1. If we want the same energy stored in the inductor and the same energy ratio of 10, then;

$$\frac{E_L}{E_T} = \frac{10}{11}$$

which, from equation 6.1.9 yields;

$$Rt/L = 0.145$$

If the charge voltage is the same as in the preceding example, 32.9 KV, then equation 6.1.8 yields, for $R_S = 0.05\Omega$;

$$L = 5.1\mu H$$

and thus the switch closed time is;

$$t_L = 14.7\mu S$$

Note that in this case the maximum current is 660 KA compared with 20 KA for the resonant charging circuit. The resonant charging circuit, however, requires a run time of 200 μs whereas the RL circuit requires only 15 μs. The long run time for the RLC circuit imposes fairly mild constraints on the switch closing and opening times, whereas the RL circuit would require switch times of about 1 μs.

This example illustrates the importance of external circuit considerations upon switch requirements and some of the trade offs which will have to be made.

One final comment is that both the preceding analyses assumed constant switch impedance. Most real switches will, of course, have variable impedance and will require numerical modeling. This does not effect the various observations, however, and the general scaling guidelines will still hold.

4. SEEDANT DENSITY SCALING CONSIDERATIONS

For given discharge dimensions and a given discharge power, and using the form of the photoelectron source strength obtained at Westinghouse (Ref. 3) the total source strength per unit area between the electrodes is of the form;

$$\int_{x_1}^{x_2} S \, dx = \text{const} \int_{x_1}^{x_2} \rho \, e^{-(\alpha+\beta\rho x)} \, dx$$

$$= \text{const} \times \frac{1}{\beta}\left(e^{-(\alpha+\beta\rho x_1)} - e^{-(\alpha+\beta\rho x_2)}\right) \qquad 6.4.1$$

where X and β gas mix dependent constrants, Rho is the seedant density, x, is the distance from the flashboard to the screen electrode and x_2 is the distance

80

from the flashboard to the solid electrode. Looking for the value of Rho which gives the maximum to this function yields;

$$\rho_{opt} = \log(x_2/x_1)/(\beta(x_2-x_1))$$ 6.4.2

If this approach were used in section 5.2, then the optimum TMA density would be 340 ppm, rather than the 324 ppm used. In the configuration used for the experiments, therefore, with a 1 1/2 cm gap and with the flashboard 1 1/2 inches behind the screen electorde, there is no significant discrepancy. For larger discharge gaps, and with the flashboard closer to the screen, however, equation 6.4.2 should be used to derive the optimum photoionization seedant density.

5. FIELD DISTORTION CONTROL OF GLOW DISCHARGES

This section presents results of a study on the theoretical behavior of nonuniform glow discharges where two types of production processes are important in two different regions of the discharge. In one region, a UV- or e-beam sustainer with short penetration distance and high electron production is used to distort the electric fields and generate a second region where self-sustained discharge processes dominate. Before initiation of the discharge, the electric field is below the self-sustained value; after initiation, electron production in the externally sustained region increases the electric field elsewhere to cause the self-sustained mode to operate.. The purpose of this line of research is to develop a glow discharge opening switch that minimizes the power requirements in the sustainer. Our theoretical approach is to use a current conservation electric field model with a glow discharge kinetics model, including electron diffusion.

a. Introduction-- For the past several years, the authors have been interested in and experimented with glow discharges, generally associated with electric discharge lasers. More recently, that interest has shifted to glow discharge opening switches, particularly those that are UV sustained. Research in this area has included actively searching for ways to substantially improve the efficiency of UV-sustained glow discharge switches and, in particular, to reduce the friction of power in the sustainer compared to power transmitted through the switch. Concurrently, a set of computer codes for modeling electric fields and glow discharge inside pulsed power devices, such as electric lasers and glow discharge switches (Ref. 10) are being developed for the Air Force Weapons Laboratory. Results of these studies indicate that the electric field distributions inside externally sustained discharges can be substantially distorted by the imposition of nonuniform conductivity ( ) within the discharge.

b. Solutions of Current Conservation Equations-- In the work reported in this paper, one-dimensional solutions to the current conservation equation,

$$\nabla \cdot \sigma \nabla \phi = 0$$

(6.5.1)

82

where ø is the electric field potential, have been studied to evaluate the possibility of control of glow discharges by intentional distortion of the electric fields. In this equation, the conductivity is modeled from a discharge kinetics code as a function of time and space, and the resulting nonlinear partial differential equations are solved to yield the distribution of conductivity, current, and electric field as a function of time and space.

If uniform photoelectron production is assumed, the electric fields are uniform and simple, average-field analysis of the discharge is adequate. However, it was determined that better use of the UV photons required stronger absorption characteristics in the gas and this violated the uniformity assumption. For this one-dimensional analysis, the anode-cathode gap can be pictured as divided into several layers and distributions are calculated for each layer. The current conservation equation requires that the current be the same in each layer. Thus, if the electron number density is higher in one layer, the electric field adjusts so that the other gas parameters, mainly drift velocity, are reduced until the currents are the same in each layer.

The discharge configuration modeled is that shown in Figure 51. It is a conventional axisymmetric glow discharge with a UV sustainer (sparker board), a 0.1 Ω ballast resistor, and an essentially infinite capacitor. (The ballast is used for controlling the self-sustained discharges and is retained in all calculations for consistency.) The baseline point for the parameter variation (shown as the large dot on the graphs) has already been through a preliminary optimization with this gas and so shows good performance in the comparisons. The discharge area is 570 cm^2, the electrode separation is 2 cm, and the capacitor voltage is nominally 20 kV. The gas mixture used for these calculations was a 3:2:1 He/N$_2$/CO$_2$ mix that was chosen because the discharge kinetics are well known, and for convenience, because it was already loaded into the glow discharge kinetics code as the result of previous laser calculations. The discharge parameters were taken from Lowke, Phelps, and Irwin (ref. 11) and Douglas-Hamilton (ref. 12). The gas mix itself has not yet received any optimization regarding its use in a switch, but was chosen arbitrarily.

During the course of the computer analysis, it was found that when the UV source is sufficiencly strong and the seedant density (and, therefore, absorption coefficient) is sufficiently large, the discharge appears to form into two regions: one UV-sustained and one self-sustained. Figure 52 shows the distribution of normalized electric field, E/N, (where E is the electric field in V/cm and N is the neutral number density in particles/cm^3) as a function of distance along the anode-cathode gap. The calculations are for an absorption
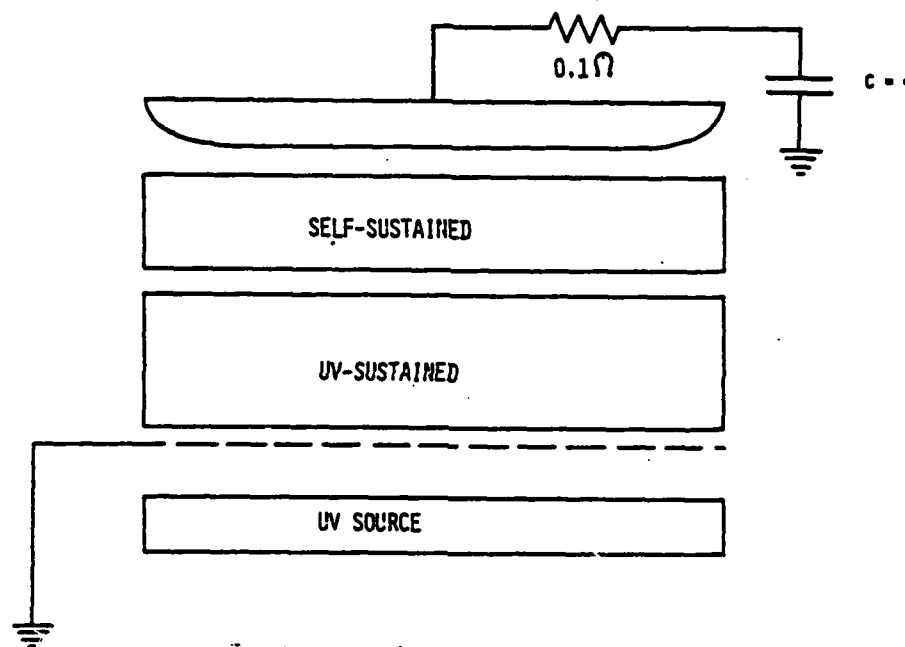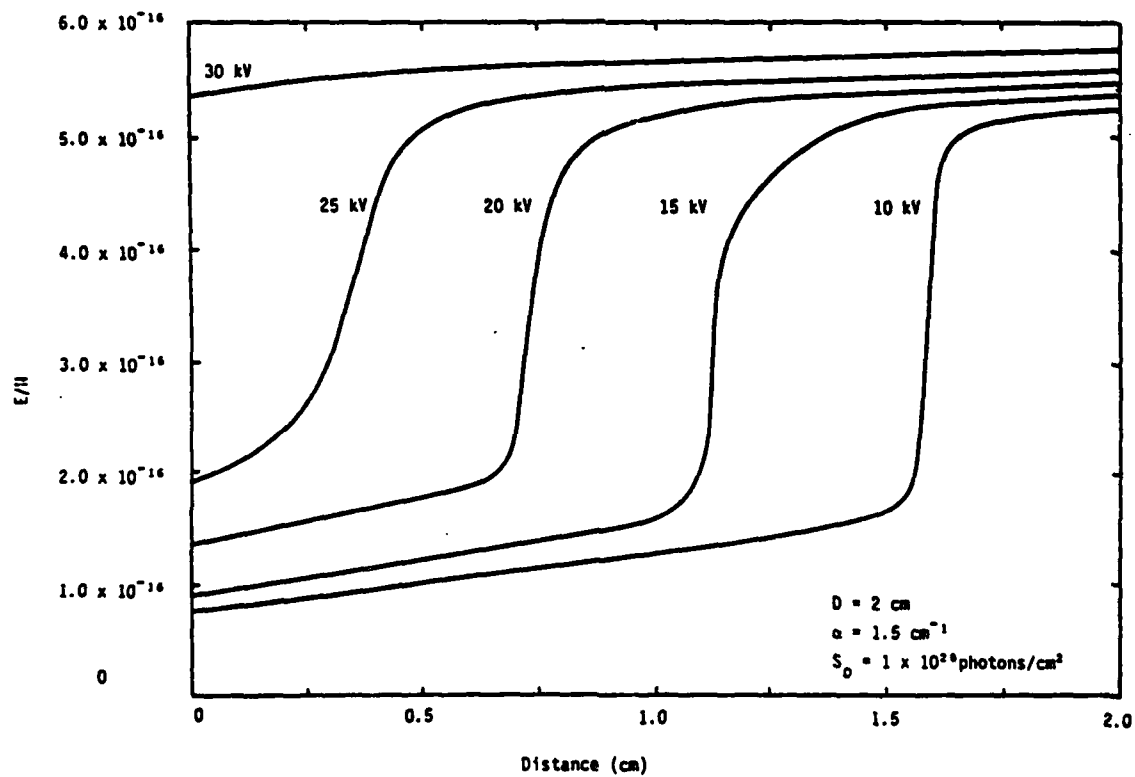
83

Figure 51 Glow Discharge Chamber

Figure 52 E/N vs Distance

coefficient of 1.5 cm and a source flux of 1×10^{20} photons/cm²/sec. At 30 kV applied potential, the entire discharge is self-sustained and there is very little distortion of the electric field, the slight amount present being caused by the increase in electron number density directly in front of the UV source (located at 0 cm). As the imposed electric field is reduced, the discharge shifts into two distinct regions of operation. The region nearest the spark source operates in the UV-sustained mode with low voltage drop and low E/N. The region at the opposite electrode operates in the self-sustained mode with a high voltage drop determined by the glow voltage.

The discharge is operating in the following manner. The self-sustained glow discharge, together with its external circuit, has a particular operating voltage, called the glow voltage, which is a weak function of the current density. The UV-sustained region produces a strong gradient in conductivity due to the high absorption of the seedant. The current conservation equation, in an alternate form,

$$\frac{\nabla \cdot \bar{E}}{\bar{E}} = - \frac{\nabla \sigma}{\sigma}$$

(6.5.2)

shows that the electric field must shift to accomodate the gradient in conductivity across the gap. The electric field rises until a portion of the discharge becomes self-sustained at the glow voltage. A very slight additional rise in electric field produces a substantial rise in current, so the electric field is effectively "clamped" at the glow voltage. This produces the two-region discharge shown in Figure 52. The discharge behaves as a resistively ballasted, self-sustained discharge with the UV-sustained portion providing the current control by acting as the resistive ballast. As the overall applied voltage on the switch is decreased, the point at which the switch operates in the self-sustained mode moves further away from the UV source. The glow voltage decreases slightly caused by a decrease in the current density in the UV-sustained region.

Figure 53 shows the discharge current density as a function of applied voltage for the same parameter values as before. The baseline operating point at 20 kV is identified. The current in the device is limited by the current in the UV-sustained region. As the applied voltage is increased, so is the E/N in the UV-sustained region (Figure 52). This increases the drift velocity, as well as the attachment and ionization coefficients (for this gas mix) in the UV-sustained region, and increases the current quite substantially for E/N_s

that approach self-sustained values. The electric field in the self-sustained region is increased slightly so that the current density there will match the

increased current density in the UV-sustained region. Control of the switch, operating with an overall E/N below the self-sustained value, can thus be obtained by controlling the UV-sustained region, which can be a much smaller volume than the total switch volume.

Figure 54 shows the current density versus absorption coefficient for three different imposed voltages. As the absorption coefficient increases for a given voltage, the current density also increases, since more conductors (electrons) are being generated in the UV-sustained region. A peak is reached when the UV-sustained region becomes too small in physical extent because of the short absorption distance. At this point, the electric field in the UV-sustained region diminishes faster than the increase in conduction electrons. The result is a decrease in current density for this region which controls the overall switch current. In the limit of infinite absorption, the electric field is too low in the UV region and the region too narrow to allow the self-sustained region to operate. In effect, too much absorption produces the same effect as no source at all: the self-sustained electric field is effectively the same as the average field which is too small for self-sustained operation. For each value of applied voltage, there is an optimum absorption coefficient that provides maximum current density for a given source strength. That peak in absorption coefficient moves to higher values as the applied voltage increases, since more of the switch falls into the self-sustained region and sufficient electric field is available to maintain high current in the UV region even in the presence of reduced UV region size. Also, the peak in the current density tends to be sharper at higher voltages because the UV-sustained region is operating in a smaller physical region where a small change in absolute distance can be a large percentage change.

Finally, the current density as a function of source strength is shown in Figure 55. At a fixed voltage, as the source strength is increased, the overall number of photoelectrons in the discharge increases. This tends to lengthen the UV-sustained region and makes the transition between the two regions less steep than in Figure 52. This increase in conductivity lowers the electric field in the UV-sustained region and slightly increases it in the self-sustained region. As the source term becomes very strong, there is reduced voltage in the UV-sustained region, but high conductivity and very large currents can be conducted. Figure 56 gives an alternate look at the same situation; here, Figure 55 data is plotted on a log-log scale, and the simple square root dependence (plotted about the baseline point), shown by the dashed line, is the curve that would result from a recombination-dominated, externally sustained uniform discharge where

$$n_e \propto \frac{S}{\gamma}$$

(6.5.3.)

$S_0 = 1 \times 10^{20}$ photons/cm²
D = 2 cm
$\alpha = 1.5$ cm^{-1}

CURRENT DENSITY (A/cm²)
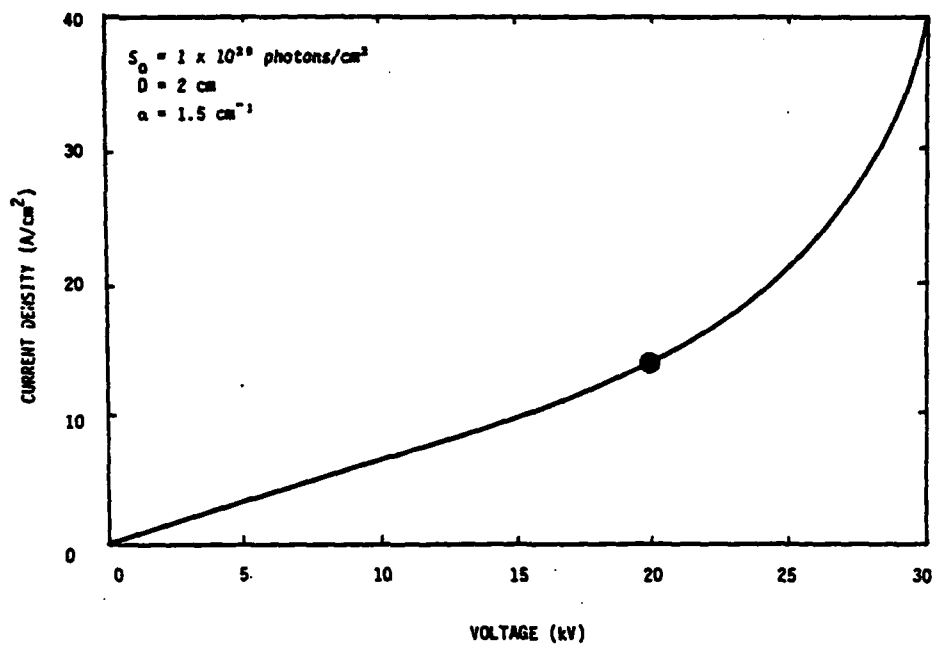
VOLTAGE (kV)

Figure 53 Voltage vs Current Density

V = 20 kV
$S_0 = 1 \times 10^{20}$ photons/cm²
D = 2 cm

25 kV

20 kV

15 kV

CURRENT DENSITY (A/cm²)

ABSORPTION COEFFICIENT (cm^{-1})
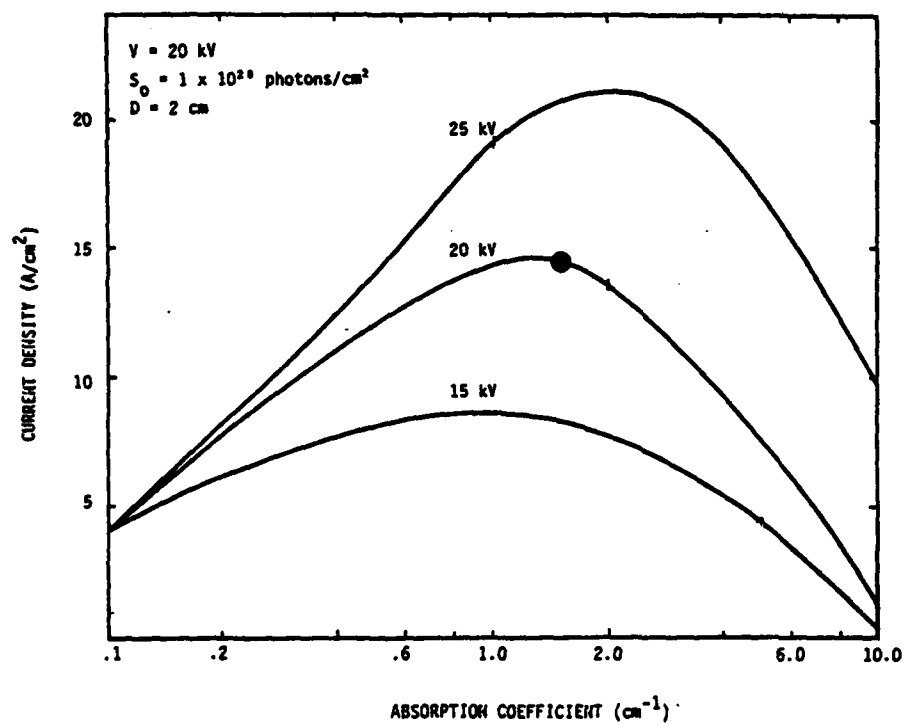
Figure 54 Absorption Coefficient vs Current Density
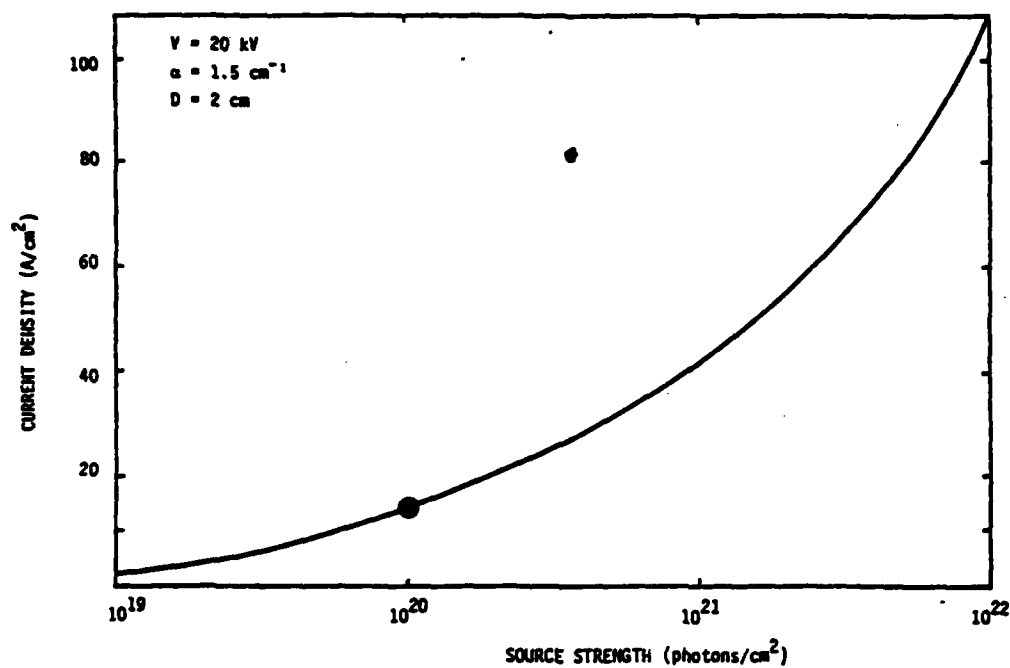
87

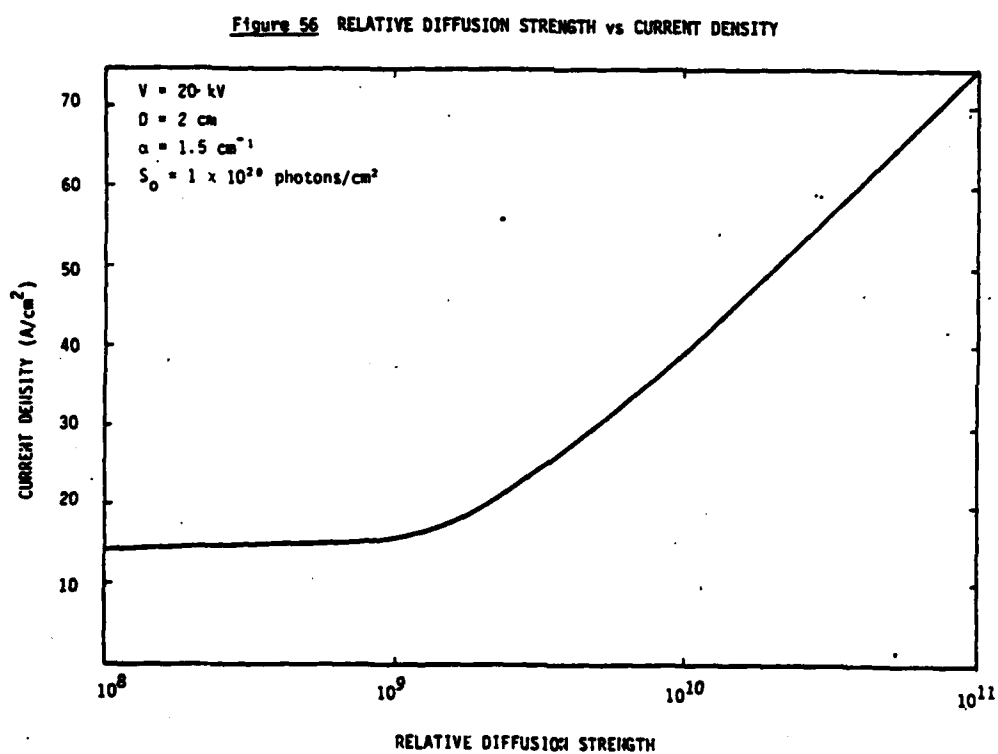Figure 55 Source Strength vs Current Density

Figure 56 RELATIVE DIFFUSION STRENGTH vs CURRENT DENSITY

where S = source strength

       X = recombination coefficient

The UV-sustained region of the discharge is attachment dominated below $S = 1 \times 10^{20}$ photons/cm^2/sec, and becomes recombination dominated near this value and above. The fall off from the straight line is due to the external 0.1 Ω ballast resistor.

c. **Conclusions**-- The results of these calculations provide a fascinating insight into the operation of glow discharges. If the mechanisms discussed in this paper prove to be correct, then field distortion methods may provide an excellent way to control glow discharges with low power consumption UV-sustainers or electric beam sustainers. The next step is to experimentally study this discharge concept using these results as a guide. Two-dimensional electric field calculations are also required to determine if the two-dimensional effects are important in controlling the glow discharge in this fashion.

6. ELECTROMAGNETIC NOISE ANALYSIS

The purpose of this section is to derive a model to estimate the electromagnetic noise (EMN) created by glow and spark discharges. The purpose of the model is to evaluate EMN production in the vicinity of operating UV-sustained glow discharge switches.

The current in discharge switches typically rises to many kiloAmperes in very short times, and then remains relatively constant until it is turned off about as suddenly as it came on. The damaging interference is caused by the fast rising leading edge, whose rise rate may typically be on the order of 10^{11} Amp/sec. The rising current will produce a rising magnetic field, which induces strong currents in equipment in the vicinity.

The model derived below assumes that the discharge and the circuitry causing it can be modeled as a small current loop, with a radius of about ten centimeters (0.1m). With appropriate shielding of peripherals such as the power supply and connecting cables, the effective size of the current loop should not significantly exceed that. We shall use a nominal 0.1m radius loop for illustrative purposes. The near-field (<wavelength) dominates in this situation. The magnetic field from such a loop will be maximum along the loop axis. In mks units (Ref. 13);

$$dB/dt \,/\mu_o \;=\; dI/dt \cdot a^2 /2(x^2 + a^2)^{3/2} \qquad (6.6.1)$$

where B is the induced magnetic field, $\mu_o = 4\pi \times 10^{-7}$ Henry/m, I is the current, a is the loop radius, and x is the distance from the loop center to the target. Using a distance x = 1m and the above illustrative values:

$$dB/dt \approx 4\pi \cdot 10^{-7+12-2}/2 \,(1.01)^{3/2} \approx 6000 \text{ Webber/m}^2/\text{sec} \qquad (6.6.2)$$

The effect of such a fast-rising magnetic field will depend on the size of the target. By Maxwell's second equation:

$$x E = - dB/dt \quad \text{or} \quad E\,dl = dB/dt\,ds \qquad (6.6.3)$$
$$\text{loop} \qquad \text{surf}$$

Let us assume that the target has an effective surface of a 1 cm square

(10^{-4}m^2). This is reasonable for a well-shielded piece of sensitive electronic

90

equipment. For a small target, we can assume the field is constant, so:

$$E \approx dB/dt \cdot 10^{-4}m^2 /00.4m \approx 15 \text{ Volts} \qquad (6.6.4.)$$

The interesting thing is to see what variables this answer is sensitive to. The size of the target affects the answer in two ways: the threat increases in proportion to the effective cross-sectional area, but decreases in proportion to the effective circumference. Therefore, long shielded cables are less likely to be a problem than roughly square boxes with a small discontinuity in the shield. The threat is proportional to the discharge current rise rate, rather than the maximum current, and to the loop area. Most important, the threat decreases with distance approximately as X^{-3}. This is the most significant variation.

If we re-define the distance to the target as measured from the loop edge, rather than the center, $r = \sqrt{a^2 + x^2}$, then $B = 2\mu_0 \cdot ia^2/r^3$. Defining the target size s as the ratio of its effective cross-sectional area to circumference, we can define an effective threat

$$\mathcal{E} = E/s \approx dB/dt = 2\mu_0 \cdot ia^2/r^3 \text{ (V/m)} \qquad (6.6.5.)$$

Since $\mu_0 = 4\pi \cdot 10^{-7}$ H/m, and the area of the loop is πa^2, it is convenient to define the current rate times the loop area as a source term:

$$\mathcal{S} = \pi a^2 i \qquad (6.6.6)$$

such that $\mathcal{E} = 8 \cdot 10^{-7} \cdot \mathcal{S}/r^3$, or $r^3 = 8 . 10^{-7} . \mathcal{S}/\mathcal{E}.$

Fig. 57 displays the relationship of $\mathcal{E}$ vs r. The units are Volts per meter of target size, normalized to a source $\mathcal{S} = 1m^2$.GAMP/sec, corresponding to a 10^{11} Amp/sec current rise rate in a $0.1m^2$ loop.

The next question is how this varies with angle from the axis. Jackson derives a completely general solution, which involves two elliptic integrals. However, at distances far compared to the size of the loop, the solution tends toward the following approximately (Ref. 14);

$$Br = 2\cos\theta \cdot \mu_0 ia^2/r^3 \text{ and } B\theta = \sin\theta \cdot \mu_0 ia^2/r^3 \qquad (6.6.7)$$

Notice this reaches a maximum on the loop axis, and a minimum in the loop plane of half the maximum. Both minimum and maximum are shown in Fig. 57. The complete pattern can be constructed from the more general solution for r for arbitrary angle:
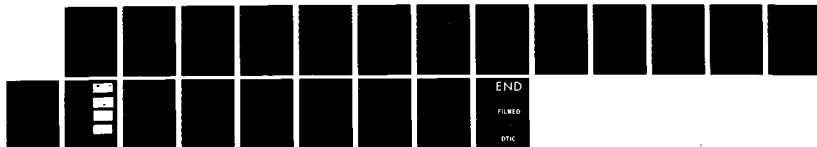
91

Fig.57. DISCHARGE CLOSE-FIELD
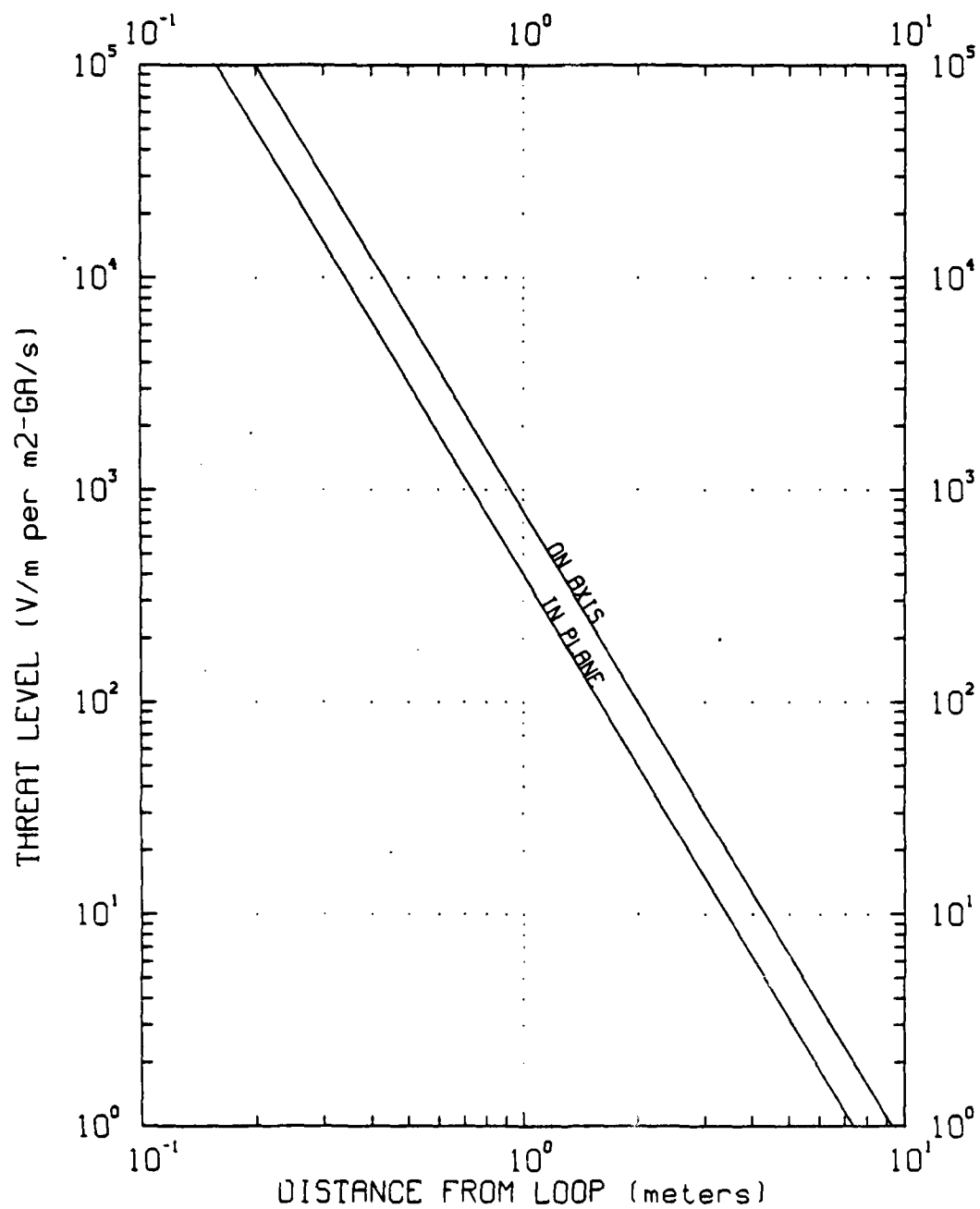
END

FILMED

DTIC

MICROCOPY RESOLUTION TEST CHART

NATIONAL BUREAU OF STANDARDS-1963-A

(6.6.8)

The resulting pattern is displayed in Fig 58. The important thing is that the threat does not go to zero; it is only reduced by a factor of 2 in the plane of the loop. This is a near-field; not a progagating wave. Thus Fig. 58 is not an antenna pattern, which would have a null somewhere.

Notice that the threat is very low (1V/m) at about 10m away. The near-field model is applicable to distances less than one wavelength. A 10m wavelength corresponds to a cycle time of 10 nsec. Therefore, for a threshold of interest of 1 V/m, the above model applies to discharges with rise times > 1 nS, or for targets susceptible only to frequencies <3GHz.

It is interesting to compare the EMN threat to that of a nuclear electro-magnetic pulse (EMP). Ref. 15 derives an approximate nuclear EMP model based on the saturation phenemenon which results from the high-frequency approximation. What happens is that the E-field saturates at a value equal to the ratio of the transverse current to the conductivity. Since both the current and the ionization it causes are proportional to gamma flux, the saturation E-field is insensitive to burst yield or height. At typical desaturation altitudes, the ratio is tens of kiloVolts/meter. Notice that the discharge threat is not comparable to nuclear EMP until r is comparable to a. In other words, the target would have to be virtually inside the discharge machinery.

What we have, then, is a threat which 1) falls off with distance as $1/r^3$, 2) is proportional to current rate times the effective loop area, but 3) does not vary significantly with orientation (a factor of two from maximum to minimum). The susceptibility of a given target to the threat is proportional to its "size", defined as the ratio of its effective cross-sectional area to details of the actual source current loop shape and target geometry not to be very significant in determining the extent of the threatened area. That extent can be estimated from Fig. 57 or 58 for a calculated or experimentally measured source term (m^2·GAmp/sec), and an estimated threat threshold (V/m) level of interest for a given target piece of equipment or class of targets.

93

Fig. 58. CLOSE-FIELD PATTERN
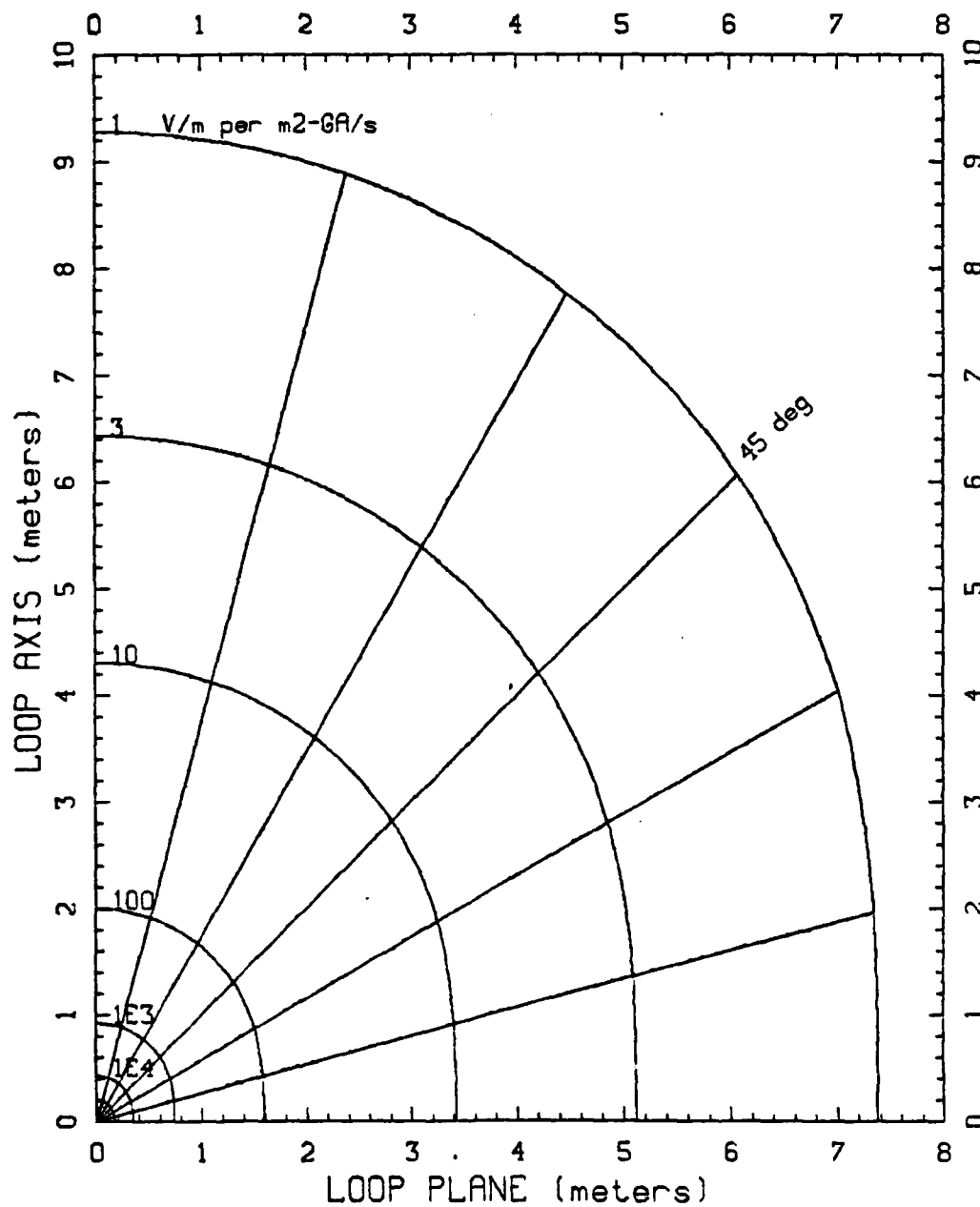
APPENDIX A .

A SUGGESTED THREE PARAMETER CURVEFITTING PROCEDURE

If the relative photoionization UV flux follows the photodetector trace then it is possible to derive the discharge parameters of interest from the current and photodetector traces. Using the notation of section 4.2

$$\frac{dn_e}{dt} = S - An_e - Rn_e^2 \qquad (A.1)$$

Integrate w.r.t. time to yield

$$n_e - n_{eo} = \int_0^t S \; dt' - A \int_0^t n_e \; dt' - R \int_0^t n_e^2 \; dt' \qquad (A.2)$$

Multiply through by ev_e and derive

$$J - J_0 = ev_e \int_0^t S \; dt' - A \int_0^t J \; dt' - \frac{R}{ev_e} \int_0^t J^2 \; dt' \qquad (A.3)$$

The photodetector trace yields S/S_{max}. Define

$$JR = J/J_{max} , \quad SR = S/S_{max}.$$

Equation A.3 can then be written as

$$JR - JR_0 = \frac{ev_e S_{max}}{J_{max}} \int_0^t SR \; dt'$$

$$- A \int_0^t JR \; dt' - \frac{R}{ev_e} \int_0^t J \; JR \; dt' \qquad (A.4)$$

95

By numerically integrating the current and photodetector data each of the integrals is readily evaluated at each time point. Let times associated with the data points be t_i, and define

$$X_1(i) = \int_0^t SR \, dt$$

$$X_2(i) = \int_0^t JR \, dt$$

$$X_3(i) = \int_0^t J \, JR \, dt$$

and

$$Y(i) = JR(t_i) - JR_0$$

Equation A.4 is then written in the form

$$Y(i) = \frac{e}{J_{max}} v_e S_{max} \, X_1(i) - A \, X_2(i) - \frac{R}{ev_e} X_3(i) \qquad (A.5)$$

Note that equation A.5 is linear in the unknown coefficients and thus a standard (Ref. 5) noniterative, linear least squares curve bit may be used to derive the values for $v_e S_{max}$, A, and R/v_e. This is the suggested three parameter curvefitting procedure.

In order to carry out this procedure it is necessary to store a large amount of data in the computer RAM, and the program itself would be relatively long. Our PC was limited to 64K RAM and was not capable of running this routine.

Our success with the two parameter, iterative program does, however, gives us confidence in the suggested parametric approach. This routine will enable the acquisition of data over a wide range of discharge parameters.

APPENDIX B

FLASHBOARDS: AN OPERATIONAL ANALYSIS

INTRODUCTION

Planar spark arrays, or flashboards, are one of few planar sources of UV light. Flashboards consist of multiple surface discharge spark gaps arranged to breakdown uniformly. Such a device can also be used to provide a planar source of plasma. The multiple arcs generate a plasma sheet which propagates away from the flashboard.

Flashboards have been used for over a decade, but are little understood. The purpose of this work is to provide a basic understanding of flashboards and present some empirical scaling laws to facilitate effective design and operation of flashboards.

FLASHBOARD CONSTRUCTION

The basic elements of a flashboard are shown in Figure B-1. Metalic pads are arranged on a dielectric material having an underlying metalic backplane. The pads are aligned in rows with the gaps between pads in a row providing the spark gaps. Multiple rows are used to provide a wider area of plasma/UV generation. The main concern of the first part of this work is centered around one row of pads. Once an understanding of a single row is achieved, the transition to muiltiple rows is less difficult.

In the experimental effort supporting this work, single rows were constructed on 50 mil. single-sided copper clad circuit board with a G-10 dielectric. The copper was used as a backplane. Pads were constructed on the reverse side using 3/8" lead burglar alarm tape. The pad could be made as wide a needed by laying multiple rows of tape side by side with a little overlap. Once the lead tape was laid, gaps were cut using a sharp knife. This arrangement is shown in Figure B-2. The unusual pad design is needed to insure that the gap configuration is constant if the pad width is modified.

One of the first parameters to be investigated was the capacitance of the pads. What effect does pad capacitance have on the breakdown character-isitcs of a single-row flashboard? To answer this question, breakdown

Dielectric

Initial
Electrode

Pads

Copper
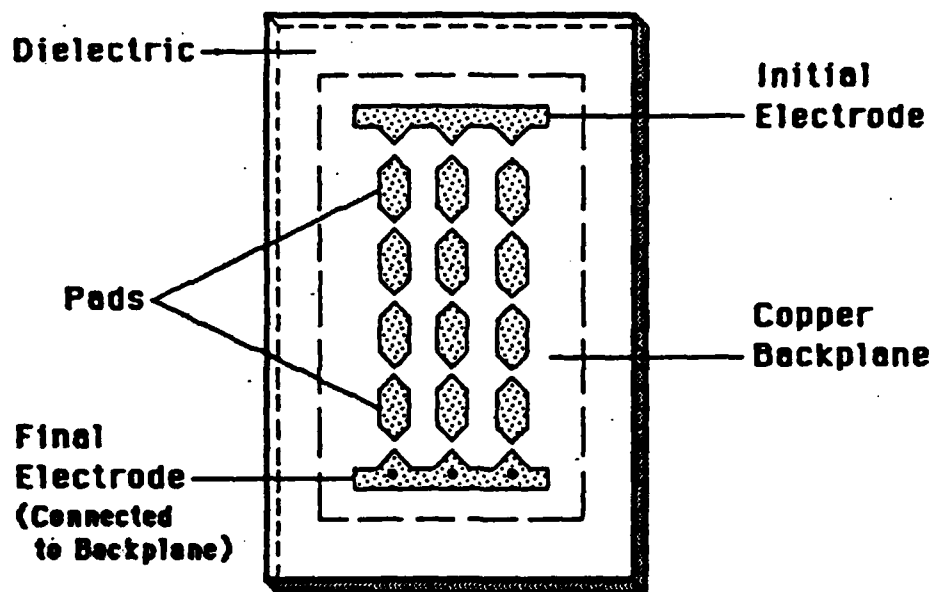Backplane

Final
Electrode
(Connected
to Backplane)

FIGURE B-1
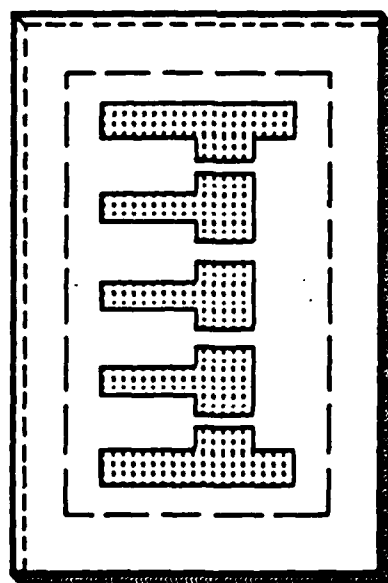BASIC FLASHBOARD LAYOUT

FIGURE B-2
SINGLE-ROW FLASHBOARD LAYOUT

measurements were made on a row of pads as a function of capacitance. The capacitance was changed by adding or removing sections of tape from a pad. The results of this experiment are shown in Figure B-3. The curves represent breakdown voltages for a single row as a function of the number of gaps per row for several values of pad capacitance. For small numbers of gaps, the curves are quite steep. After about 5 gaps, the slope is much less and is not a function of capacitance. The knee in each curve is a strong function of capacitance at least as far as breakdown voltage is concerned. On the other hand the knee is a weak function of pad capacitance in relation to the number of ' gaps. The data in Figure B-3 was taken with a constant gap width of 1.5 mm.

The next question to arise is the one concerned with the role of gap width in single-row characteristics. Figure B-4 shows the results of another experiment in which the pad capacitance was kept fixed, but the gap width was varied. The knees appear to be independent of the gap width in relation to the number of gaps, but are a strong function of gap width in relation to the breakdown voltage. Furthermore, the slope of the curves on the right hand side of the knees are also a function of the gap width.

MODEL FOR SINGLE-ROWS

From the experimental data obtained, a model for the operation of a single-row can be obtained. The model for breakdown can be realized with three stages. Figure B-5 shows these three stages.

Stage I is a set-up stage before breakdown occurs. Each pad floats to a potential somewhere near that of the packplane. In other words, the pads are discharged capacitors. Figure B-5 shows this discharge path to be a resistor which may be leakage current through the dielectric material, ionization of the air, or leakage due to water vapor in the air. Whatever the reason, this allows each pad to be at an equal potential, much different than that of the opposite electrode on the first-gap just prior to breakdown.

Stage II begins when the switch is closed and the first gap breaks down. The first gap breaks down because the first pad is floating at a much different potential than the first electrode. An initial breakdown occurs and current flows until either the next gap breaks down or the first pad (capacitor) is nearly charged; i.e., no current flows. A typical pad/capacitor size is 5 pf. If the average arc impedance in on the order of 1 Ω, then it takes only a few tens of picoseconds for the pad/capacitor to charge. Since the formation time of an arc is on the order of a few nanoseconds, the arc in the first gap extinguishes before the seocnd gap breaks down. Therefore, to break down the
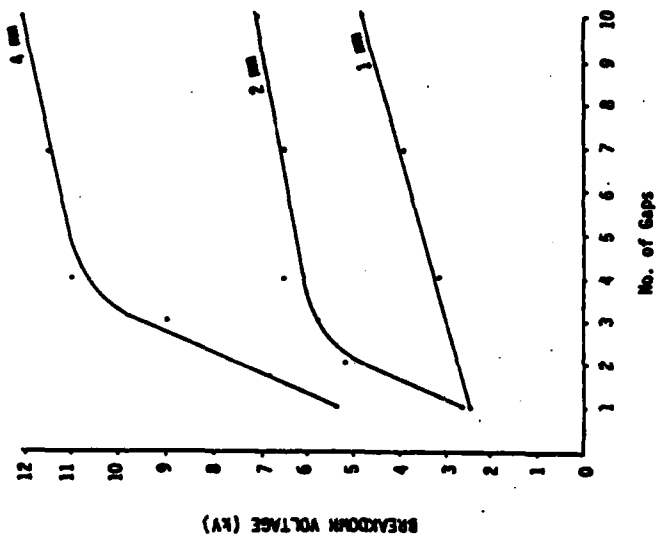
Figure B-4

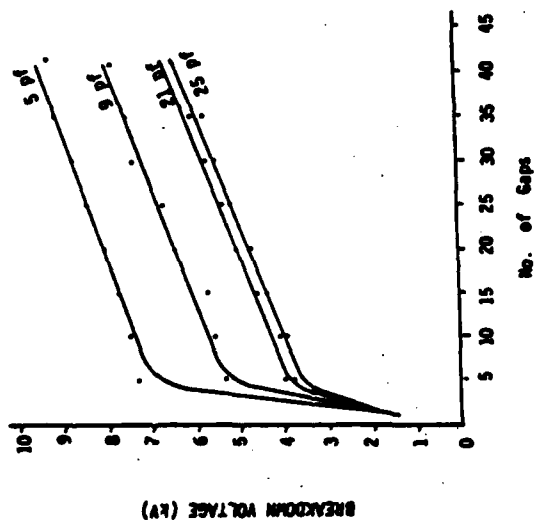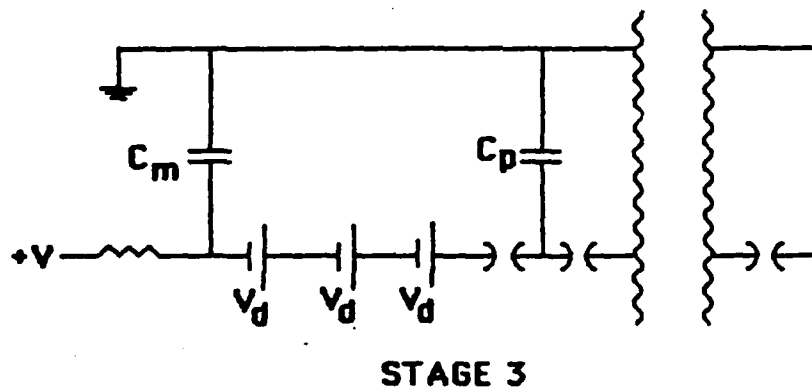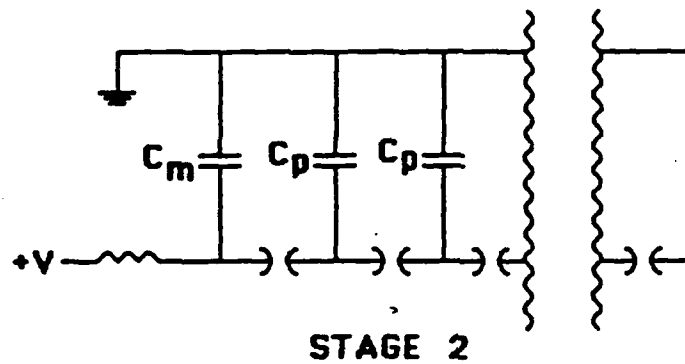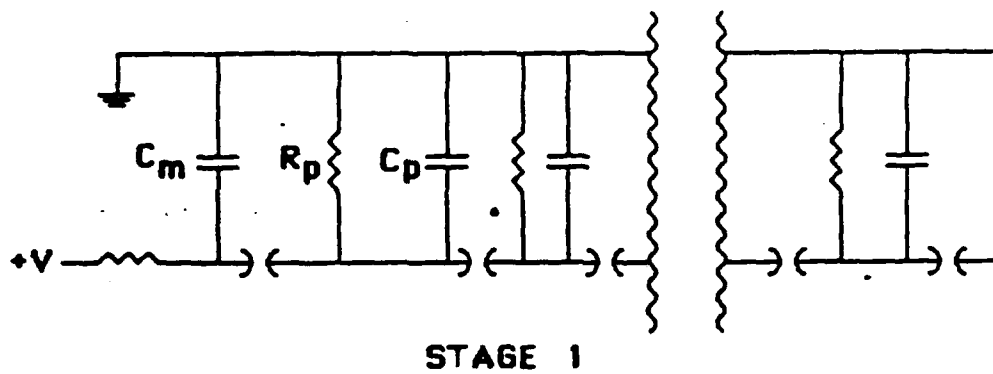BREAKDOWN VOLTAGE VS. GAP WIDTH FOR CONSTANT PAD CAPACITANCE

Figure B-3

BREAKDOWN VOLTAGE VS. PAD CAPACITANCE FOR CONSTANT GAP WIDTH

STAGE 1

STAGE 2

STAGE 3

FIGURE B-5

FLASHBOARD EQUIVALENT CIRCUIT

R_p is the leakage resistance

C_m is the discharge capacitor

C_p is the pad capacitance

101

second gap, the voltage must be high enough to break down the second gap plus restrike the arc in the first gap. The voltage required to to restrike the first gap is not necessarily the same voltage required to initially break down the gap because, even though the arc is extinguished, a conductive path still exists due to the "long" recombination times in the gap. This implies that the curve of breakdown voltage versus number gaps will have a large slope for the first few gaps. In fact, the slope will be large until Stage III begins.

Stage III begins when the arcs in gaps < n have not extinguished before the nth gap breaks down. As the number of gaps increase the impedance in the charging path for the nth pad increases. For large enough 'n,' the RC time constant is large enough to sustain each preceeding arc long enough for the nth gap to break down. For each succeeding gap (mth gap) the breakdown voltage is now just the voltage required to breakdown m-2 gaps plus the voltage drop across the m-1 gap. The equation for the breakdown voltage as a function of the gaps is a straight line given by

$$V_{brkdwn} = n V_d + Const. \qquad (B.1)$$

where n is the number of gaps, V_d is the voltage drop across one arc, and the constant is the voltage required to initiate Stage III. Once Stage III is entered, the gaps continue to breakdown and are sustained until the last gap has broken down. Then a large current flows to discharge the main capacitor.

This 3-stage model fits the experimentsl data very well. During Stage II, Figure B-3 shows that the breakdown voltage increases considerably with an increase in the number of gaps. For a large pad/capacitor, the energy in the arc is greater than that for small pad/capacitors. This implies that the restrike voltage will be lower for larger pad/capacitors since the extra energy will provide extra ionization and delay the decrease in conduction. This will cause the slope of the line in Stage II to be inversely proportional to the capacitance of each pad. This energy difference can also account for the slight change in the knee with reference to the number of gaps. For example, the knee occurs at 4 gaps for a 25 pf pad, but for a 5 pf pad, it occurs at 6 gaps. The higher energy for 25 pf pads allows the gap to remain conductive after the arc extinguishes for a longer period of time than the 5 pf pad energy would allow. Hence, Stage III can start at a fewer number of gaps. Once an arc has formed, the voltage drop across the arc will not be a fuction of the pad capacitance. Hence, the slope of the line in Stage III will be independent of the pad capacitance.

For a constant capacitance, the slope during Stage II should be a function of the gap width. After an arc has extinguished, the conductivity of a small gap would be expected to decrease at a lesser rate than that of a larger gap for a given energy deposit in the arc. So, for wide gaps the restrike voltage will increase more quickly as a function of time than for a narrow gap. Hence, the wider the gap, the greater the slope during Stage II.

During Stage III the slope will also increase with increasing gap width but for a different reason. A long arc would be expected to have a greater voltage drop than that of a short arc if the same amount of energy is transferred to each arc. Since, by Equation 1, the slope of the line is equal to the voltage drop across each gap, as the arc becomes longer, the voltage drop becomes greater and the slope of the line increases.

SOME EMPIRICAL SCALING LAWS FOR SINGLE ROW FLASHBOARDS

From the above observations derived from the model and experimental data, several scaling laws become apparent with respect to the pad size, board thickness, number of gaps, and width of gaps. Each of these scaling laws will be examined on the assumption that as one parameter (i.e.; pad size, board thickness, etc.) is varied, all other parameters are fixed.

Pad size along with dielectric material and dielectric thickness determine the capacitance of the pad. For a row of gaps to have a minimum breakdown voltage, the pad capacitance must be large. If the capacitance is large enough, the flashboard will not encounter Stage II but will immediately go to Stage III. The reason for this is found in the fact that for large enough capacitance, the arc in the first gap will not extinguish before the arc in the second gap has formed. This will in fact eliminate the knee in the plot of breakdown voltage vs. number of gaps. Similarly, increasing the dielectric constant of the dielectric and/or decreasing the dielectric thickness will increase the capacitance and eliminate Stage II. Care must be taken when decreasing the dielectric thickness. If the dielectric is too thin, the flashboard will fail due to dielectric breakdown. Once Stage II is eliminated, increasing capacitance has little effect.

For a small number of gaps, the breakdown voltage will increase greatly as more gaps are added until Stage III is encountered. During Stage III, the increase in breakdown voltage with added gaps is greatly reduced. An additional consequence of added gaps is increased flashboard arc impedance.

The width of the gaps plays an important role in determining the slope of the lines in Stages II and III. As the gaps increase in width, the slopes of the lines representing breakdown voltage as a function of number of gaps increase.

MULTIPLE ROW FLASHBOARDS

With a basic understanding of single row flashboards, multiple rows present only a minor step in complication of the subject. The primary difficulty with multiple rows is that of getting each row to breakdown. The problem is that when one row breaks down under certain conditions the other rows are prevented from breaking down.

Multiple row flashboards can be viewed as multichannel breakdown devices. According to Martin, in order for multichanneling to occur, the breakdown times of individual arcs must have jitters less than 10% of the gap voltage decay time. For multiple row flashboards, this problem has several solutions. The authors have observed that as voltage is increased past the minimum breakdown voltage, multichanneling becomes more prevalent. Therefore, if every row does not break down, simply increase the voltage until breakdown is uniform. The reason this works is related to the fact that higher voltages produce longer voltage decay times. Higher voltages also decrease the jitter and formative breakdown time of each gap, therefore fulfilling Martin's criteria. Of course, this has a disadvantage in that a sufficient voltage for multichanneling may cause dielectric breakdown or excessive dielectric or electrode erosion.

The other methods for enhancing the probability of multichanneling are based on delaying the voltage decay once a row has completely broken down. A method used by several investigators is to place 1Ω resistors in series with each row. These resistors limit the current in a row long enough to allow multiple rows to break down. Once each row is capable of breaking down, the resistors flash over, thereby eliminating the need for high power resistors. In fact, 1/2 W resistors are sufficient.

The method of voltage decay delay used in this work relies on added inductance in series with each row. This is accomplished by using individual lines (as wide as the pads) under each row instead of a solid backplane. This technique works very well. On one particular flashboard of 6 parallel lines, the minimum breakdown voltage for one line was around 6 kV. Multilines fired at about 8 kV. Of course, as the voltage was increased, the multilines fired more reliably.

104

Earlier investigators made some note as to the importance of the initial voltage risetime in the operation of multiple row flashboards. Experiments conducted during the present work indicated little change in multiple row characteristics over a range of risetimes less than about 50 ns. Of course, greater risetimes would have an adverse effect on flashboard performance, but below about 50 ns, no improvement is observed for shorter risetimes.

Voltage polarity has a large effect on multiple row breakdown. This phenomena is not understood. Figure B-6 shows four arrangements used to test the signficance of charging polarity and switch placement. As can be seen in the accompanying photographs, the optimum performance is obtained by allowing the backplane to achieve the highest potential and placing the switch in series with the front plane (pads). Again, the reason for this is not yet understood, but this is extremely helpful in optimizing flashboard performance.

One final observation concerns erection time for the flashboard. Once voltage is applied, there is a finite time until the board breaks down. This erection time is a function of all of the single row parameters but more strongly a function of percentage of overvoltage with respect to the minimum breakdown voltage. Around the minimum breakdown voltage the erection time can be on the order of tens of microseconds. For higher voltage, the erection time can be as short as a few tens of nanoseconds or even a few nanoseconds.

SUMMARY

A model for single and multiple row flashboards has been developed which explains the experimental data obtained. Although this is a simple model and does not involve such items as conditioning, surface charging, etc., it does give quite a bit of insight to the operation of flashboards. Several empirical scaling laws are obtained from the model and techniques are presented to enhance multiple row flashboard performance.
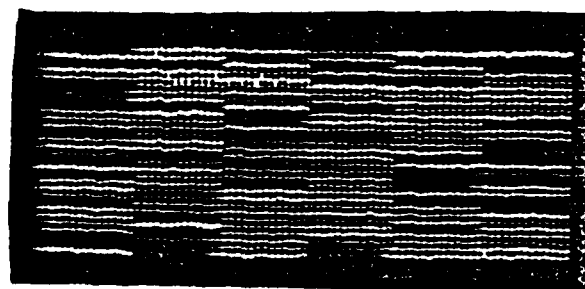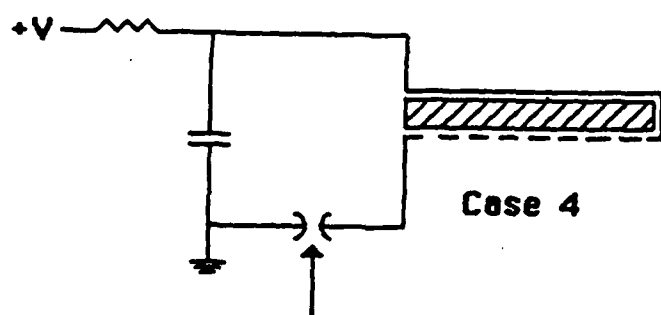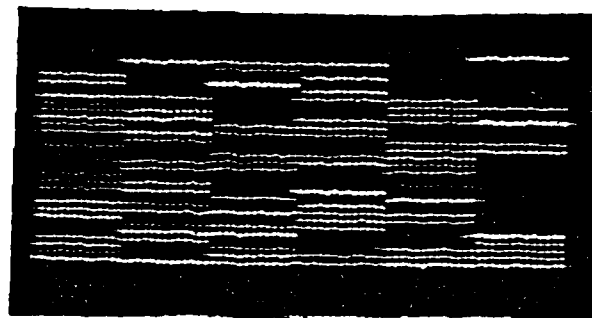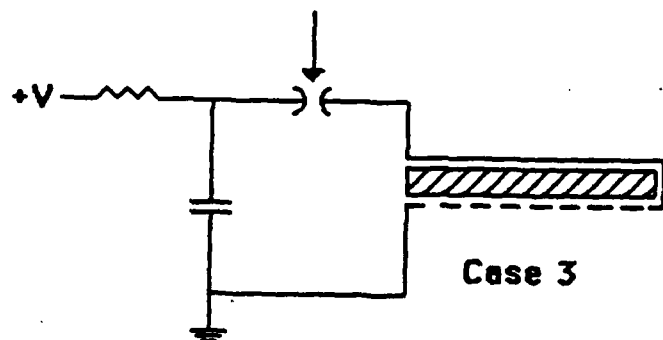
Case 1

Case 2

Case 3

Case 4

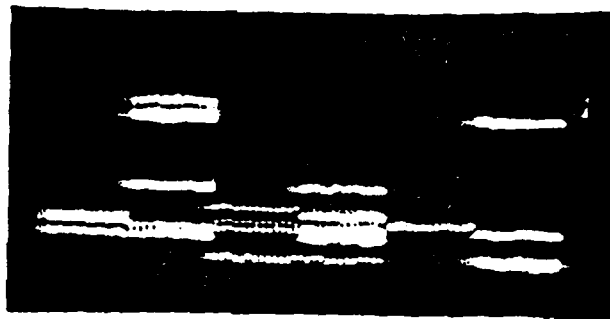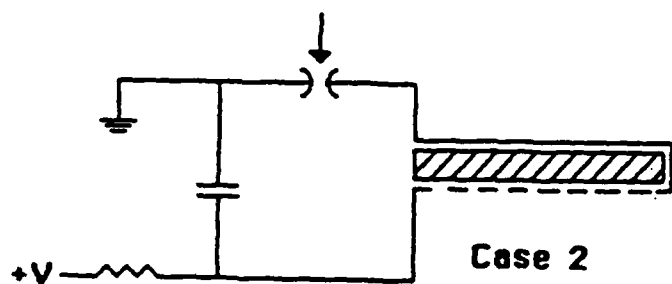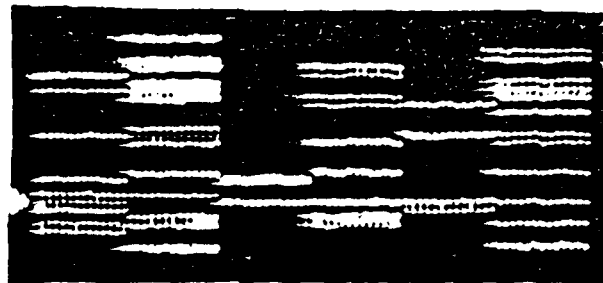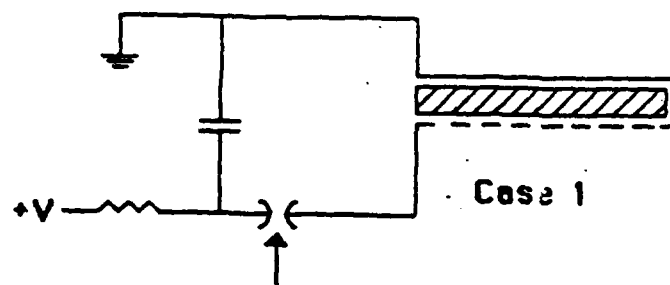FIGURE B-6

EFFECT OF POLARITY ON FLASHBOARD IGNITION

APPENDIX C

THE ELECTRODE DESIGN

The profile used in the electrode design was two blended super-ellipses further blended with an elementary electrode profile. This family of electrode profiles has proved very useful and is described in this Appendix.

Figure 4 in Chapter 4 shows the electrode profile which gave the best electric field distribution for breakdown measurements with a 1 cm electrode gap. Figure C.1 shows the resultant electric field distribution relative to a reference electric field at the center of the discharge of 1,000 V/cm. The solid curves represent the electric field magnitude as a function of arc length along the electrode surfaces. The dotted line represents the electric field as a function of arc length through the center of the discharge region. It is noted that these calculations are done without the presense of the plasma. The maximum relative deviation above the reference electric field is 0.97%. This is quite sufficient for the measurement of break down voltages. If the gap is increased to 1 1/2 cm for this profile, however, then the electric field distribution is shown by Figure C.2. The roll off enhancement is now 18%. This electrode is good only for a 1 cm gap.

Figure 5 in Chapter 4 shows the electrode profile which was designed for variable spacing. As shown in Figure C.3, the enhancement for a 1 cm gap is now 2.1%, compared with less than 1% for the previously described electrode. When the gap is increased to 1 1/2 cm however, the enhancement is now only 4.4%, as shown in Figure C.4. It is not until a spacing of 2 1/2 cm that the enhancement reaches 19%. Since all the switching experiments were conducted below the breakdown voltage this electrode was adequate for actual switching experiments. The two solid electrodes were machined out of stainless steel on a NC lathe.

1. THE BLENDED SUPER-ELLIPSE ELECTRODE FAMILY

The super-ellipse is defined (in the first quadrant) by the equation

$$(x/x_1)^p + (y/y_1)^p = 1 \qquad\qquad C.1$$

E-VAL. VS. S

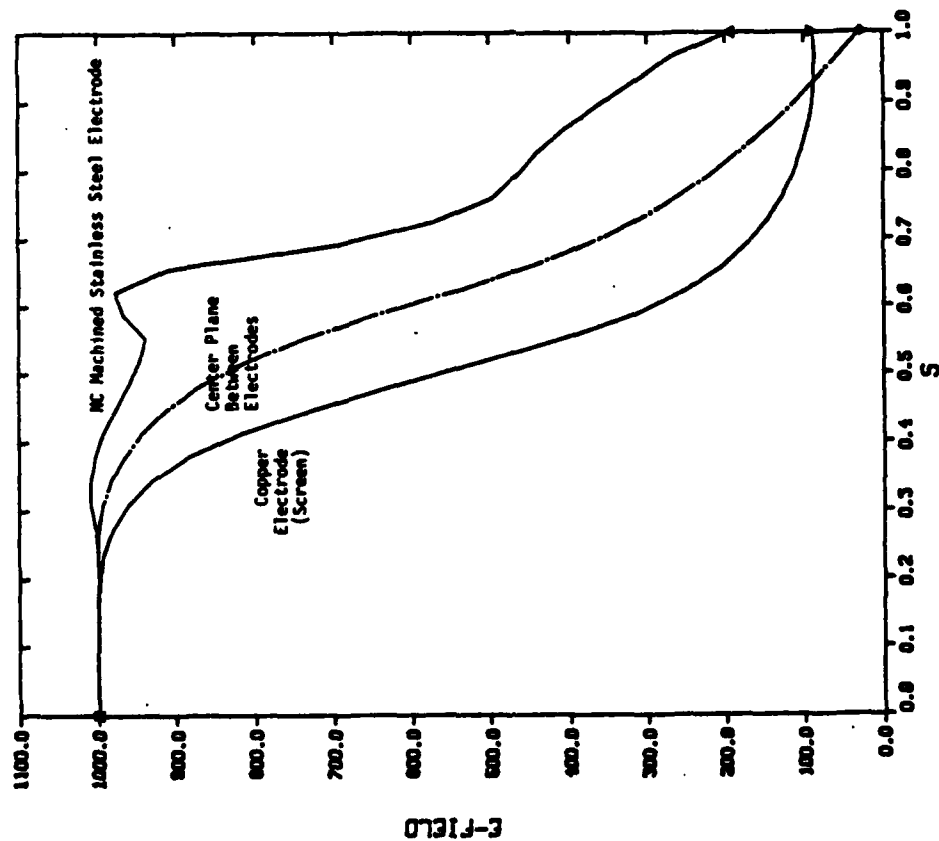Figure C.2 As in Figure C.1, but with a 1.5 cm Gap.

E-VAL. VS. S

Figure C.1 The Electric Field Magnitude as a Function of Normalized Distance along the Electrode Surfaces for the Profile Designed for a 1 cm Gap and with a 1 cm Gap.
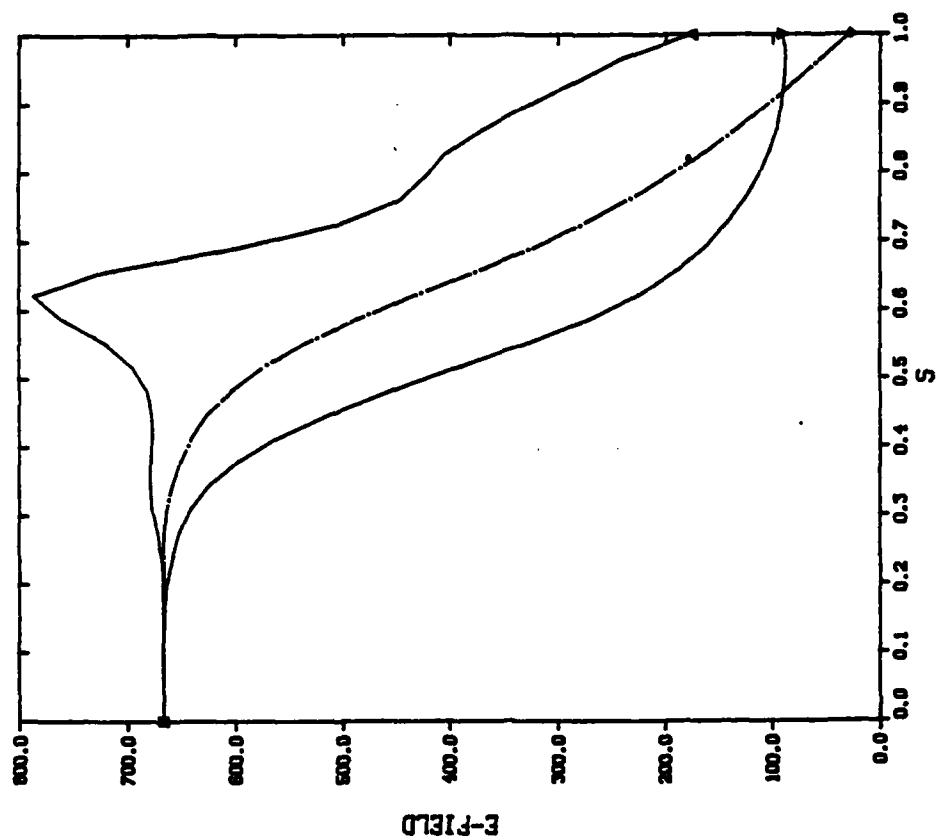
108

E-VAL. VS. S

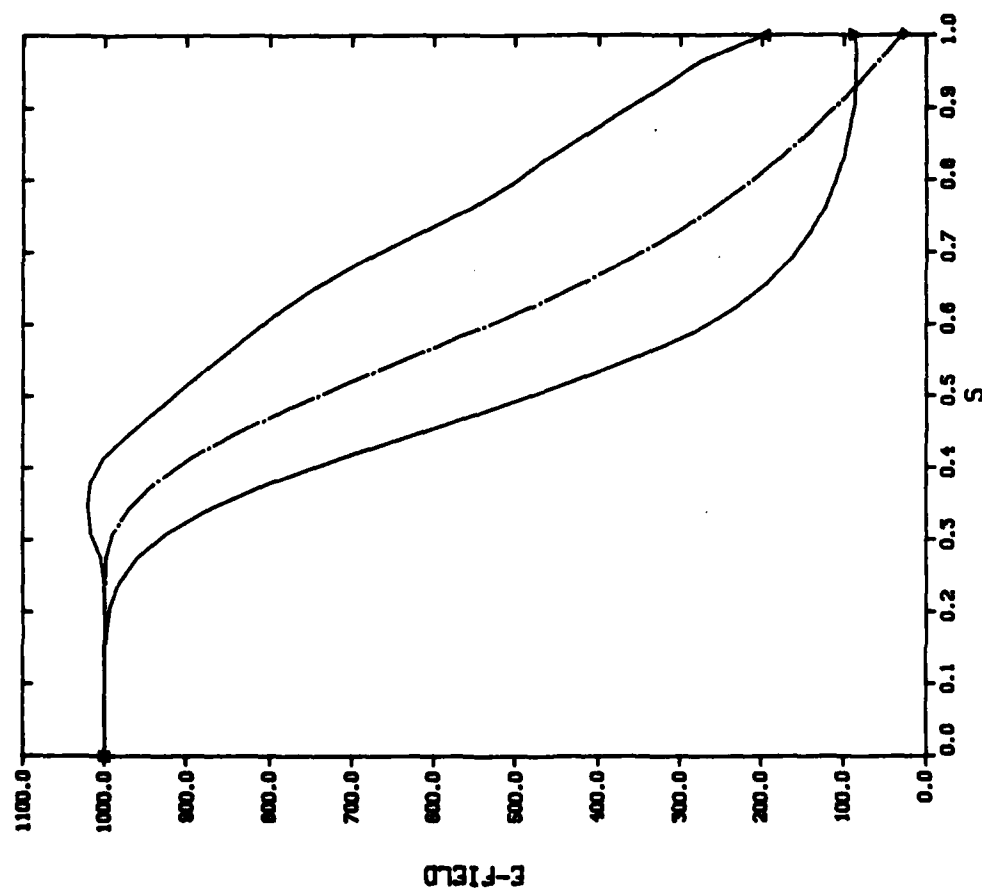Figure C.4 As in Figure C.3, but with a 1.5 cm Gap.

E-VAL. VS. S

Figure C.3 The Electric Field Magnitude as a Function of Arc Length
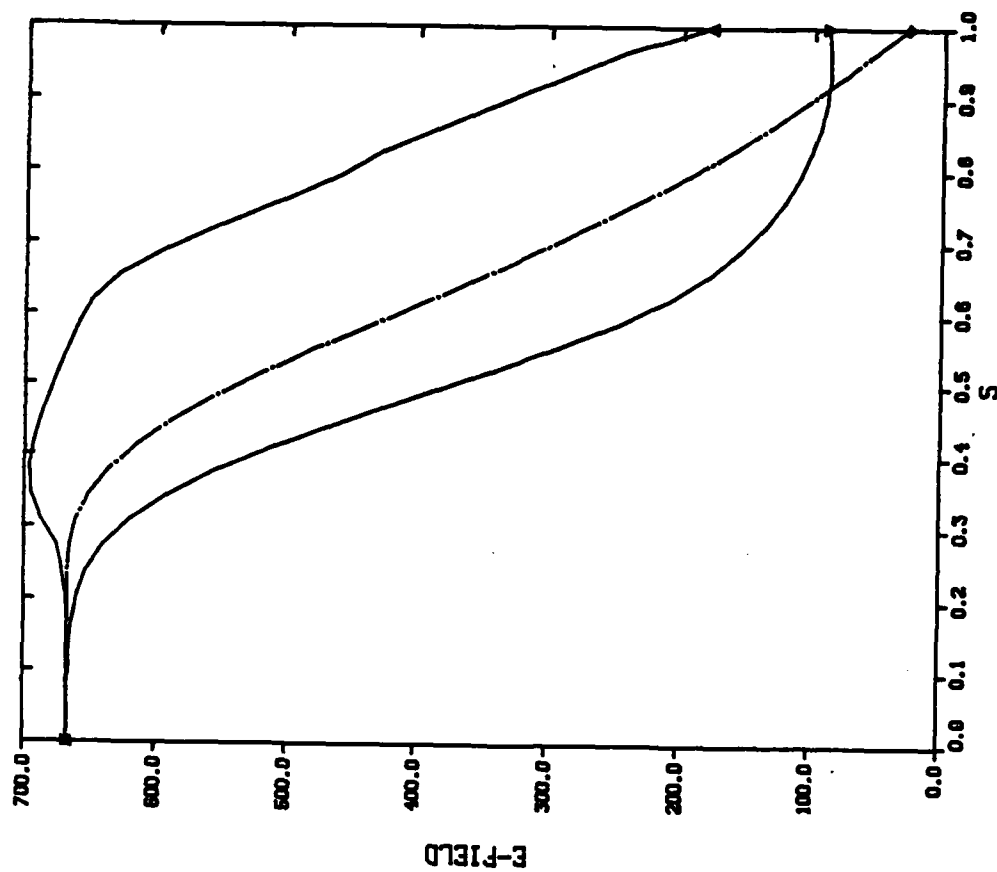for the Profile Designed for Variable Spacing, with
a 1 cm Gap.

where x_1 and y_1 are the dimensions of the circumscribed rectangle of the inner electrode surface. For $p = 2$, a simple ellipse is obtained. For $p \geq 2$, the surface is smooth and tangent to the circumscribed rectangle at the end points. As $p \to \infty$, the super-ellipse approaches the circumscribed rectangle. Each electrode inner surface is then obtained as a linear blend of two super-ellipses of powers P_L and P_R with the same semi-major and -minor axes x_1 and y_1. They are blended by a factor w_L; in polar coordinates (r, θ) at the same θ, the r's are blended as

$$r = w_L \bullet r_L + (1 - w_L) \bullet r_R \qquad \text{(C.2)}$$

This blended super-ellipse surface can be shifted, so that the initial section is a straight line, and can be further blended with an elementary electrode formed by a straight section and a radius. The inner surface can be further modified by a blended perturbation, which may be used for E-field shaping (e.g. to accomplish pre-ionization). The perturbation is a shifted sinewave, raised to a power P_p. As P_p becomes large, the perturbation approahces a rectangle, but is smooth and blends to the basic shape with continuous first derivatives for finite P_p, avoiding sharp corners. The back side or outer surface is formed by a simple radius and a straight section. Neither of the switch electrodes required the blended perturbation.

110

APPENDIX D

LIST OF PARTICIPATING SCIENTIFIC PERSONNEL

William M. Moeny - Principal Investigator
A.I. Lampson
M. vonDadelszen (Ph.D. earned while employed on the project)
A. E. Rodgriguez
C. M. Young

APPENDIX E

LIST OF PUBLICATIONS AND PLANNED PUBLICATIONS

Moeny, W. M. and Lampson, A. I., "Field Distortion Control of Glow Discharges",
4th IEEE Pulse Power Conference, Albuquerque, NM, June 6-8, 1983.

Moeny, W. M. and Lampson, A. I., "Field Distortion Control of Glow Discharges",
to be submitted to IEEE Transactions on Plasma Science.

Moeny, W. M. and vonDadelszen, M., " UV-Sustained Glow Discharge Opening
Switch Experiments", 5th IEEE Pulse Power Conference, Washington, DC,
June 12-15, 1985.

Moeny, W. M. and vonDadelszen, M., "UV-Sustained Glow Discharge Opening
Switch Experiments", to be submitted to IEEE Transactions on Plasma
Science.

vonDadelszen, M., "Electrode Design Using the ELF Code", to be submitted to
Review of Scientific Instruments.

Rodriguez, A. E., "Electro-Magnetic Noise Generation from Glow and Spark
Discharges", to be submitted to IEEE Transactions on Plasma Science.

REFERENCES

1. D. F. Grosjean, and P. Bletzinger, "Photoionization and Photoabsorption Characteristics of Laser Seed Compounds," IEEE Journal of Quantum Electronics, Vol. OE-13, No. 11, November 1977.

2. P. J. Roache, S. Steinberg, W. M. Moeny, "Interactive Electric Field Calculations for Lasers," in Proceedings of the AIAA 17th Fluid Dynamics, Plasma Dynamics, and Lasers Conference, 1984.

3. S. A. Wutzke, D. R. Suhre, L. H. Taylor, L. E. Kline, R. R. Mitchell, and M. J. Pechersky, "UV Photoionized CO Electric Laser Research," Final Technical Report, Westinghouse R&D Center, Pittsburgh, Pennsylvania, October 1977.

4. G. N. Glasoe, and J. V. Lebacqz, Pulse Generators, McGraw-Hill, New York, 1948.

5. P. R. Bevington, "Data Reduction and Error Analysis for the Physical Sciences," McGraw-Hill 1969.

6. S. M. Spyrou, I. Sauers, and L. G. Christophorou, "Electron Attachment to the Perfluoroalkanes $n-C_NF_{2N+2}(N=1-6)$ and $i-C_4F_{10}$," J. Chem. Phys 78(12), June 1983.

7. S. C. Brown, Basic Data of Plasma Physics, 2nd ed., M.I.T., 1966.

8. P. Bletzinger, "Measurement of Oscillations in Gases with Negative Differential Conductivity," 37th Annual Gaseous Electronics Conference, University of Colorado, October 1984.

9. D. H. Douglas-Hamilton, and R. S. Lowder, "Carbon Dioxide Electric Discharge Laser Kinetics Handbook," AFWL, Report no. AFWL-TR-74-216, April 1975.

10. J. J. Lowke, A. V. Phelps, and B. W. Irwin, "Predicted Electron Transport Coefficients and Operating Characteristics of CO_2/N/He Laser Mixtures," Journal of Appl. Phys. 44, 4664, 1973.

11. 12 IBID Douglas-Hamilton et. al.

13. N. H. Frank, "Introduction to Electricity and Optics, McGraw-Hill, 2nd Ed., 1950.

14. J. D. Jackson, "Classical Electrodynamics, John Wiley & Sons, 1962.

15. A. E. Rodriguez, "Externally Generated EMP Threats to Satellites, draft echnical report, Tetra Corp.

END

FILMED

10-85

DTIC